Anomalous Transport through Porous and Fractured Media

by

Peter Kyungchul Kang

B.S., Seoul National University (2008)
S.M., Massachusetts Institute of Technology (2010)

Submitted to the Department of Civil and Environmental Engineering
in partial fulfillment of the requirements for the degree of

Doctor of Philosophy in the Field of Hydrology

at the

MASSACHUSETTS INSTITUTE OF TECHNOLOGY

June 2014

ARCHIVES
MASSACHUSETTS INSTITUTE OF TECHNOLOGY
JUN 13 2014
LIBRARIES

© 2014 Massachusetts Institute of Technology. All rights reserved.

Signature redacted

Author .....
Department of Civil and Environmental Engineering
May 12, 2014

Signature redacted

Certified by .....
Ruben Juanes
Associate Professor of Civil and Environmental Engineering
Thesis Supervisor

Signature redacted

Accepted by .....
Heidi M. Nepf
Chair, Departmental Committee for Graduate Students

Anomalous Transport through Porous and Fractured Media

by

Peter Kyungchul Kang

Submitted to the Department of Civil and Environmental Engineering
on May 12, 2014, in partial fulfillment of the
requirements for the degree of
Doctor of Philosophy in the Field of Hydrology

Abstract

Anomalous transport, understood as the nonlinear scaling with time of the mean square displacement of transported particles, is observed in many physical processes, including contaminant transport through porous and fractured geologic media, animal and human foraging patterns, tracer diffusion in biological systems, and transport in complex networks. Understanding the origin of anomalous transport is essential, because it determines the likelihood of high-impact, low-probability events and therefore exerts a dominant control over the predictability of a system. The origin of anomalous transport, however, remains a matter of debate.

In this thesis, we first investigate the pore-scale origin of anomalous transport through sandstone. From high-resolution (micron-scale) 3D numerical flow and transport simulation, we find that transport at the pore scale is markedly anomalous. We demonstrate that this anomalous behavior originates from the intermittent structure of the velocity field at the pore scale, which in turn emanates from the interplay between velocity heterogeneity and velocity correlation. Finally, we propose a continuous time random walk (CTRW) model that honors this intermittent structure at the pore scale and captures the anomalous 3D transport behavior at the macroscale.

To show the generality of our finding, we study transport through lattice networks with quenched disorder. We again observe anomalous transport originating from the interplay between velocity heterogeneity and velocity correlation. We extend the developed CTRW model to capture the full multidimensional particle transport dynamics for a broad range of network heterogeneities and for both advection- and diffusion-dominated flow regimes.

We then study anomalous transport through fractured rock at the field-scale. We show that the interplay between heterogeneity and correlation in controlling anomalous transport can be quantified by combining convergent and push-pull tracer tests because flow reversibility is strongly dependent on correlation, whereas late-time scaling of breakthrough curves is mainly controlled by velocity heterogeneity. Our transport model captures the anomalous behavior in the breakthrough curves for both push-pull and convergent flow geometries, with the same set of parameters. Moreover, the inferred flow correlation length shows qualitative agreement with geophysical measurements. Thus, the proposed correlated CTRW modeling approach furnishes a simple yet powerful framework for characterizing the impact of flow correlation and heterogeneity on transport in porous and fractured media.

Finally, we propose a joint flow-seismic inversion methodology for characterizing fractured reservoirs. Traditionally, seismic interpretation of subsurface structures is performed without any account of flow behavior. With the proposed methodology, we reduce the uncertainty by integrating dynamic flow measurements into the seismic interpretation, and improve the predictability of reservoir models by this joint use of seismic and flow data. This work opens up many possibilities of combining geophysical and flow information for improving subsurface characterization.

Thesis Supervisor: Ruben Juanes
Title: Associate Professor of Civil and Environmental Engineering

Acknowledgments

I am deeply grateful to my family, friends, colleagues, and mentors who helped me to grow in various ways during my PhD studies. To name only a few, I offer my thanks

to the DOE Office of Science Graduate Fellowship (DOE SCGF) program for supporting my graduate studies for three years;

to the Martin Family Society of Fellows for Sustainability at MIT for supporting my graduate studies;

to my advisor, Ruben Juanes, for his guidance, mentorship, and support throughout my PhD studies;

to my research mentor, Marco Dentz, who taught me from the basics and helped me to become an independent researcher;

to my thesis committee, Dennis B. McLaughlin and Daniel H. Rothman for their guidance and support towards my studies;

to Tanguy Le Borgne, who provided field experiment facilities and mentored me throughout the field experiments in Ploemeur, France;

to Martin J. Blunt, who shared pore-scale experiment data and guided my research on pore-scale transport;

to Susan Murcott, who inspired me with her works in drinking water issues in developing countries and motivated me to visit Tanzania;

to the members of the Juanes Research Group for their friendship and boundless enthusiasm for science;

to my parents, In-Sik and Jeung-Hee, and my sister, Sarah, for their unconditional love and support;

and, to my fiancée, SunMin Hwang, for her trust and love towards me. With her love and support, I could finish my PhD thesis with full of joy.

Contents

List of Figures

Chapter 1

Introduction

1.1 Anomalous transport: the breakdown of Fick's law

Understanding flow and transport through subsurface is essential for improving forecasts, management, and risk assessment of many underground technologies, including geologic nuclear waste disposal [17], geologic CO_2 storage [137]; oil and gas production from fractured reservoirs [84], enhanced geothermal systems [118], shale-gas development [31, 30], and groundwater contamination and remediation [58, 69]. Since subsurface consists of rock which is highly porous and often fractured, the prediction of flow and transport through subsurface requires understanding of flow and transport through porous and fractured media.

The transport of mass through porous media is traditionally described with two processes: advection and dispersion where advection is the translation of the mass following the mean flow direction and the dispersion describes the spreading of the mass. Since Adolf E. Fick introduced the diffusion equation (Fick's law) in 1855 [54], Fick's law still is the dominant framework that describes dispersive transport processes in porous materials, nuclear materials, pharmaceuticals, population dynamics, neurons, semiconductor doping process, etc. Implicit in Fick's law is that the time evolution of the mean square displacement (MSD) of passive tracers increases linearly with time, MSD $\sim t$. However, the generality of Fick's law has been questioned since 1926 when L. F. Richardson observed how particles disperse in the atmosphere [122]. Again in 1948, Richardson studied the relative displacements of pairs of submersed floats over a fixed interval of time on the west

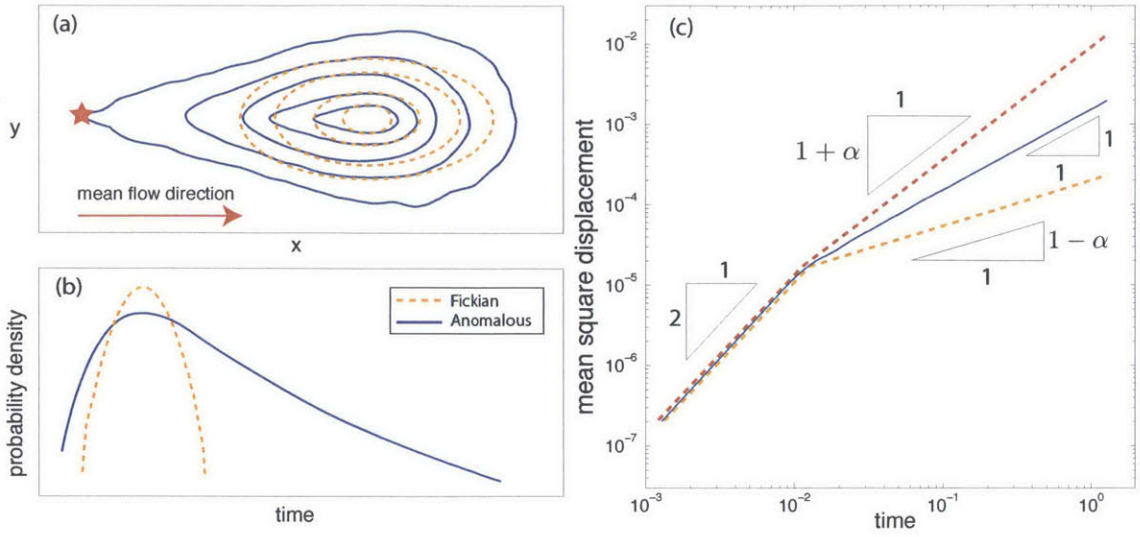

Figure 1-1: Illustration of the manifestations of anomalous transport. (a) After a point injection of tracers (red star), anomalous transport often shows a strongly non-Gaussian concentration field as opposed to a Gaussian concentration field for Fickian dispersion. (b) Tracer concentration measured from the fixed control plane shows early time breakthrough and long tailing for anomalous transport. (c) Time evolution of mean square displacements shows nonlinear increase in time for anomalous transport.

coast of Scotland and observed the clear breakdown of Fick's law, MSD $\sim t^{\alpha}, \alpha \neq 1$ [123].

Since then, anomalous (non-Fickian) transport has been widely observed in many domains: transport in amorphous semiconductors, contaminant transport through porous and fractured geologic media, animal foraging, human travel, and diffusion of passive tracers in turbulent flows, to name just a few. The signatures of anomalous behavior are non-Gaussian or multipeaked plume shapes, early breakthrough, long tailing of the first passage time distribution, and nonlinear scaling of the MSD—effects that cannot be captured by a traditional advection-dispersion formulation [Fig. 1-1]. Understanding the origin of the slow-decaying tails in probability density is essential, because they determine the likelihood of high-impact, low-probability events and therefore exert a dominant control over the predictability of a system.

The focus of this thesis is anomalous transport through porous and fractured media. Despite the broad relevance of flow and transport through geologic porous media, our understanding still faces significant challenges due to the almost ubiquitous observation of anomalous transport behavior, from laboratory experiments in packed beds [76, 108], sand

columns [95] and real rock samples [130, 14] to field-scale experiments [56, 88]. Different mathematical models have been proposed to reproduce anomalous transport by replicating the broad (power-law) distribution of velocity; these include multirate mass transfer [63], fractional advection-dispersion [102], and continuous time random walk (CTRW) models [10, 12].

In this thesis, we investigate the origin of anomalous transport through porous and fractured media, and propose a parsimonious stochastic transport model capable of capturing anomalous transport. We first identify the origin of anomalous transport in 3D porous rock using high-resolution 3D numerical flow and transport simulation at the pore scale. To show the generality of our finding, we then extend our model to Darcy-scale transport through lattice networks. We then apply the developed model to study field-scale anomalous transport through fractured geologic media. Finally, we propose a joint flow-seismic inversion methodology for characterizing fractured reservoirs.

1.2 Numerical experiments on 3D real rock

In the first part of this thesis (Chapter 2), we study the origin of non-Fickian particle transport in 3D porous media by simulating fluid flow in the intricate pore space of real rock. We simulate Stokes flow at the same resolution as the 3D micro-CT image of the rock sample, and simulate particle transport along the streamlines of the velocity field [Fig. 1-2(a)]. We find that transport at the pore scale is markedly anomalous: longitudinal spreading is superdiffusive, while transverse spreading is subdiffusive. We demonstrate that this anomalous behavior originates from the intermittent structure of the velocity field at the pore scale, which in turn emanates from the interplay between velocity heterogeneity and velocity correlation [Fig. 1-2(b)]. Finally, we propose a continuous time random walk model that honors this intermittent structure at the pore scale and captures the anomalous 3D transport behavior at the macroscale. These results have been submitted for publication [80].

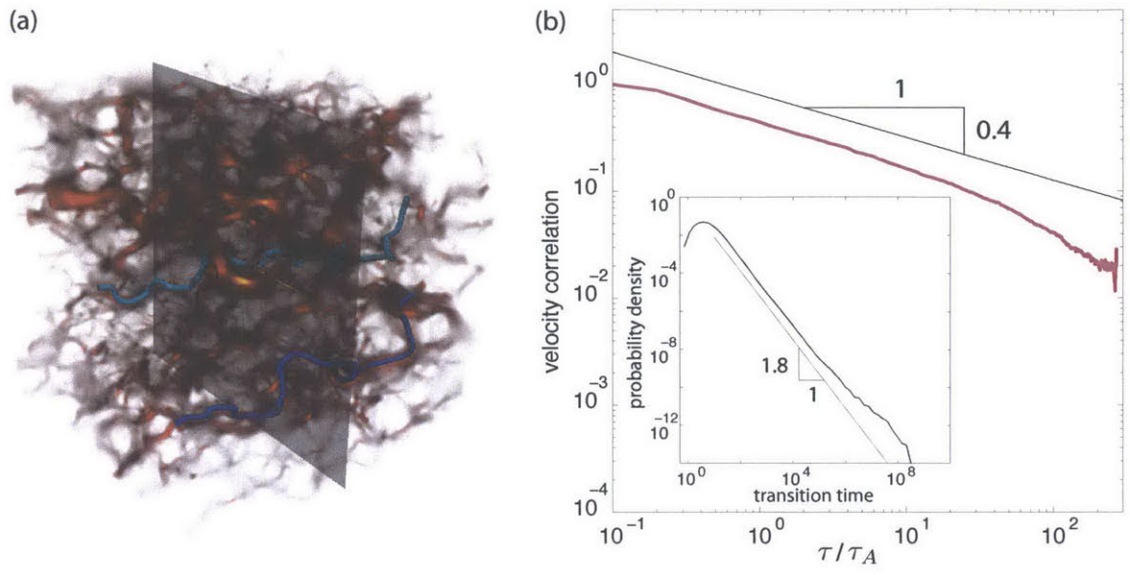

Figure 1-2: (a) Three-dimensional normalized velocity magnitude ($|\mathbf{v}|/\bar{v}$) through a Berea sandstone sample of size 1.66 mm (approximately 8 pore lengths) on each side; blue and cyan solid lines indicate two particle trajectories. The domain is discretized into 300^3 voxels with resolution 5.55 μm (approximately 0.03 pore lengths). (b) Velocity autocorrelation function shows power-law decay of Lagrangian velocity in time. Inset: transition time distribution shows broad distribution following truncated power-law.

1.3 Anomalous transport through lattice fracture networks

In the second part of this thesis (Chapter 3), we extend our findings to transport through lattice fracture networks. Flow through lattice networks with quenched disorder exhibits strong correlation in the velocity field, even if the link transmissivities are uncorrelated. This feature, which is a consequence of the divergence-free constraint, induces anomalous transport of passive particles carried by the flow. We show that, for lattice fracture networks, the interplay between this strong velocity correlation and velocity heterogeneity is again the origin of anomalous transport. We extend the developed CTRW model to capture the full multidimensional particle transport dynamics for a broad range of network heterogeneities and for both advection- and diffusion-dominated flow regimes. The model captures the anomalous longitudinal and transverse spreading, and the tail of the mean first passage time observed in the Monte Carlo simulations of particle transport. We show that reproducing these fundamental aspects of transport in disordered systems requires honoring both the correlation and the heterogeneity in the Lagrangian velocity. These results

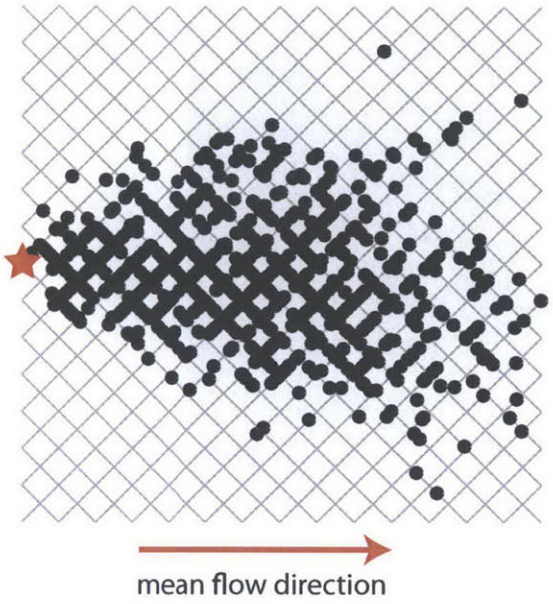

Figure 1-3: Particle distribution at a fixed time after injection at the origin (red star).

have been published in *Physical Review Letters* and *Physical Review E* [78, 77].

1.4 Field experiment on fractured granite

In the third part of this thesis (Chapter 4), we study anomalous transport through fractured rock at the field scale [Fig. 1-4(a)]. Quantitative modeling of flow and transport through fractured geological media is challenging due to the inaccessibility of the underlying medium properties and the complex interplay between heterogeneity and small-scale transport processes such as heterogeneous advection, matrix diffusion, hydrodynamic dispersion, and adsorption. This complex interplay leads to anomalous (non-Fickian) transport behavior, and we show that the interplay between heterogeneity and correlation in controlling anomalous transport can be quantified by combining convergent and push-pull tracer tests because flow reversibility is strongly dependent on correlation, whereas late-time scaling of breakthrough curves is mainly controlled by velocity heterogeneity [Fig. 1-4(b)(c)]. In the framework of the developed CTRW model, flow heterogeneity and flow correlation are quantified by a Markov process of particle transition times that is characterized by a distribution function and a transition probability. Our transport model captures the anomalous

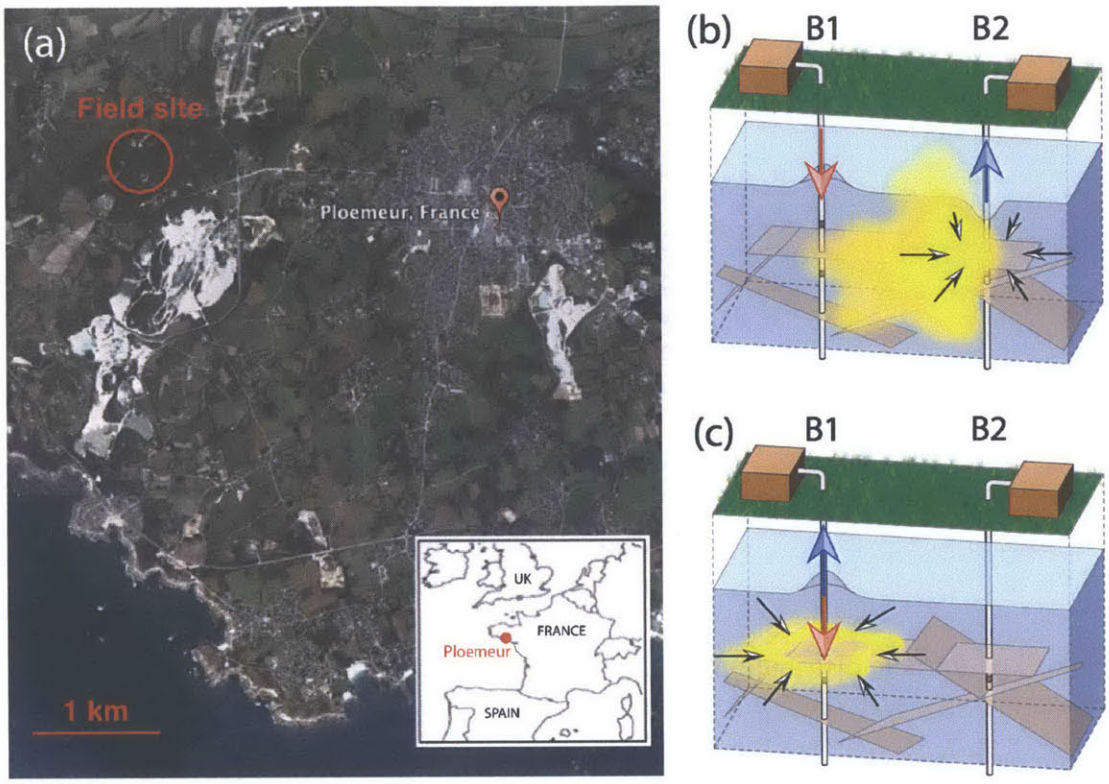

Figure 1-4: (a) Satellite image of the Ploemeur field site where we conducted field-scale tracer transport experiment through fractured granite (modified from Google Earth). Inset: map showing the location of Ploemeur, France. (b) Schematic of the convergent tracer tests conducted. (c) Schematic of the push-pull tracer tests conducted.

behavior in the breakthrough curves for both push-pull and convergent flow geometries, with the same set of parameters. Thus, the proposed correlated CTRW modeling approach furnishes a simple yet powerful framework for characterizing the impact of flow correlation and heterogeneity on transport in fractured media. These results have been submitted for publication [81].

1.5 Joint flow–seismic inversion for characterizing fractured reservoirs

In the fourth part of this thesis (Chapter 5), we propose a joint flow-seismic inversion methodology for characterizing fractured reservoirs. Traditionally, seismic interpretation

of subsurface structures is performed without any account of flow behavior. Here, we present a methodology to characterize fractured geologic reservoirs by integrating flow and seismic data. The key element of the proposed approach is the identification of the intimate relation between acoustic and flow responses of a fractured reservoir through fracture compliance. By means of synthetic models, we show that: (1) owing to the strong (but highly uncertain) dependence of fracture permeability on fracture compliance, the modeled flow response in a fractured reservoir is highly sensitive to the geophysical interpretation; and (2) by incorporating flow data (well pressures and production curves) into the inversion workflow, we can simultaneously reduce the error in the seismic interpretation and improve predictions of the reservoir flow dynamics. These results have been published in a conference paper and in preparation for journal publication [79].

1.6 Conclusions and future work

In the last chapter of this thesis (Chapter 6), we conclude by summarizing the intellectual contributions of this thesis to understanding anomalous transport through porous and fractured media, and we discuss possible future work that could build on this thesis.

Chapter 2

Numerical experiments on 3D real rock

In this Chapter, we first investigate the pore-scale origin of anomalous transport through sandstone. From high-resolution $3D$ numerical simulation on real $3D$ rock, we rigorously identify the physical origin of observed anomalous transport and develop a predictive stochastic model.

2.1 Background

Fluid flow and transport in porous media is critical to many natural and engineered processes, including sustainable exploitation of groundwater resources [66, 60], seawater intrusion into coastal aquifers [53], enhanced oil recovery [114], geologic carbon sequestration [71, 137], geologic nuclear waste disposal [154], water filtration and membrane technology [131], and drug delivery and chemical signaling through living tissue [50].

Despite the broad relevance of flow and transport through geologic porous media, our understanding still faces significant challenges. One such challenge is the almost ubiquitous observation of anomalous (non-Fickian) transport behavior, from laboratory experiments in packed beds [76, 108], sand columns [95] and real rock samples [130, 14] to field scale experiments [56, 88]. The signatures of anomalous behavior are early breakthrough, long tailing of the first passage time distribution, non-Gaussian or multipeaked plume shapes, and nonlinear scaling of the mean square displacement—effects that cannot be captured by a traditional advection-dispersion formulation. Different mathematical

models have been proposed to reproduce anomalous transport, by replicating the broad (power-law) distribution of velocity; these include multirate mass transfer [63], fractional advection-dispersion [102], and continuous time random walk (CTRW) models [10, 12].

In addition to velocity heterogeneity, recent studies have pointed out the importance of velocity correlation in the signature of anomalous transport [90, 39, 78]. In particular, numerical simulations using smoothed particle hydrodynamics of flow and transport on simple 2D porous media suggest that longitudinal spreading is strongly modulated by the intermittent and correlated structure of Lagrangian velocity [35], which is also observed in laboratory experiments in 3D glass bead packs [34]. Moreover, fundamental understanding on the impact of velocity heterogeneity and correlation on *transverse spreading* is poor. It is known that transverse spreading largely controls overall mixing and, as a result, many chemical and biological processes in natural systems [13, 139, 151, 138, 126].

In this Chapter, we study flow and particle transport through real rock (Berea sandstone), imaged at the pore scale via micro-computed tomography (micro-CT imaging). We observe strongly non-Fickian spreading behavior in both longitudinal and transverse directions, and find complementary anomalous behavior: longitudinal spreading is superdiffusive, while transverse spreading is subdiffusive. We show that the interplay between pore-scale velocity correlation and velocity heterogeneity is responsible for the observed anomalous behavior. We then develop a stochastic transport model for 3D porous media that incorporates the microscale velocity structure. To show the generality of the proposed framework, we also investigate the impact of particle injection rule on the macroscopic spreading. Finally, we further simplify our stochastic model such that it has only two parameters: one for flow heterogeneity and the other for flow correlation. We show the predictability of the simplified model, and discuss the potential applicability.

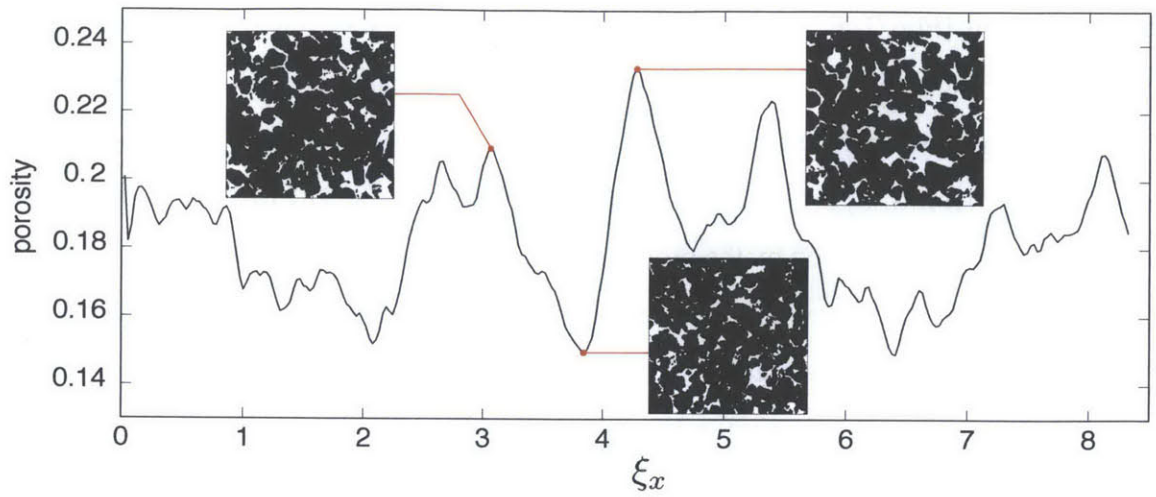

Figure 2-1: Areal porosity variation along the longitudinal direction. Areal porosity varies between 0.15 and 0.23. Volumetric porosity of the 3D sample rock is 0.18. Insets: 2D porosity maps at three different locations. White indicates pore space and black indicates solid rock.

2.2 Fluid flow and particle tracking through Berea sandstone

We analyze the 3D Lagrangian velocities of a Newtonian fluid flowing through a cube sample of Berea sandstone rock of size $L = 1.66$ mm on each side. Micro-CT is used to obtain the 3D image of the porous structure at a resolution of 5.55 μm (300^3 voxels). Image segmentation identifies each voxel as either solid or void. The characteristic length of the mean pore size is $\lambda_c \approx 200$ μm [109], which is used to define the nondimensional distance $\xi_x = x/\lambda_c$ (the sample has ~ 8 characteristic pore lengths in each direction). The porosity and pore structure variation along longitudinal direction shows complex porous structure of Berea sandstone [Fig. 2-1].

We simulate Stokes flow (incompressible steady viscous flow) through the pore geometry of the Berea sandstone with no-slip boundary conditions at the grain surfaces, using a standard finite volume method [113, 16, 15]. We impose constant pressure boundary conditions at the inlet and outlet faces. The Eulerian velocity field $\mathbf{v}$ exhibits a complex structure, with multiple preferential flow channels and stagnation zones [Fig. 2-2(a)]. To confirm the incompressible steady viscous flow, we calculate mean velocity along longi-

tudinal direction [Fig. 2-3(a)]. As expected, x-directional mean velocity stays constant confirming the incompressible steady viscous flow. The transverse velocities fluctuates around 0. If we compute the effective mean velocity (average velocity over pore space), we obtain $\overline{v_x} = 6.37\mu$m/s, $\overline{v_y} = -0.16\mu$m/s, and $\overline{v_z} = -0.26\mu$m/s. The heterogeneity of the flow field can be characterized by the probability density function of Eulerian velocity field [Fig. 2-3(b)]. In all directions, Eulerian velocity shows strongly heterogeneous distribution with power -0.5. The overall structure of the probability distribution between longitudinal and transverse direction is similar but longitudinal direction has higher probability for larger velocity. 29% of the pore space has velocity larger than the mean velocity ($\overline{v_x}$) and 71% of the pore space has velocity smaller than the mean velocity ($\overline{v_x}$). This indicates that there are a few preferential paths and large number of stagnation zones. Probability density function of Lagrangian velocities sampled equidistance in time shows slope -0.75 [Fig. 2-3(b)inset]. This implies higher probability of having small velocities for Lagrangian velocity distribution compared to Eulerian velocity distribution. This is because the particles with small velocities are sampled much more compared to fast velocities if we sample equidistance in time.

To study the transport properties, we simulate the advection of particles along streamlines of the stationary 3D flow field. We trace streamlines using a semianalytical formulation to compute entry and exit positions, and transit times, through each voxel traversed by individual streamlines [109]. To initialize the streamlines, we place 10^4 particles at the inlet face, following a *flux-weighted* spatial distribution through the pore geometry. To obtain particle trajectories that are long enough to observe macroscopic behavior, we concatenate particle trajectories randomly within the same class of the flux probability distribution (we have confirmed that the flux distribution at inlet and outlet faces are virtually identical). To ensure representative statistics of transverse displacement, we reinject a particle (following the same flux-weighted protocol) whenever its distance to one of the lateral boundaries is less than 2 voxels. We compute the mean Lagrangian velocity across all trajectories, $\bar{v}$, and define the characteristic time to travel the average pore size as $\tau_A = \lambda_c/\bar{v}$, which is used to rescale time. Two particle trajectories are shown in Figure 2-2(a).

We first analyze the time evolution of Lagrangian mean velocity and Lagrangian veloc-

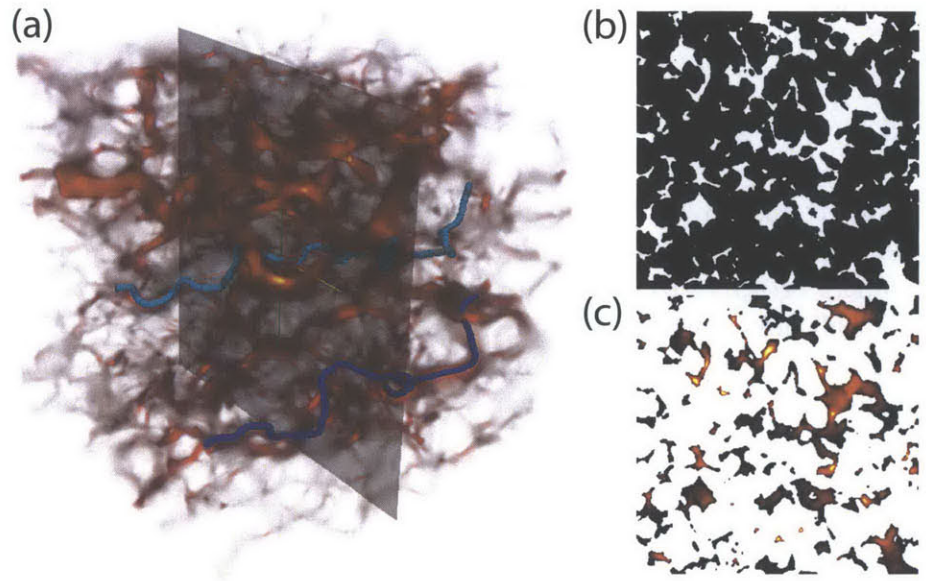

Figure 2-2: (a) Three-dimensional normalized velocity magnitude ($|\mathbf{v}|/\bar{v}$) through a Berea sandstone sample of size 1.66 mm (approximately 8 pore lengths) on each side; blue and cyan solid lines indicate two particle trajectories. The domain is discretized into 300^3 voxels with resolution 5.55 μm (approximately 0.03 pore lengths). (b) Cross section of the Berea sandstone at rescaled distance $\xi_x = \frac{x}{\lambda_c} = 4.16$, showing the pore space (white) and solid grains (black). The average porosity (fraction of void space in the sample) is approximately 18.25%. (c) Cross section of the velocity magnitude at rescaled distance $\xi_x = 4.16$ (warm colors correspond to higher velocities), illustrating the presence of preferential flow paths.

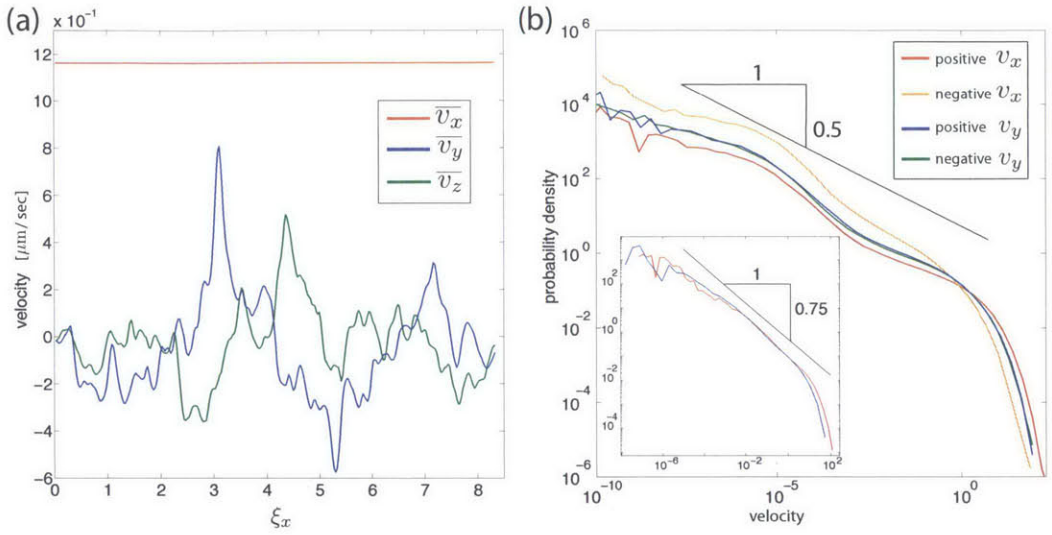

Figure 2-3: (a) Average velocity along longitudinal direction. From the incompressibility, x-directional mean velocity stays constant. Transverse (y, z) directional velocity has fluctuations around 0 velocity. (b) Probability density functions for Eulerian velocities in each direction. For all directions, we can observe very broad distribution of velocities (more than ten orders of magnitude). Inset: Probability density functions for Lagrangian velocities in each direction. The slope is 0.75 which is steeper than the slope for Eulerian velocity distribution.

ity variance for ensemble of particles in all directions [Fig. 2-4]. We observe power law decay of Lagrangian velocity mean and variance indicating nonstationarity of Lagrangian statistics. The nonstationarity and the power-law decay originates from the flux-weighted injection and the strongly heterogeneous velocity field. The *flux-weighted* injection places large number of particles to high velocity zone, and particles experience heterogeneous velocity field and slowly converges to stationary velocity field.

To further investigate Lagrangian transport behavior, we analyze individual particle trajectories. The temporal evolution of the Lagrangian velocity and acceleration for a particle indicate strongly intermittent behavior, both in the longitudinal (x) and the transverse (y, z) directions of the flow, alternating between long periods of stagnation and bursts of high variability [Fig. 2-5(a)(b)]. Similar intermittent behavior in the longitudinal direction has been observed in a 2D porous medium consisting of a random distribution of disks [35]. In the transverse direction, particles with high positive velocities jump to high negative velocities—an anticorrelation that was also observed in the particle transport through simple lattice networks [78].

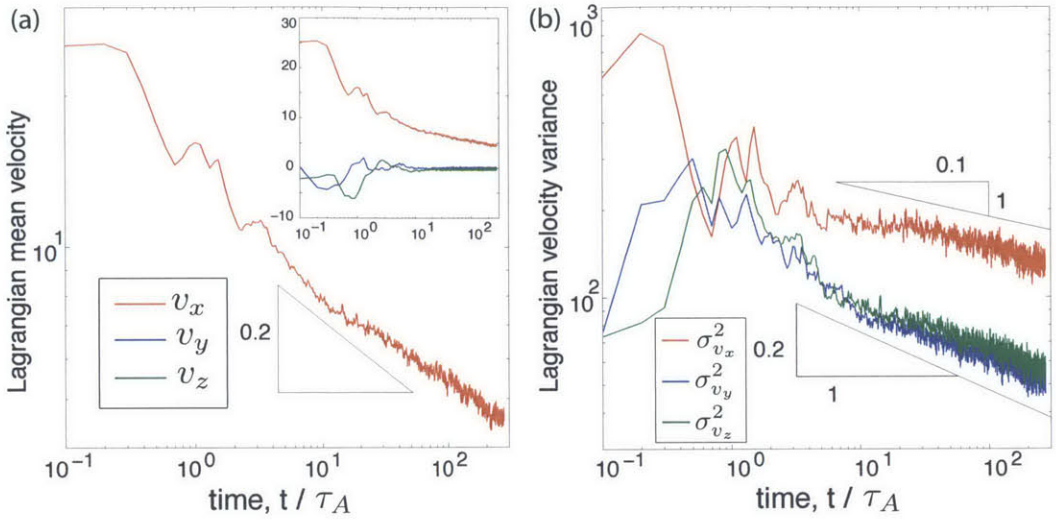

Figure 2-4: (a) Time evolution of Lagrangian mean velocity. Longitudinal Lagrangian velocity follows power 0.2 and in transverse directions Lagrangian mean velocity converges to 0. (b) Time evolution of Lagrangian velocity variance. Both longitudinal and transverse direction exhibits power law decay with respective power 0.1 and 0.2.

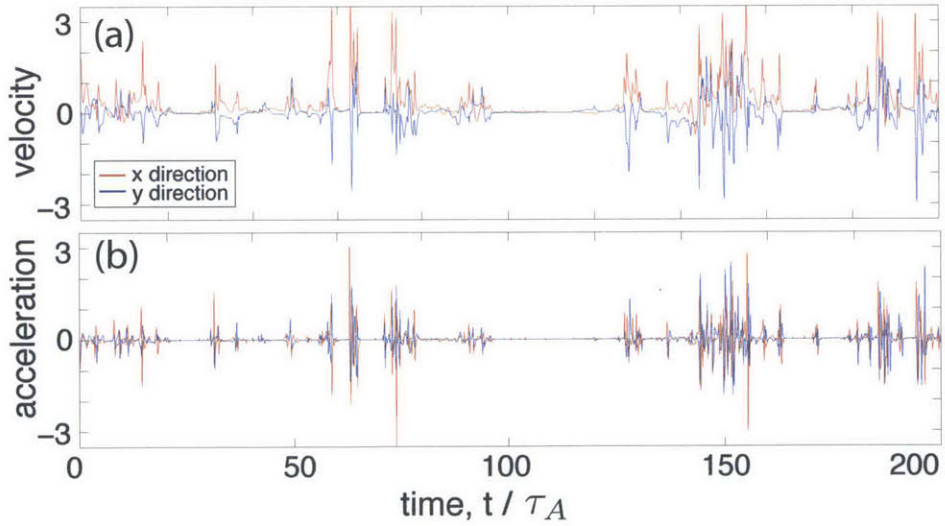

Figure 2-5: (a) and (b) Time series of the normalized Lagrangian velocity and acceleration, respectively, for the blue particle trajectory in Fig. 2-2(a). The Lagrangian statistics exhibit strongly intermittent behavior in both longitudinal and transverse directions.

2.3 Non-Fickian spreading and intermittency

To investigate the impact of the observed intermittent behavior of individual particles on the macroscopic spreading of the ensemble of particles, we compute the time evolution of the longitudinal and transverse mean square displacements (MSD) with respect to the center of mass of a point injection, i.e., initializing every particle's starting position to an identical reference point. For the longitudinal direction (x), the MSD is given by $\sigma_x^2(t) = \langle (x(t) - \langle x(t) \rangle)^2 \rangle$ where $\langle \cdot \rangle$ denotes the average over all particles. The same definition is applied to the transverse directions to compute σ_y^2 and σ_z^2. At early times, longitudinal MSD exhibits ballistic scaling, $\sigma_x^2 \sim t^2$, characteristic of perfectly correlated stratified flows [141]. After this initial period, the MSD follows a non-Fickian *superdiffusive* scaling $\sigma_x^2(t) \sim t^{1.5}$. The MSD in the transverse directions also scales as $\sigma_y^2, \sigma_z^2 \sim t^2$ at early times but, in contrast, then slows down to an asymptotic non-Fickian *subdiffusive* scaling $\sigma_y^2, \sigma_z^2 \sim t^{0.8}$ (Fig. 2-6).

Our hypothesis is that the observed non-Fickian anomalous spreading is a consequence of the observed intermittent behavior in the Lagrangian velocity. To quantify the intermittent behavior, we compute the velocity increment probability density function (PDF). The Lagrangian velocity increment associated to a time lag τ is defined as $\Delta_\tau v = v(t+\tau) - v(t)$ where $v(t) = [x(t+\tau) - x(t)]/\tau$. The velocity increments are rescaled with respect to their standard deviation, $\Delta_\tau v / \sigma_{\Delta_\tau v}$. We find that the velocity increment PDFs in both the longitudinal and transverse directions collapse (Fig. 2-7(a)); an indication that intermittent behavior is equally significant in all directions. This multidimensional intermittency originates from the combined effect of the 3D pore structure and the divergence-free constraint on the velocity field, which results in a misalignment between the local velocity and the mean flow direction. The PDF of the velocity increments is characterized by a sharp peak near zero, and exponential tails. The peak reflects the trapping of particles in stagnation zones, while the exponential tails indicate that large velocity jumps are also probable due to the strong heterogeneity in the velocity field—a signature of the observed intermittency [35, 34]. As τ increases, the slope of tail increases and the peak becomes less prominent. However, even after four characteristic advective time, the velocity increment

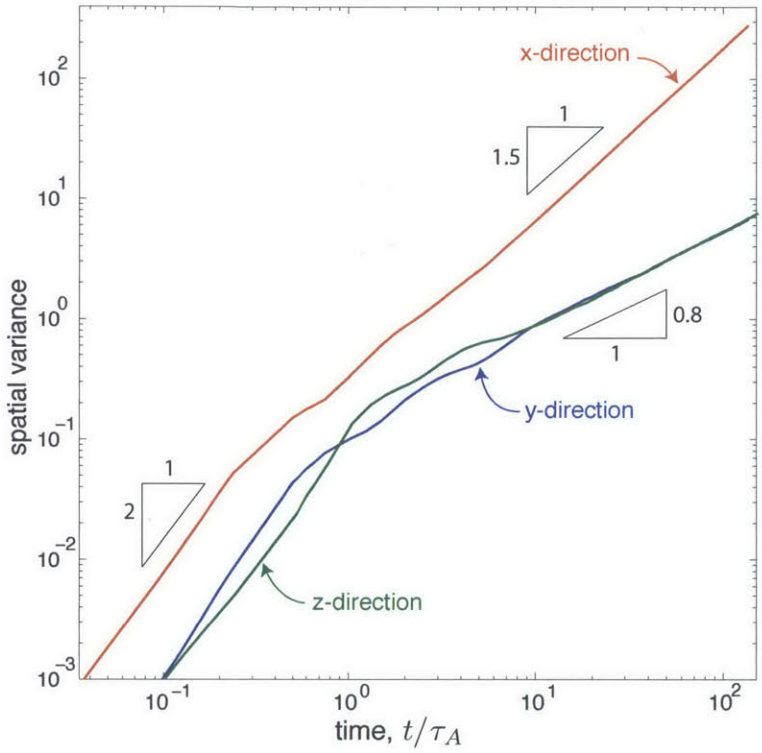

Figure 2-6: Time evolution of the centered second spatial moments from particle-tracking simulation. In the x-direction, particle dispersion is superdiffusive with slope ~ 1.5, and in the y and z directions, dispersion is subdiffusive with slope ~ 0.8.

PDF is still strongly non-Gaussian showing the persistent anomalous nature of the pore scale fluid transport (Fig. 2-7(b)). This non-Gaussian character indicates that pore-scale fluid flow cannot be modeled using the Langevin description with white noise [138].

2.4 Lagrangian velocity correlation structure and origin of anomalous transport

From velocity increment pdf, we observed signature of flow intermittency as the sharp peak near zero and exponential tails. The peak represents strong flow correlation due to stagnation zones, and exponential tail represents strong velocity fluctuation from heterogeneous velocity field. Now we formulate the time evolution of second spatial moments as a function of flow correlation and flow heterogeneity to investigate their respective impact on particle spreading.

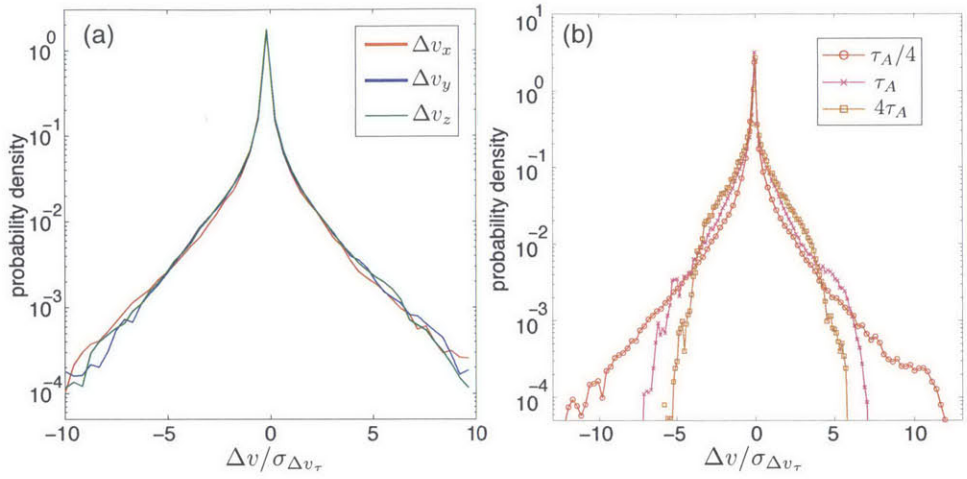

Figure 2-7: (a) Probability density distributions of the normalized Lagrangian velocity increments in x, y and z directions, for a time lag $\tau = \tau_A/4$. Velocity increments are normalized with respect to their standard deviation σ_{vi}, $i = x, y, z$. (b) Change in probability distributions for different time lags. The tailing decreases as the time lag increase, but the distribution is still non Gaussian even for the lag time of $4\tau_A$.

Let $\chi_v(\tau, \eta)$ be the velocity autocorrelation between times τ and η,

$$\chi_v(\tau, \eta) = \frac{\langle [v(\tau) - \langle v(\tau) \rangle][v(\eta) - \langle v(\eta) \rangle] \rangle}{\sigma_v(\tau)\sigma_v(\eta)}, \tag{2.1}$$

where $\sigma_v^2(\eta)$ is the variance of the Lagrangian velocity at time η. Velocity autocorrelation functions at different τ values in longitudinal and transverse direction (Fig. 2-8) shows long range correlation in longitudinal direction and short range correlation in transverse direction.

From the definition of the MSD [3], we can express MSD as,

$$\sigma_x^2(t) = 2 \int_0^t d\eta\, \sigma_v(\eta) \int_0^\eta d\tau\, \sigma_v(\tau) \chi_v(\tau, \eta). \tag{2.2}$$

When the velocity standard deviation, $\sigma_v(\tau)$, follows slow decay in time with respect to $\chi_v(\tau, \eta)$ (we confirmed this), the MSD can be approximated as

$$\sigma_x^2(t) \approx 2 \int_0^t d\eta\, \sigma_v^2(\eta) \int_0^\eta d\tau\, \chi_v(\tau, \eta). \tag{2.3}$$

To study the independent roles of velocity heterogeneity and velocity correlation on spread-

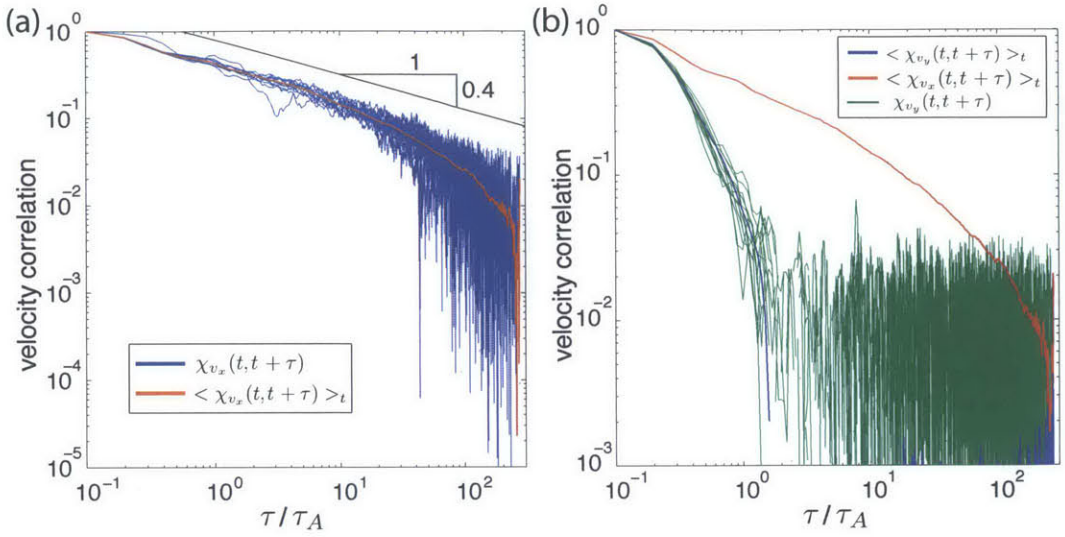

Figure 2-8: (a) Longitudinal Lagrangian velocity autocorrelation, $\chi_{v_x}(t, t+\tau)$, for multiple t values. We can observe the fluctuation of velocity autocorrelation functions with respect to the average autocorrelation function, $< \chi_{v_x}(t, t+\tau) >_t$, due to the nonstationarity of the Lagrangian statistics. (b) Transverse Lagrangian velocity autocorrelation (green), $\chi_{v_y}(t, t+\tau)$, for multiple t values.

ing, we define $\Psi_v(t) = \int_0^t d\eta\, \sigma_v^2(\eta)$ and $\Phi_v(t) = \int_0^t d\eta \int_0^\eta d\tau\, \chi_v(\tau, \eta)$, respectively. In both longitudinal and transverse direction, neither velocity heterogeneity nor velocity correlation alone can explain the observed anomalous spreading in our system [Fig. 2-9(a)]. Therefore, advective particle spreading is determined by the interplay between velocity heterogeneity and velocity correlation.

To study velocity autocorrelation structure in time and space, we compute the average velocity autocorrelation as a function of *time* and *space* [Fig. 2-9]. From our qualitative and quantitative analysis of intermittency in the Lagrangian statistics [Fig. 2-5 and Fig. 2-7, respectively], it is not surprising that the longitudinal velocity autocorrelation, χ_{v_x}, is slow-decaying in time [Fig. 2-9(b), inset]. Moreover, while the transverse velocity autocorrelation, χ_{v_y}, decays faster in time, this does not mean that it has short-range correlation; indeed, the absolute magnitude of the transverse velocity, $|v_y|$, exhibits broad-range temporal autocorrelation [Fig. 2-9(b), inset], highlighting the crucial fact that the transverse velocity is mean-reverting but strongly correlated in time—a phenomenon also observed in turbulence for velocity increments [106].

The Lagrangian correlation structure is drastically different as a function of space, in-

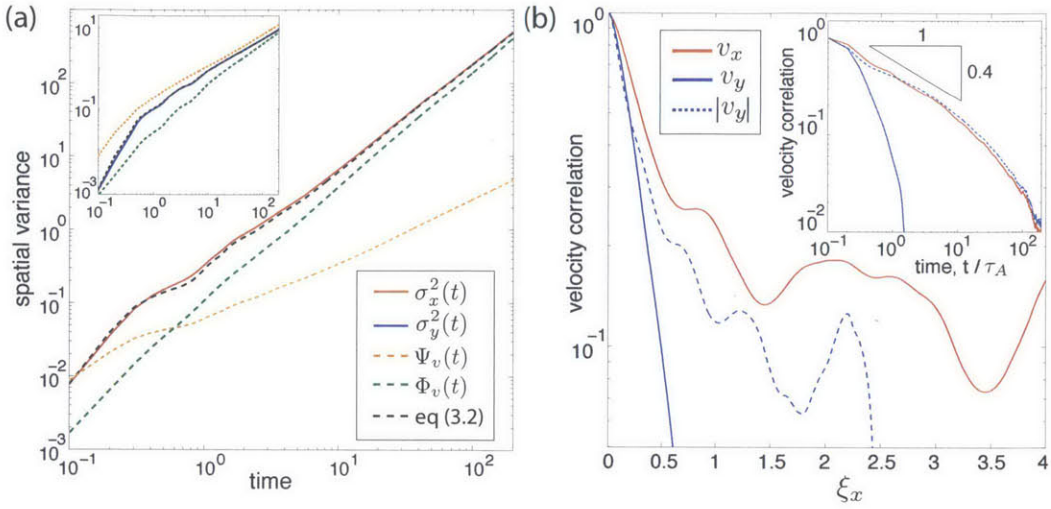

Figure 2-9: (a) Time evolution of the centered second spatial moments in the longitudinal direction from particle tracking simulation (solid line), prediction from eq (2.3) (black dotted line), and estimations from velocity heterogeneity alone ($\Psi_v(t)$, orange dotted line) and velocity correlation alone ($\Phi_v(t)$, green dotted line). The orange and green lines are shifted along the y axis for clarity. Inset: Time evolution of the centered second spatial moments in the transverse direction. (b) Longitudinal (x, red) and transverse (y, blue) Lagrangian velocity autocorrelation as a function of *space* along the longitudinal direction. All functions are short-ranged. Inset: Longitudinal (red) and transverse (blue) Lagrangian velocity autocorrelation as a function of *time*. Note the strong, long range, correlation of the longitudinal velocity v_x and the absolute value of the transverse velocity, $|v_y|$.

stead of time—a key insight first pointed out in [90] for Darcy flow in heterogeneous media. The longitudinal and transverse velocity autocorrelation, as a function of space ξ_x, are all short-ranged and decay exponentially [Fig. 2-9(b)].

2.5 Continuous time random walk model

The exponential decay of autocorrelation is characteristic of Markov processes [125], which suggests that the effective pore scale velocity transitions in space can be captured by a one-step correlated model in space. We propose a correlated CTRW macroscopic model [90, 142], where the velocity heterogeneity structure and the one-step velocity correlation are characterized by a velocity transition matrix derived from the pore scale 3D simulations [90, 78]. The velocity transition matrix is the only input to our model.

We denote by $r_m(v_\zeta|v'_\zeta)$ the transition probability density to encounter a velocity v_ζ

after $n + m$ steps given that the particle velocity was v'_ζ after n steps (here ζ refers to any of the space directions, x, y, z). To evaluate the discrete transition probability from the simulated 3D particle trajectories, we discretize the particle velocity distribution into $N = 100$ classes with equiprobable binning, $v_\zeta \in \bigcup_{j=1}^{N}(v_\zeta^j, v_\zeta^{j+1})$, and define the m-step transition probability matrix:

$$T_m(k|j) = \int_{v_\zeta^k}^{v_\zeta^{k+1}} dv_\zeta \int_{v_\zeta^j}^{v_\zeta^{j+1}} dv'_\zeta \, r_m(v_\zeta|v'_\zeta)p(v'_\zeta) \Big/ \int_{v_\zeta^j}^{v_\zeta^{j+1}} dv'_\zeta p(v'_\zeta), \tag{2.4}$$

where $p(v'_\zeta)$ is velocity probability distribution function. The one-step velocity transition matrix (T_1), in longitudinal and transverse directions, is shown in Fig. 2-10. For the longitudinal direction, the high probabilities along the diagonal of T_1 reflect the strong persistence in the magnitude of longitudinal velocity. For the transverse direction, this effect is also present, but in addition we observe high probability values along the opposite diagonal, as a result of the transverse velocity anticorrelation due to local flow reversal [Fig. 2-2(d)].

Average particle motion can be described by the following system of Langevin equations:

$$\zeta_{n+1} = \zeta_n + \Delta\zeta \frac{v_\zeta(n\Delta\zeta)}{|v_\zeta(n\Delta\zeta)|}, \quad t_{n+1} = t_n + \frac{\Delta\zeta}{|v_\zeta(n\Delta\zeta)|}, \tag{2.5}$$

where $\zeta = x, y, z$. We choose $\Delta x = \lambda_c/4$, $\Delta y = \lambda_c/8$ and $\Delta z = \lambda_c/8$, based on the characteristic correlation length of the exponential decay of the spatial velocity autocorrelation [Fig. 2-9(a)]. We assume that the sequence of Lagrangian velocities $\{v_\zeta(n\Delta\zeta)\}_{n=0}^{\infty}$ can be approximated by a Markov process, and thus fully characterized by the one-step transition probability density T_1 (Fig. 2-10). Particles start with initial velocities chosen randomly from the velocity distribution and the velocity transition is determined probabilistically following the one-step transition matrix.

The proposed correlated CTRW model accurately predicts the plume evolution in all space directions, as evidenced by the longitudinal and the transverse projections of particle density at fixed times and by the MSDs in both longitudinal and transverse directions (Fig. 2-11). The model captures nicely the early ballistic regime, the late time scaling,

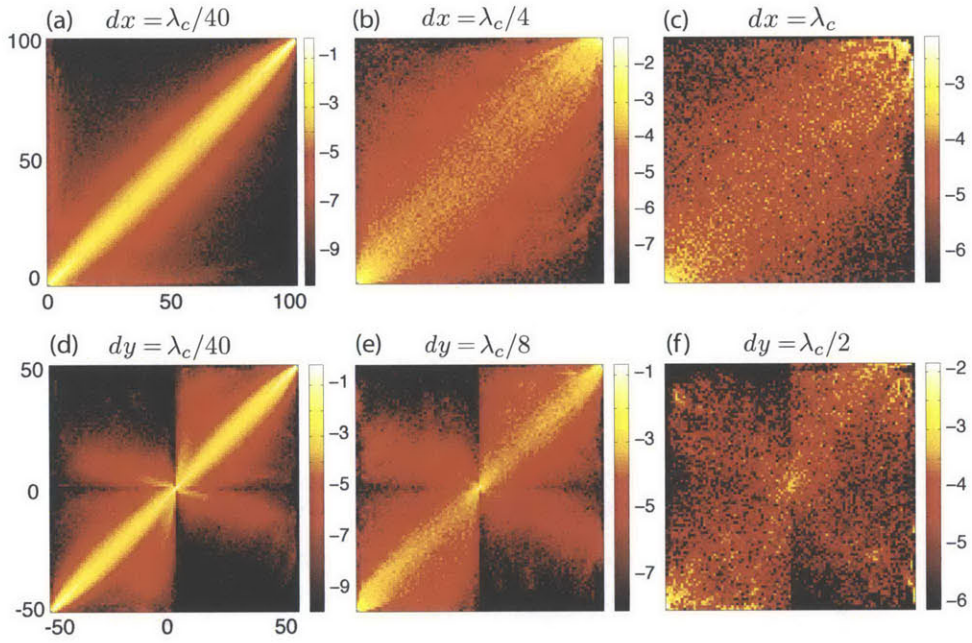

Figure 2-10: (a,b,c) Longitudinal (x) transition matrix with $N = 100$ velocity classes for different values of the space transition $\Delta x/\lambda_c$. The velocity correlation decreases as the sampling distance Δx increases. (d,e,f) Transverse (y) transition matrix with $N = 100$ velocity classes for different Δy values. We assign 50 bins for positive velocity and another 50 for negative velocity. The z-directional transition matrix is almost identical to y-directional transition matrix.

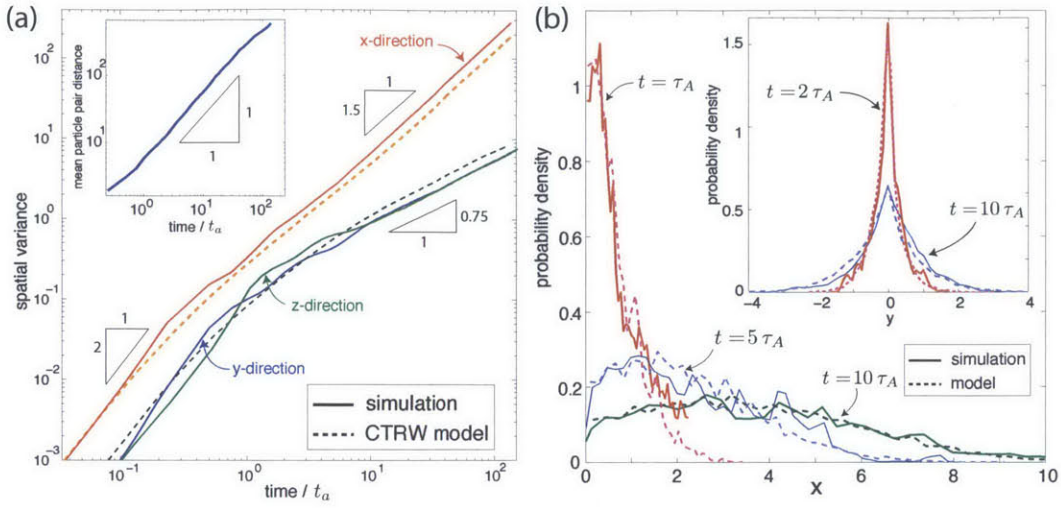

Figure 2-11: (a) Time evolution of the centered second spatial moments from particle-tracking simulation (solid line) and the prediction with correlated CTRW (dotted line). Inset: Time evolution of the mean particle pair distance. We do not see the exponential increase in the particle pair distance up to $100\tau_A$. Therefore, chaotic advection is not the mechanism for anomalous transport. (b)Longitudinal projection of the particle density distribution at fixed times ($t = \tau_A, 5\tau_A$ and $10\tau_A$) from direct pore-scale simulation (solid line), and the correlated CTRW model prediction (dotted line). Inset: Transverse projection of the particle density distribution at fixed times ($t = 2\tau_A$ and $10\tau_A$) from direct simulation (solid line) and the respective CTRW model prediction (dotted line). Different colors indicate different times.

and the transition time, without any fitting parameters. Recently, it has been demonstrated that the chaotic advection is inherent to the porous media flow [94]. To investigate the existence of chaotic advection in our porous media system, we compute the time evolution of average particle pair distance as shown in the inset of Figure 2-11(a). At least at the time scale of our interest, we can not observe the exponential increase in the particle pair distance. Therefore, we can confirm that the velocity correlation is the main driver for the anomalous transport rather than the chaotic advection in our system.

Taken together, our findings point to the critical role of velocity intermittency at the pore scale on transverse particle spreading and, consequently, on mixing and reactive transport processes in porous media flows.

2.6 Impact of particle injection rule: flux weighted injection vs volume injection

In previous chapters, we have used flux weighted (proportional) injection, where the number of injected particle in each pore space is proportional to local flux, as an initial particle placement rule. In this section, we compare the *flux weighted* injection case with *volume injection* case. We define *volume injection* as injecting equal number of particles in each pore space. Both injection scenarios can occur in real porous media flow. For example, to understand the underground contaminant flow characteristics, volume injection is relevant since contaminants occupy pore space equally. However, when we artificially inject tracer into groundwater system, flux weighted injection is more relevant since more number of tracers will be injected at high flux zone. We compare two injection cases to study the impact of injection rule on spreading and to show the generality of our framework by applying it to two different cases.

Since volume injection has much more number of particles in stagnation zones, Lagrangian mean velocity is significantly faster for flux weighted injection ($8.70\ \mu$m/s) compared to volume injection ($4.84\ \mu$m/s). When the underlying flow field is stationary, the volume injection gives stationary Lagrangian statistics since the ensemble of particles represent stationary flow field. For flux weighted injection, particles in the preferential path get trapped and this causes decrease in Lagrangian mean velocity in time. Lagrangian velocity distribution computed at every t_A shows stationary distribution for volume injection and strongly time dependent distribution for flux weighted injection (Fig. 2-12(a)). The average Lagrangian velocity distribution for flux weighted injection shows smaller probability to sample small velocities (Fig. 2-12(b)). As shown in Figure 2-13, both first and second moments of velocity are much less time dependent for volume injection case compared to flux weighted injection case.

We now investigate the impact of injection rule on macroscopic spreading behavior. There are three main interesting differences between the two cases (Fig. 2-14). First, we can clearly observe that the spreading is smaller for volume injection case compared to flux weighted injection case. Second, transition from ballistic to anomalous scaling occurs

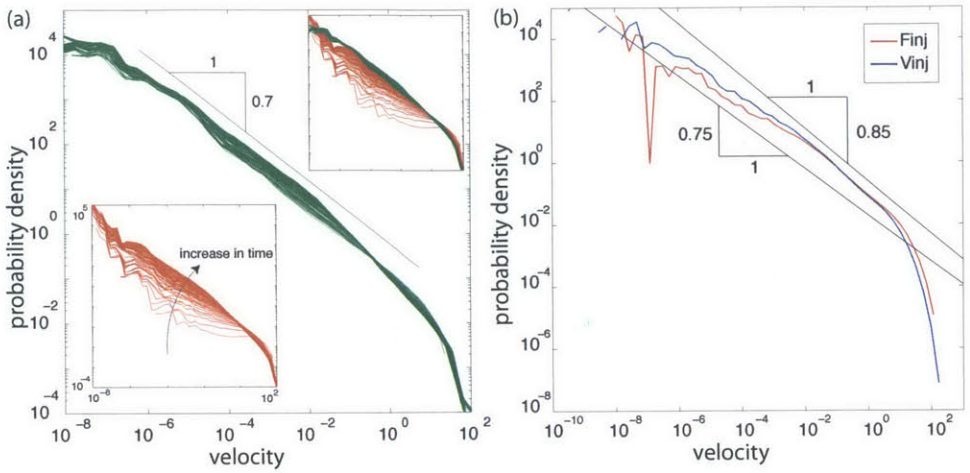

Figure 2-12: (a) Comparison of Lagrangian velocity probability density functions at every t_a for volume injection and flux weighted injection. We can clearly observe the Lagrangian statistics for flux weighted injection case is nonstationary. (b) Comparison of probability density functions of x-directional Lagrangian velocities sampled equidistance in time for volume injection and flux weighted injection.

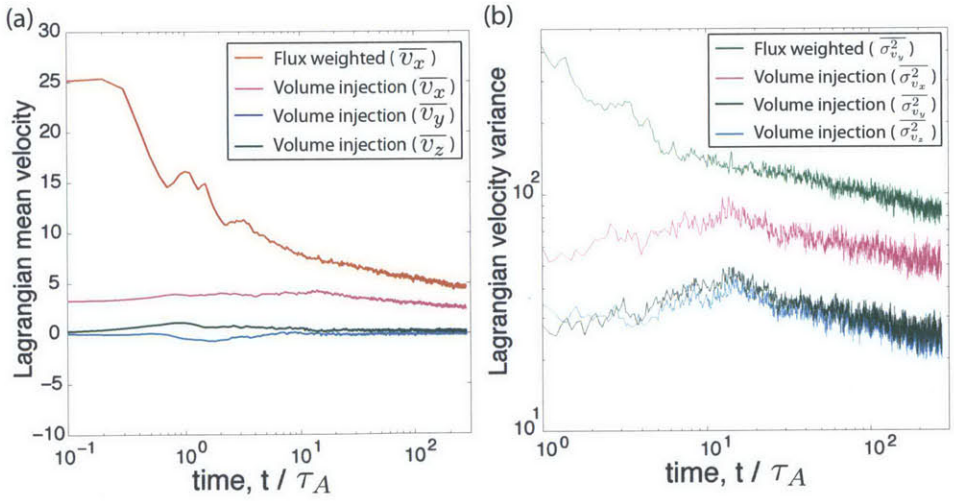

Figure 2-13: (a) Time evolution of Lagrangian mean velocity for volume injection case. Mean velocity is approximately constant over time. (b) Time evolution of Lagrangian velocity variance. Both longitudinal and transverse direction shows no dependence in time.

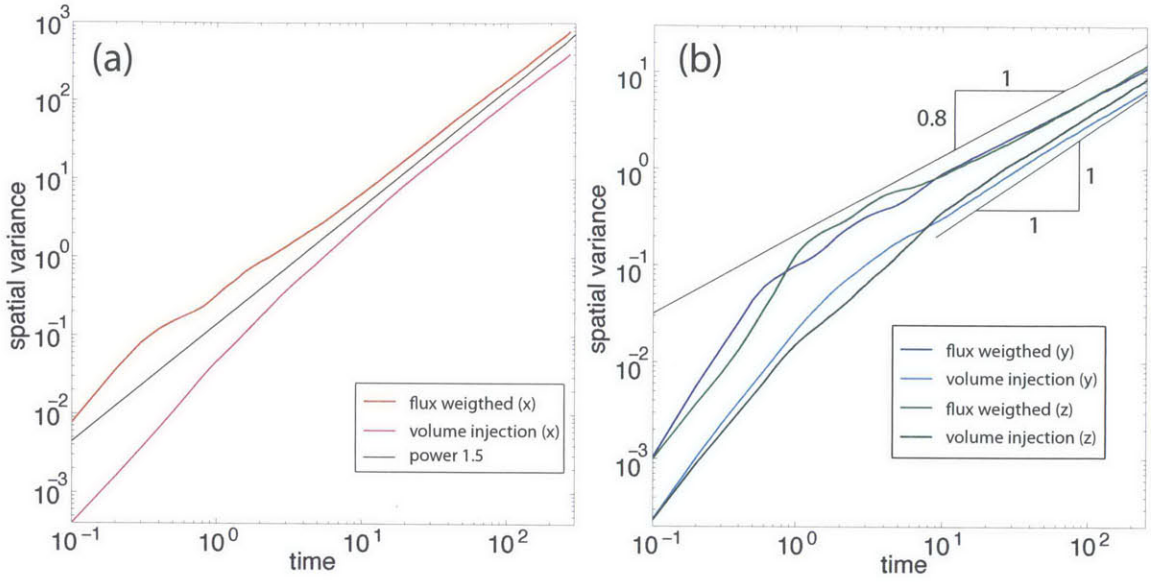

Figure 2-14: MSD for two different injection rules. We can observe clear difference between the two cases.

later in time for volume injection case. Third, anomalous scaling in longitudinal direction converges to $\sigma_x^2(t) \sim t^{1.5}$ for both cases. However, in transverse direction, volume injection shows normal scaling, $\sigma_y^2(t) \sim t^1$, whereas flux weighted injection shows subdiffusive scaling, $\sigma_y^2(t) \sim t^{0.8}$.

We now compare velocity autocorrelation for the two difference injection rules. Velocity autocorrelation for volume injection case has stronger correlation (Fig. 2-15). This originated from particles in stagnation zones. Velocity of a particle in stagnation zone has strong correlation for long time as shown in the single particle trajectory (Fig. 2-5). Since volume injection has much more number of particles in stagnation zones, velocity autocorrelation for volume injection case has stronger correlation in time.

To investigate the role of velocity correlation and velocity heterogeneity on particle spreading, we now further develop eq (2.3). For second order stationary velocity process, $\sigma_v^2(t) = \sigma_v^2$ and $\chi_v(t_1, t_2) = \chi_v(t_2 - t_1)$. Therefore, we can further simplify eq (2.3) as,

$$\sigma_x^2(t) \approx 2\sigma_v^2 \int_0^t d\eta \int_0^\eta d\tau \, \chi_v(\tau). \tag{2.6}$$

The prediction from eq (2.6) shows excellent match with the particle tracking simu-

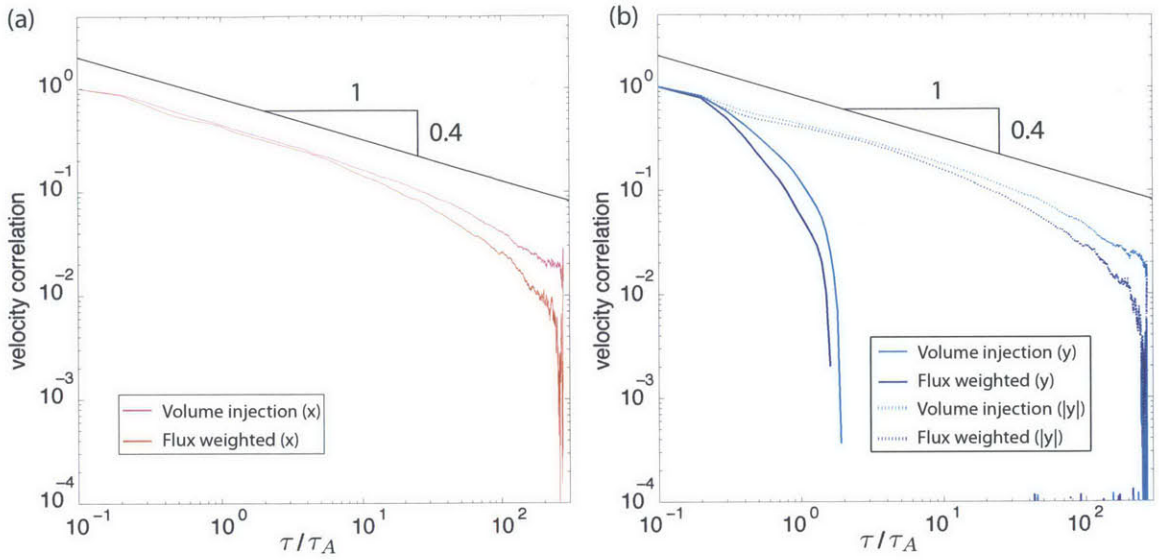

Figure 2-15: Velocity autocorrelation for the two different injection rules. Volume injection case shows stronger correlation for both longitudinal and transverse directions.

lation in all directions (Fig. 2-16(a)). Also, we confirmed that eq (2.6) fails to predict flux-weighted injection case since eq (2.6) requires second order stationary process. The generality of correlated CTRW model can be tested by applying it to volume injection case. As shown in Figure 2-16(b), correlated CTRW accurately predicts particle spreading at all times showing the general applicability of our model. The Markovianity assumption can be also understood by comparing transition matrices in time and in space (Fig. 2-17). Due to the long range velocity correlation in time for particles in stagnation zones, velocity transition in time shows strong correlation for small velocities and cannot be approximated as Markov process.

2.7 Effective correlated CTRW

In CTRW, $\psi(t)dt$ is defined as the ensemble averaged probability of a particle experiencing transition time t [41]. $\psi(t)$ can be obtained by measuring the distribution of Lagrangian velocity sampled in space. Figure 2-18 shows Lagrangian transition time distribution sampled in space and in time for two different injection rules. $\psi(t)$ for CTRW should be measured with volume injection and sampled in space.

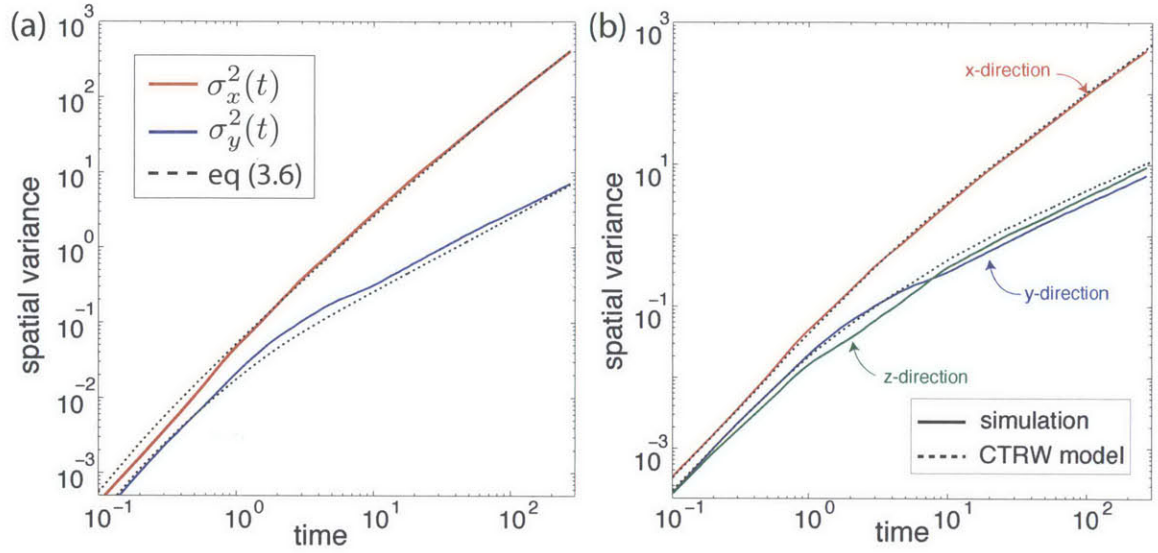

Figure 2-16: (a) Time evolution of the centered second spatial moments from particle tracking simulation (solid line), and predictions from eq (2.6) (black dotted line). (b) Time evolution of the centered second spatial moments from particle-tracking simulation (solid line) and the prediction with correlated CTRW (black dotted line).

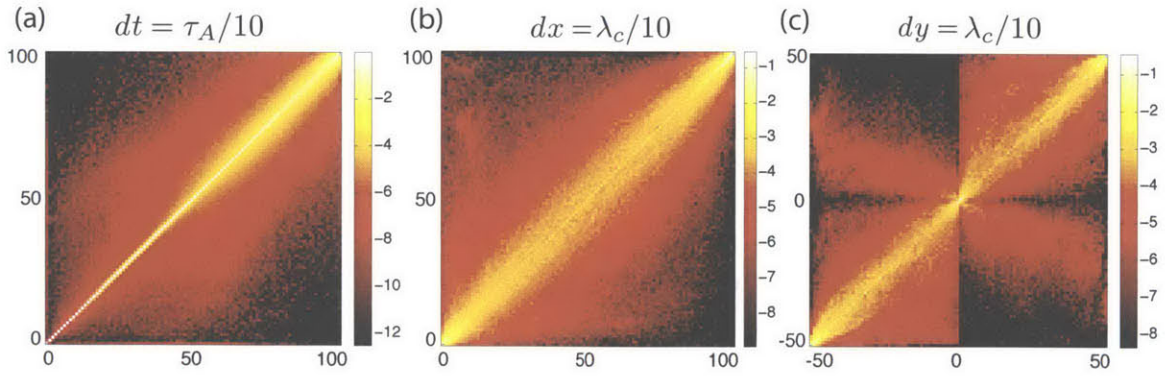

Figure 2-17: Transition matrices for uniform injection case. In time, velocities are very strongly correlated for small velocities due to the particles in stagnation zones. We have symmetric transition matrix in space.

We can also relate the probability density function of the velocity $p(v)$ and time $\psi(t)$ as following. Say $p(v) \sim v^{\alpha}$ and $\psi(t) \sim t^{-1-\beta}$. From $\psi(t)dt = p(v)dv$ and $dt = \frac{1}{v^2}dv$, we can relate α and β as $\beta = \alpha + 1$. We observed $\alpha = -0.75$ for Lagrangian velocity distribution sampled in equidistance in time (Fig. 2-12(b)). This is equivalent to $\beta = 0.25$ which is consistent with Figure 2-18(a).

The transition time distribution for CTRW should be sampled equidistance in space which gives $\beta = 0.8$ (Figure 2-18(a)). In CTRW theory, for $\beta < 1$, $\sigma^2 \sim t^{2\beta}$ in longitudinal direction and $\sigma^2 \sim t^{\beta}$ in transverse direction. Therefore, CTRW theory predicts $\sigma_x^2 \sim t^{1.6}$ and $\sigma_y^2 \sim t^{0.8}$. This is consistent with what we observed for flux-weighted injection but not for volume injection where $\sigma_y^2 \sim t^1$. The CTRW theory explains scaling of second spatial moments only with velocity distribution. However, we showed that the anomalous transport originates from the interplay between velocity heterogeneity and correlation (eq (2.3)).

To reduce the number of parameters in the developed correlated CTRW model, we simplify the model with two independent parameters: β that characterizes velocity heterogeneity and λ that characterizes velocity correlation. β can be measured from the distribution of Lagrangian transition times sampled in space where we observed as 0.8. λ determines characteristic correlation length which can be measured from either transition matrix or velocity autocorrelation function. The full description of the simplified model can be found in 4.4.3. As can be seen in the Figure 2-18(b), the model accurately captures the spatial spreading at all times with $\beta = 0.8$ and $\lambda = 2\lambda_c$. β determines late-time scaling and λ determines the transition from ballistic to anomalous scaling.

2.8 Discussion

We have identified the pore-scale origin of anomalous transport as the competition between flow correlation and flow heterogeneity. From the understanding of the origin of anomalous transport, we have successfully developed predictive transport model that properly honors flow heterogeneity and correlation. We further simplified the developed model by reducing the number of parameters to two: one for heterogeneity and one for correlation. Now we study the generality of our finding in the following chapter.

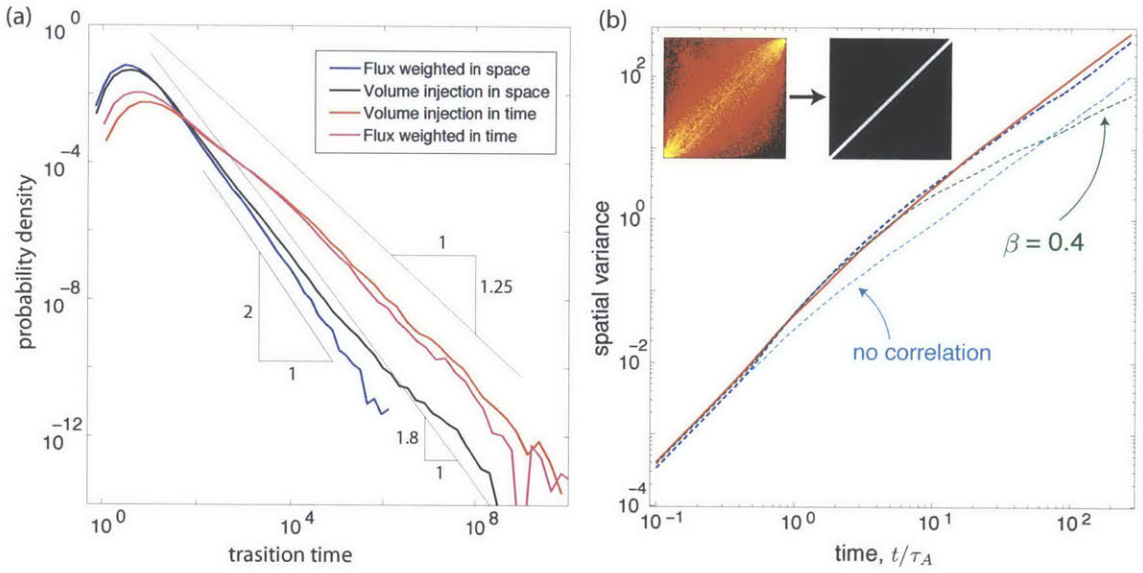

Figure 2-18: (a) Probability density distribution of particle transition times. Transition times sampled at equidistance in time and equidistance in space gives dramatic difference in the probability distribution. To apply CTRW theory, the proper transition time distribution is the one with volume injection and sampled equidistance in space. (b) Time evolution of the centered second spatial moments from particle tracking simulation (solid line), and predictions using effective correlated CTRW (black dotted line). inset: measured transition matrix and simplified transition matrix.

Chapter 3

Anomalous transport through lattice fracture networks

3.1 Background

Anomalous transport, understood as the nonlinear scaling with time of the mean square displacement of transported particles, is observed in many physical processes, including contaminant transport through porous and fractured geologic media [10], animal foraging patterns [147], freely diffusing molecules in tissue [155], tracer diffusion in suspensions of swimming micro-organisms [93], and biased transport in complex networks [111].

Anomalous transport often leads to a broad-ranged particle distribution density, both in space and time [135, 18, 102]. Understanding the origin of the slow-decaying tails in probability density is essential, because they determine the likelihood of high-impact, "low-probability" events and therefore exert a dominant control over the predictability of a system [77]. This becomes especially important when human health is at risk, such as in epidemic spreading through transportation systems [2] or radionuclide transport in the subsurface [104].

Past studies have shown that high variability in the flow properties leads to anomalous transport [18, 10]. Depending on the nature of the underlying disorder distribution anomalous behavior can be transient or persist to asymptotic scales [143, 41]. The continuous time random walk (CTRW) formalism [129, 87] offers an attractive framework to under-

stand and model anomalous transport through disordered media and networks [8, 10, 111]. The CTRW model is intrinsically an annealed model because the disorder configuration changes at each random-walk step. A particle that returns to the same position experiences different velocity properties. The validity of the CTRW approach for average transport in quenched random environments has been studied for purely diffusive transport [e.g., 18] and biased diffusion [e.g., 90, 40, 39, 77]. Most studies that employ the CTRW approach assume that transition times associated with particle displacements are independent of each other, therefore neglecting velocity correlation between successive jumps [9]. Indeed, a recent study of transport on a lattice network has shown that CTRW with independent transition times emerges as an exact macroscopic transport model when velocities are uncorrelated [77].

However, detailed analysis of particle transport simulations demonstrates conclusively that particle velocities in mass-conservative flow fields exhibit correlation along their spatial trajectory [5, 90, 103]. Mass conservation induces correlation in the Eulerian velocity field because fluxes must satisfy the divergence-free constraint at each intersection. This, in turn, induces correlation in the velocity sequence along a particle trajectory. To take into account velocity correlation, Lagrangian models based on temporal [115, 103] and spatial [5, 90] Markovian processes have recently been proposed. These models successfully capture many important aspects of the Lagrangian velocity statistics and the particle transport behavior. In particular, the study of Le Borgne et al. [90] shows that introducing correlation in the Lagrangian velocity through a Markov process in space yields an accurate representation of the first and second moments of the particle density. The model is restricted, however, to particle trajectories projected onto the direction of the mean flow, and the study leaves open the question of whether spatial Markov processes can describe multidimensional features of transport.

Here, we investigate average transport in divergence-free flow through a quenched random lattice from the CTRW point of view. We introduce a multidimensional spatial Markov model for particle velocity, and confirm that the model exhibits excellent agreement with Monte Carlo simulations. We show that accounting for the spatial correlation in the Lagrangian velocity is essential to capture the fundamental macroscopic transport behavior.

3.2 Random Lattice Network

We consider a lattice network consisting of two sets of parallel, equidistant links oriented at an angle of $\pm\alpha$ with the x-axis. The distance between nodes is l [Fig. 3-1]. Flow through the network is modeled by assuming Darcy's law [3] for the fluid flux u_{ij} between nodes i and j, $u_{ij} = -k_{ij}(\Phi_j - \Phi_i)/l$, where Φ_i and Φ_j are the flow potentials, and $k_{ij} > 0$ is the conductivity of the link between the two nodes. Imposing mass conservation at each node i, $\sum_j u_{ij} = 0$, leads to a linear system of equations, which is solved for the flow potentials at the nodes [Fig. 3-2]. A link from node i to j is incoming for $u_{ij} < 0$ and outgoing for $u_{ij} > 0$. We denote by $\mathbf{e}_{ij}$ the unit vector in the direction of the link connecting i and j. A realization of the random lattice network is generated by assigning independent and identically distributed random conductivities to each link. Therefore, the k values in different links are uncorrelated. The set of all realizations of the quenched random network generated in this way form a statistical ensemble that is stationary and ergodic. To study the impact of the network heterogeneity on transport, we take log-normal distribution for k distribution and the variance of the log-normal distribution determines the heterogeneity.

We study a simple flow setting of mean flow in the positive x-direction, by imposing a no-flow condition at the top and bottom boundaries of the network, and fixed values of the potential at the left ($\Phi = 1$) and right ($\Phi = 0$) boundaries.

Once the fluxes at the links are known, we simulate transport of a passive tracer by particle tracking. We neglect diffusion along links, and thus particles are advected with the mean flow velocity between nodes. When particles arrive at nodes, they follow either complete mixing or streamline routing (no mixing) rules [Fig. 3-3]. The complete mixing assumes that Peclet numbers at nodes are very small that particles are well mixed within the link. Thus, the link through which the particle exits a node is chosen randomly with flux-weighted probability. For streamline routing, Peclet numbers at nodes are very high that particles essentially follow streamline and cannot jump between streamlines. The complete mixing and streamtube routing rules are the two extremes where the former is diffusion dominated and the latter is advection dominated. In reality, local Peclet number at node and the intersection geometry determines the strength of mixing at nodes that is somewhere

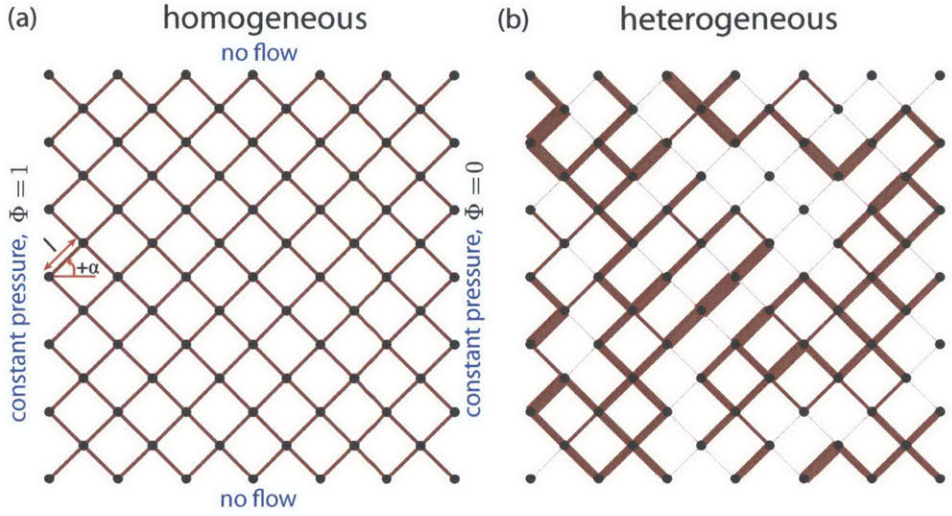

Figure 3-1: (a) Schematic of the homogeneous lattice network considered here, with two sets of links with orientation $\pm\alpha = \pm\pi/4$ and spacing $l = 1$. Boundary conditions are imposed to realize liner flow geometry. (b) Schematic of the heterogeneous lattice network.

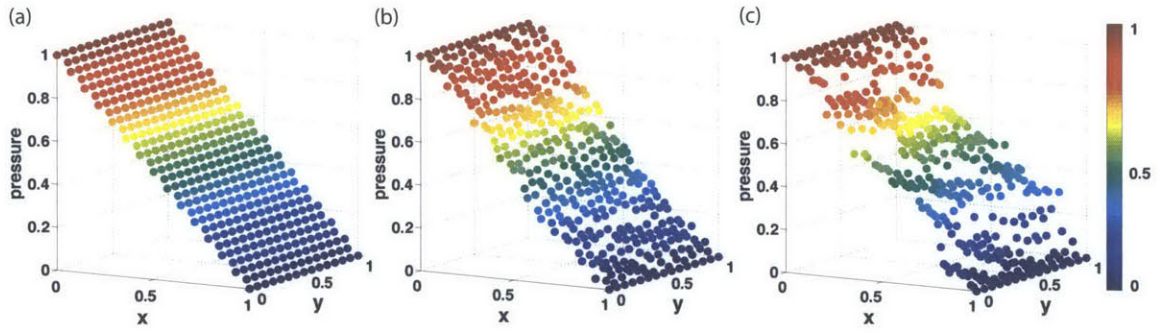

Figure 3-2: (a) Pressure field for log-normal conductivity distribution with variance 0, (b) Pressure field for log-normal conductivity distribution with variance 1 (c) Pressure field for log-normal conductivity distribution with variance 5.

between complete mixing and streamline routing.

Particle transfer probabilities from node i to node j (p_{ij}) for complete mixing is as follows:

$$p_{ij} = \frac{|u_{ij}|}{\sum_k |u_{ik}|}, \tag{3.1}$$

where the summation is over outgoing links only, and $p_{ij} = 0$ for incoming links. This implies that the particle transition is determined only with outgoing flux distribution and not the incoming fluxes. The equation (3.1) applies to the cases with three outgoing fluxes and one outgoing fluxes for both complete mixing and streamtube routing. However, for two outgoing fluxes, streamline routing has different transition probability as following.

$$p_{\text{adj}} = \begin{cases} 1, & u_{\text{adj}} > u_{\text{in}} \\ \frac{u_{\text{adj}}}{u_{\text{in}}}, & u_{\text{adj}} < u_{\text{in}} \end{cases} \qquad p_{\text{opp}} = \begin{cases} 0, & u_{\text{adj}} > u_{\text{in}} \\ \frac{u_{\text{in}} - u_{\text{adj}}}{u_{\text{in}}}, & u_{\text{adj}} < u_{\text{in}} \end{cases} \tag{3.2}$$

Figure 3-3 illustrates the dramatic difference between the two mixing rules. When the two incoming links and the two outgoing links have same fluxes, the particles from incoming link partitions equally into the two outgoing links for the complete mixing rule. However, for the streamline routing case, all of the particles transit to the adjacent link. Therefore, the local mixing at the node may lead to the different global spreading behavior.

The Langevin equations describing particle movements in space and time are

$$\mathbf{x}_{n+1} = \mathbf{x}_n + l\frac{\mathbf{v}(\mathbf{x}_n)}{|\mathbf{v}(\mathbf{x}_n)|}, \qquad t_{n+1} = t_n + \frac{l}{|\mathbf{v}(\mathbf{x}_n)|}. \tag{3.3}$$

If $\mathbf{x}_n$ is the position of the ith node, the transition velocity is equal to $\mathbf{v}(\mathbf{x}_n) = u_{ij}\mathbf{e}_{ij}$ with probability p_{ij} define in (3.1) and (3.2). The velocity vector $\mathbf{v}$ in the following is expressed in (ν, θ) coordinates, in which $\nu = |v|\cos(\varphi)/|\cos(\varphi)|$ is the velocity along a link with $\varphi = \arccos(v_x/|v|)$ and $\theta = \sin(\varphi)/|\sin(\varphi)|$, so that $\mathbf{v} = [\nu\cos(\alpha), |\nu|\theta\sin(\alpha)]^t$. Note that φ can only assume values in $\{-\alpha, \alpha, \pi - \alpha, \pi + \alpha\}$.

The system of discrete Langevin equations (3.3) describes coarse-grained particle transport for a single realization of the quenched random lattice. Particle velocities and thus tran-

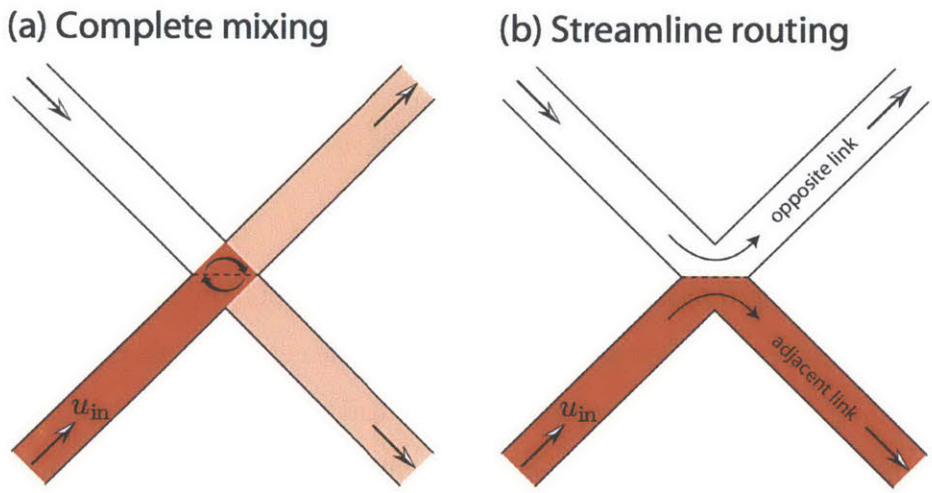

Figure 3-3: Schematic for the two different mixing rules when the two incoming links and the two outgoing links have same fluxes. (a) Complete mixing rule. (b) Streamline routing rule.

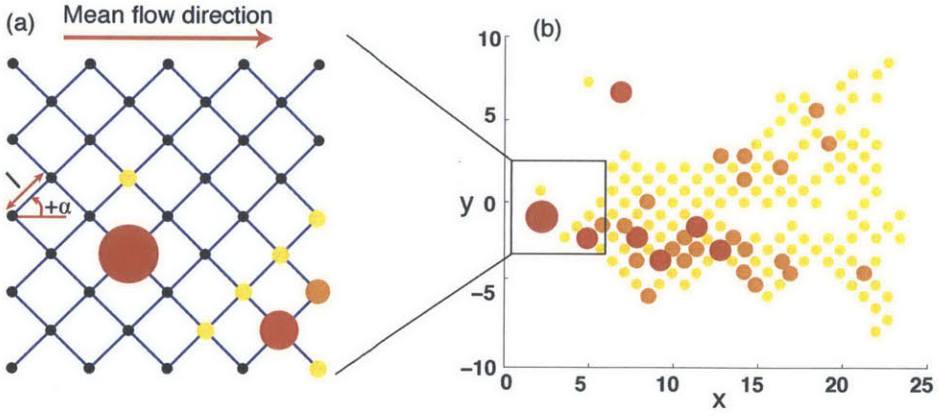

Figure 3-4: (a) Schematic of the lattice network considered here, with two sets of links with orientation $\pm\alpha = \pm\pi/4$ and spacing $l = 1$. (b) Particle distribution at nodes (represented by circles of different sizes) at $t = 30$ for a single realization after injection at the origin at $t = 0$.

sition times depend on the particle position. The particle position at time t is $\mathbf{x}(t) = \mathbf{x}_{n_t}$, where n_t denotes the number of steps needed to reach time t. The mean particle density is $P(\mathbf{x}, t) = \langle \delta(\mathbf{x} - \mathbf{x}_{n_t}) \rangle$, where the angular brackets denote both the noise average over all particles in one realization and the ensemble average over all network realizations. We solve transport in a single disorder realization by particle tracking based on Eq. (3.3) with the initial conditions $\mathbf{x}_0 = 0$ and $t_0 = 0$ [Fig. 3-4(b)]. From this, we obtain the mean particle density $P(\mathbf{x}, t)$ by ensemble averaging.

The fracture heterogeneity and mixing rule has significant impact on the evolution of mean particle density [Fig. 3-5]. Increase in heterogeneity increases particle spreading in both transverse and longitudinal directions. Impact of mixing rule is significant for networks with low heterogeneity. Complete mixing at nodes significantly enhances transverse spreading while longitudinal spreading is independent of the mixing rule.

3.3 Average Transport Behavior

We study the average transport behavior on lattice networks for a given conductivity distributions and mixing rules at nodes (either complete mixing or streamline routing). We run particle tracking simulations in 10^2 realizations of an ensemble of random lattices characterized by a lognormal k distribution with three different variance $\sigma^2_{\ln k} = 0.1, 1, 5$. The use of a lognormal distribution is motivated by measurements of conductivity in many natural media [128]. The lattice size is 51×51 nodes and, in each realization, we release 10^4 particles at the origin. The average transport behavior is studied in terms of the spatial particle density $P(\mathbf{x}, t)$, its mean square displacements in longitudinal and transverse directions and the distribution of the first passage time, $t_f(x)$, at a control plane at a distance x from the inlet.

Figure 3-6 shows the time evolution of the longitudinal and transverse spreading. In both directions, spreading shows ballistic regime ($\sim t^2$) at early time and evolves to anomalous scaling. The Monte Carlo simulation shows that the *longitudinal* mean square displacement (MSD) with respect to the center of mass evolves faster than linear with time (slope of $1.2 \sim 1.4$) [Fig. 3-6(a)(c)(e)]. There is no noticeable difference between complete

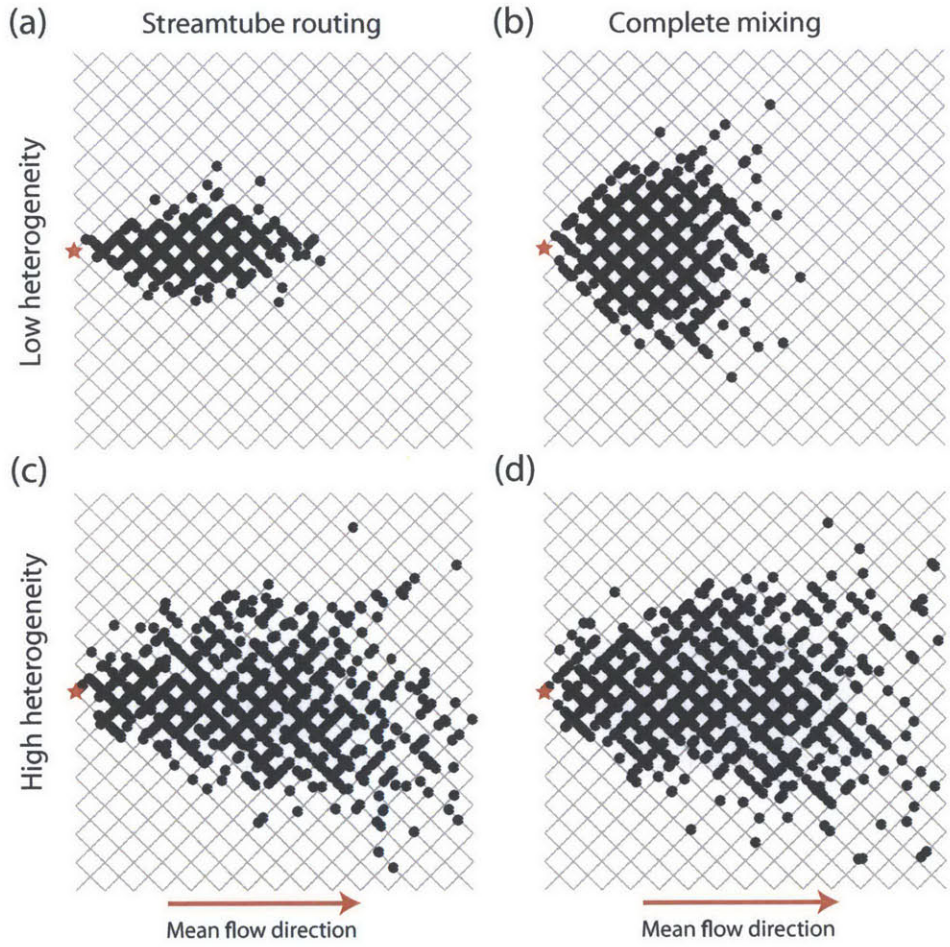

Figure 3-5: Particle distribution at fixed time after injection at the origin (red star). In low heterogeneity, transverse spreading significantly increases for complete mixing. Spreading is similar between streamtube routing and complete mixing for high heterogeneity.

mixing and streamline routing cases. However, increase in conductivity variance (heterogeneity) significantly increases MSD and we can also observe the change in the scaling.

Transverse MSD with respect to the center of mass evolves linearly with time for complete mixing case, and slower than linear with time (slope of $0.8 \sim 1$) for streamline routing case. Different from longitudinal direction, transverse MSD has noticeable difference between complete mixing and streamline routing cases. Complete mixing rule has significantly higher MSD for small heterogeneity and the difference diminishes as heterogeneity increases. Also, note that increase in heterogeneity has clear impact for streamline routing but not for complete mixing case. This is because complete mixing rule itself maximizes transverse spreading so that increase in heterogeneity has no significant impact. For streamline routing, network heterogeneity is the only source of transverse spreading and we can clearly observe transverse spreading increases as heterogeneity increases.

The impact of mixing rule is also clearly shown with probability distribution of transverse particle positions when particles exit a control plane at a fixed distance x from the inlet [Fig. 3-7]. For small conductivity variance, change in mixing has major impact of transverse spreading. However, as conductivity variance increases, the difference between the two mixing rules reduces. First passage time (FPT) distributions for different conductivity heterogeneity and mixing rules at nodes are shown in Fig. 3-8. Conductivity heterogeneity has clear impact on FPT, but the mixing rules has negligible impact of FPT. In summary, conductivity heterogeneity has major impact on longitudinal spreading and mixing rule has major impact on transverse spreading.

To develop a transport model for the observed average particle density $P(\mathbf{x}, t)$, we study average particle movements from a CTRW point of view. This could be done, for example, by interpreting first-passage time distributions in the CTRW framework and inferring an optimal distribution of transition times [9]. Here we follow a different rationale and analyze the ensemble statistics of the Lagrangian velocities because the CTRW model is based on the assumption that particle velocities sampled at given spatial positions along an average trajectory form a Markov process.

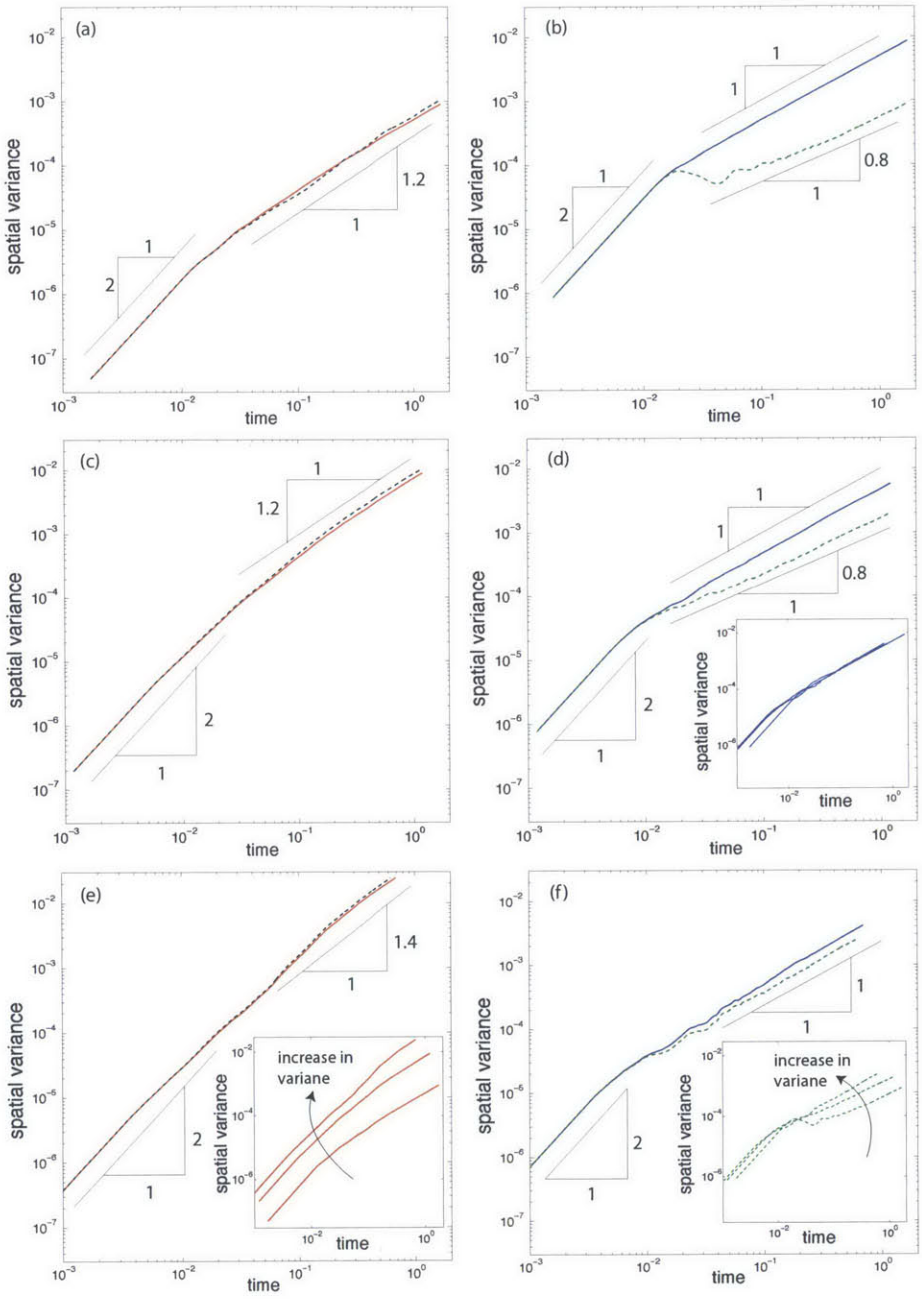

Figure 3-6: Time evolution of second spatial moments for complete mixing (solid line) and streamline routing (dashed line). (a) Longitudinal spreading with conductivity variance 0.1. (b) Transverse spreading with conductivity variance 0.1. (c) Longitudinal spreading with conductivity variance 1. (d) Transverse spreading with conductivity variance 1. inset: Change in the time evolution of transverse spreading for complete mixing with increasing variance. (e) Longitudinal spreading with conductivity variance 5. inset: Change in the time evolution of longitudinal spreading for complete mixing with increasing variance. (f) Transverse spreading with conductivity variance 5. inset: Change in the time evolution of transverse spreading for streamline routing with increasing variance.

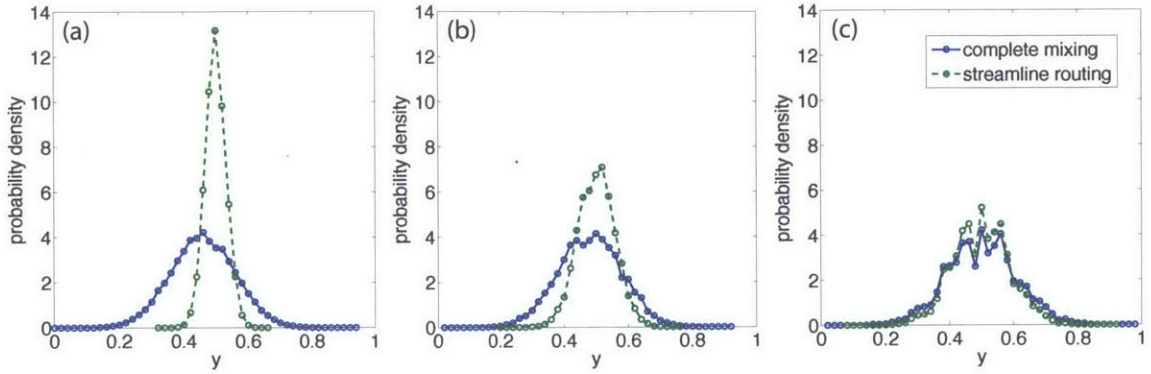

Figure 3-7: Probability density of particle breakthrough position in transverse direction. (a) Comparison between the two different mixing rules for conductivity variance 0.1. (b) Comparison between the two different mixing rules for conductivity variance 1. (c) Comparison between the two different mixing rules for conductivity variance 5.

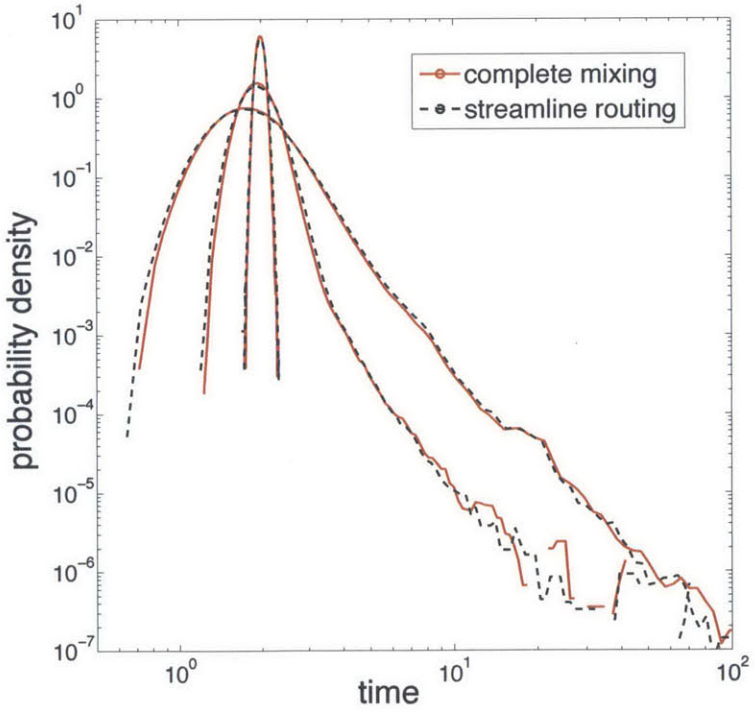

Figure 3-8: Particle first passage time distributions for three different conductivity heterogeneities and different mixing rules.

3.4 Spatial Markov Property.

To characterize average particle movement from a CTRW point of view, we study the ensemble statistics of the series of Lagrangian velocities experienced by particles along individual trajectories. We consider the transition probability density to encounter a velocity v after $n+m$ steps given that the particle velocity was v$'$ after n steps, which in the variables (ν, θ) reads

$$r_m(\nu, \theta|\nu', \theta') = \left\langle \delta\left[\nu - \nu(\mathbf{x}_{n+m})\right] \delta_{\theta,\theta(\mathbf{x}_{n+m})} \right\rangle \Big|_{\nu(\mathbf{x}_n)=\nu', \theta(\mathbf{x}_n)=\theta'} . \tag{3.4}$$

To evaluate the transition probability numerically, the particle velocity ν is discretized into classes, $\nu \in \bigcup_{j=1}^{N}(\nu_j, \nu_{j+1})$ with $N = 50$. The discretization can be either equiprobable or logarithmic scale. The logarithmic scale has better discretization for low velocities which has major role on anomalous transport. We define the transition probability matrix

$$T_m(i, \theta|j, \theta') = \int_{\nu_i}^{\nu_{i+1}} d\nu \int_{\nu_j}^{\nu_{j+1}} d\nu' r_m(\nu, \theta|\nu', \theta') p(\nu', \theta') \Big/ \int_{\nu_j}^{\nu_{j+1}} d\nu' p(\nu', \theta'). \tag{3.5}$$

In $2D$ lattice networks, there are sixteen possible transitions which are described by multi-dimensional transition matrix [Fig. 3-8]. The transition matrices can be obtained numerically from ensemble of particle trajectories. The transition matrices for two different heterogeneity distributions and mixing rules are shown in Fig. 3-10, 3-11, 3-12, 3-13, 3-14, 3-15, 3-16, and 3-17. For small heterogeneity, the difference in the transition matrix between complete mixing rule and streamline routing rule is clear. This difference diminishes as heterogeneity increases. The impact of heterogeneity on particle transition matrix is significant. As heterogeneity increases, the probability of transitions with backward transition increases.

The aggregate transition matrix $T_m(i|j) = \sum_{\theta,\theta'} T_m(i, \theta|j, \theta')$ shown in Fig. 3-18a for $m = 1$, clearly indicates that particle velocities are correlated (5 velocity classes are assigned to negative velocities and 95 velocity classes are assigned to positive velocities.). The relatively large probabilities in the upper-left and lower-right corners of the transition

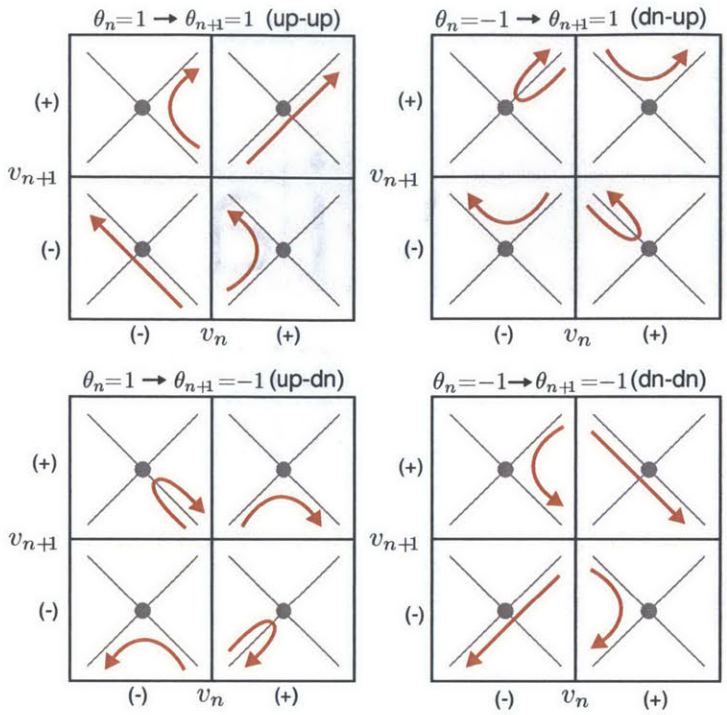

Figure 3-9: Illustration of velocity transition matrix for $2D$ lattice networks. Transition matrix considers all 16 possible transitions to capture the full particle transport dynamics.

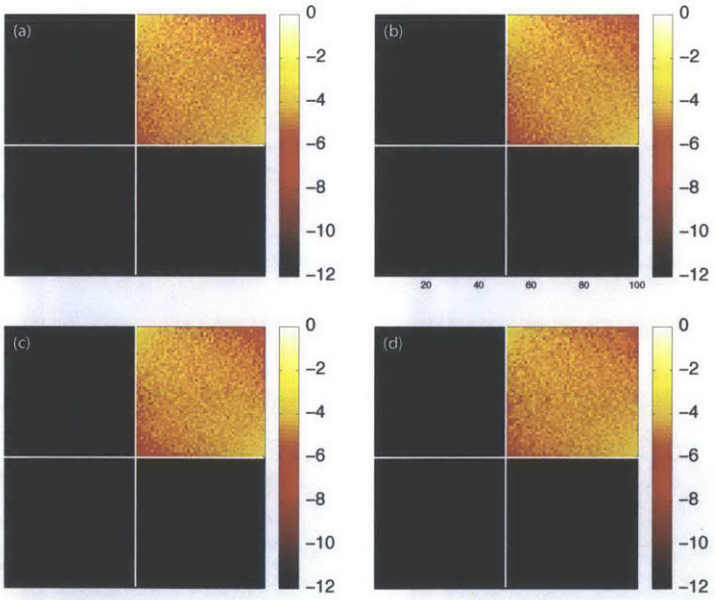

Figure 3-10: Velocity transition matrix with equiprobable binning for $\sigma^2_{\ln k} = 0.1$ and complete mixing rule. Only four transitions that have forward movement in longitudinal direction are possible out of sixteen possible transitions. Also, note that the probability for each possible transition is almost identical.

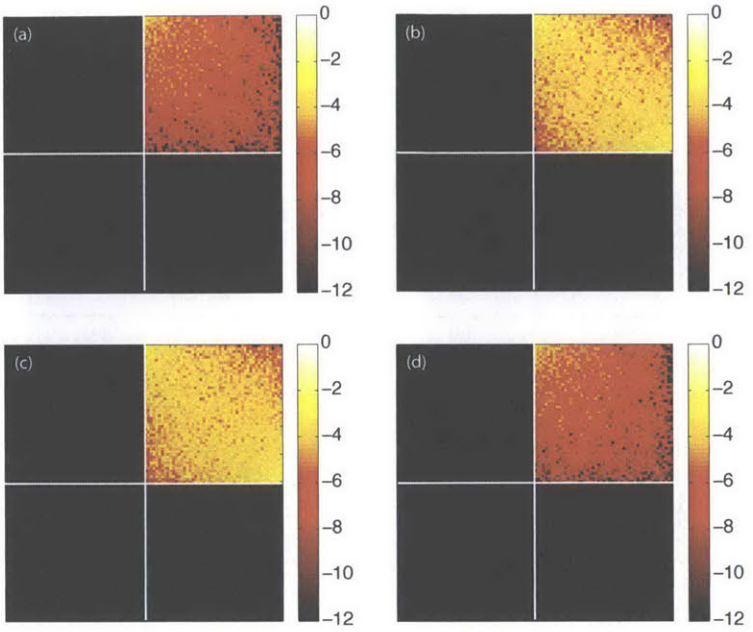

Figure 3-11: Velocity transition matrix with equiprobable binning for $\sigma^2_{\ln k} = 0.1$ and streamline routing rule. Only four transitions that have forward movement in longitudinal direction are possible out of sixteen possible transitions. Also, note that the probability for up-down and down-up forward transitions have significantly higher probabilities compared to up-up and down-down forward transitions.

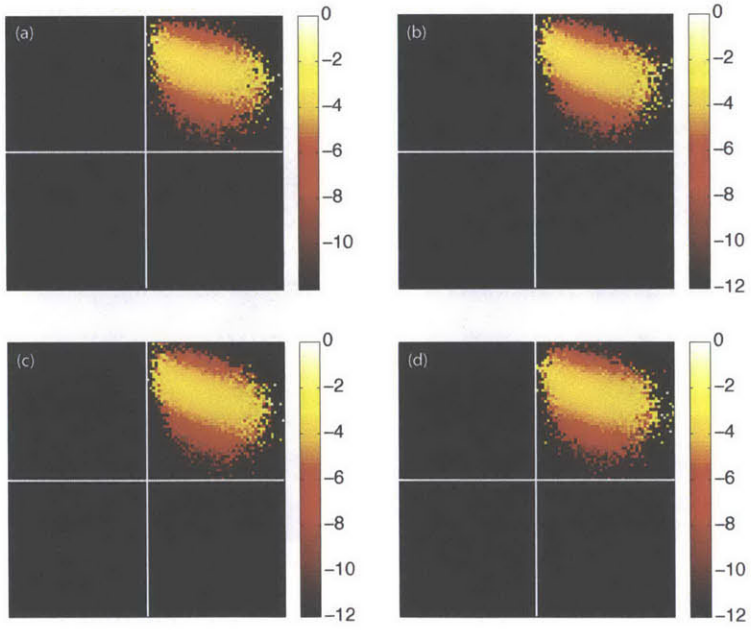

Figure 3-12: Velocity transition matrix with log-scale binning for $\sigma^2_{\ln k} = 0.1$ and complete mixing rule.

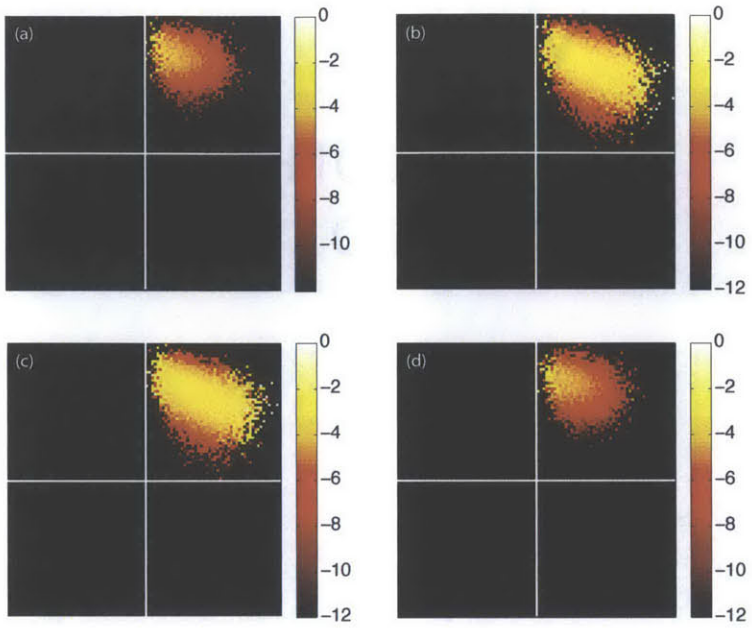

Figure 3-13: Velocity transition matrix with log-scale binning for $\sigma^2_{\ln k} = 0.1$ and streamline routing rule.

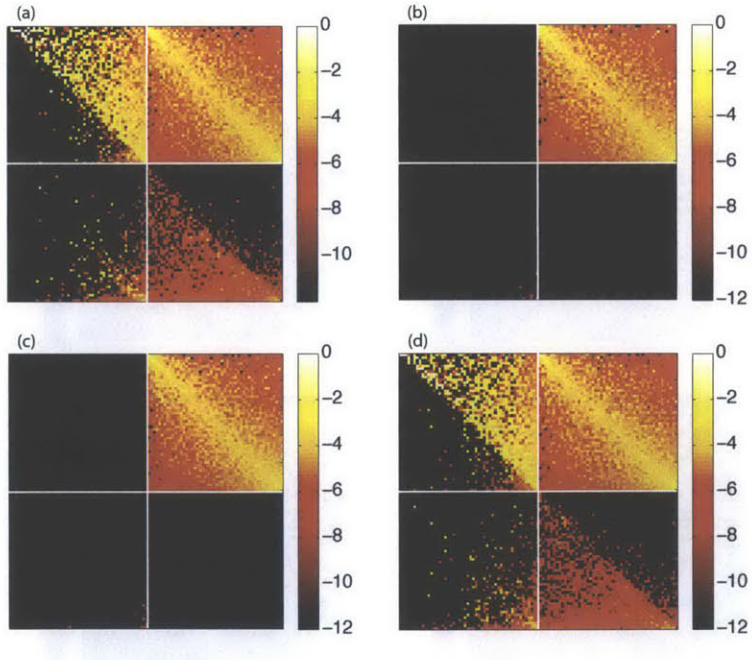

Figure 3-14: Velocity transition matrix with equiprobable binning for $\sigma^2_{\ln k} = 5$ and complete mixing rule. Due to strong heterogeneity, 12 out of 16 possible transitions are happening. Also, note that up-up and down-down transitions have triangular matrices.

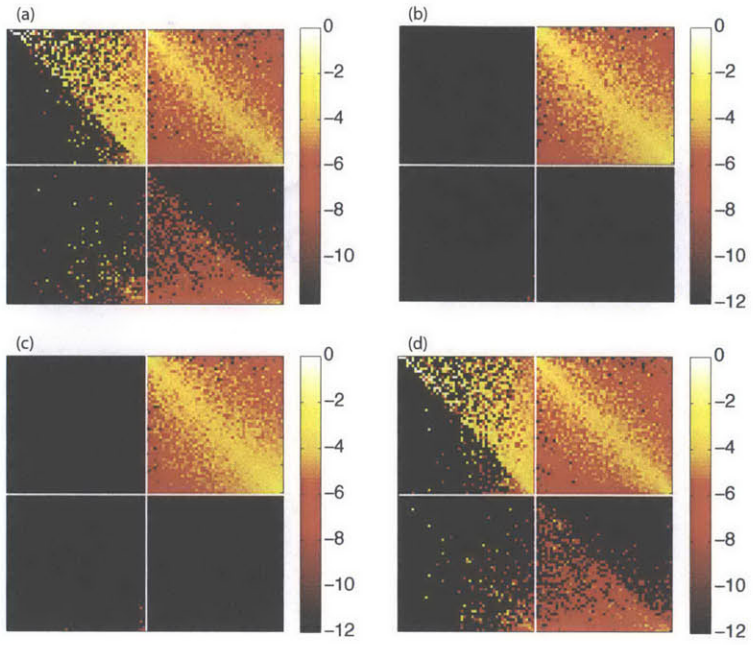

Figure 3-15: Velocity transition matrix with equiprobable binning for $\sigma^2_{\ln k} = 5$ and streamline routing rule. Since strong heterogeneity determines the particle transition, there is no noticeable difference between complete mixing and streamline routing.

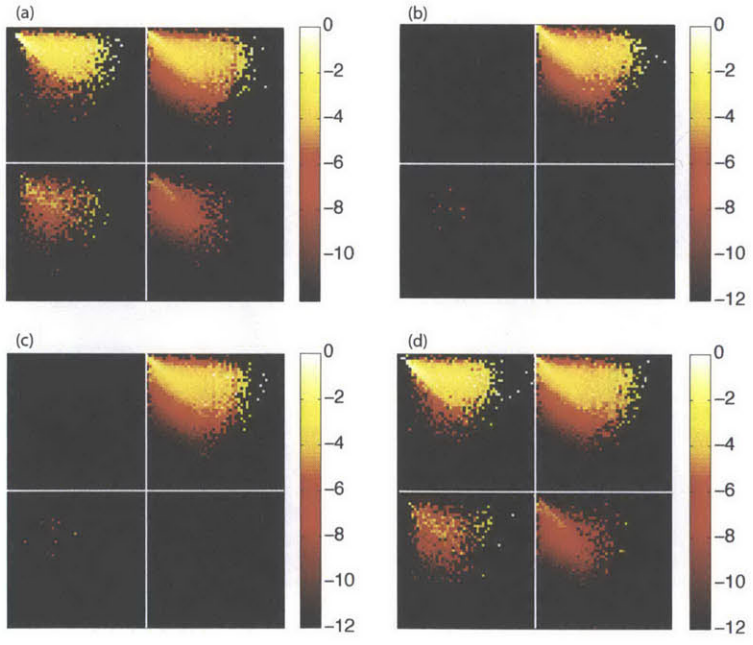

Figure 3-16: Velocity transition matrix with log-scale binning for $\sigma^2_{\ln k} = 5$ and complete mixing rule.

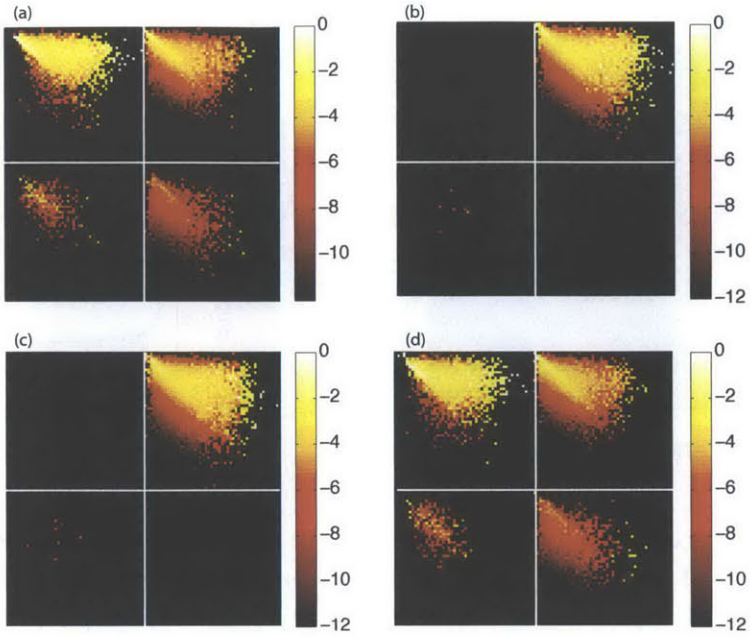

Figure 3-17: Velocity transition matrix with log-scale binning for $\sigma^2_{\ln k} = 5$ and streamline routing rule.

matrix reflect flow reversal.

The series of Lagrangian velocities $\mathbf{v}(\mathbf{x}_n) \equiv \mathbf{v}_n$ along particle trajectories can be approximated as a Markov process, if the transition matrix satisfies the Chapman-Kolmogorov equation [e.g., 125], which in matrix form reads

$$T_n(i, \theta | j, \theta') = \sum_{i', \theta''} T_{n-m}(i, \theta | i', \theta'') T_m(i', \theta'' | j, \theta'). \tag{3.6}$$

Specifically, for a Markov process, the m-step transition matrix $\mathbf{T}_m$ is equal to the m-fold product of the 1-step transition matrix $\mathbf{T}_1$ with itself as $\mathbf{T}_m = \mathbf{T}^m$. Figure 3-18c shows the transition probabilities for $m = 5$ steps conditional to a low ($j = 5$) and high ($j = 90$) velocity class given by $\mathbf{T}_5$, which is obtained by direct Monte Carlo simulations, and under the Markov assumption from $\mathbf{T}^5$. The Markov model predicts accurately the transition probabilities, as well as the return probability for any number of steps [Fig. 3-18b, inset]. Our analysis suggests that the Markov model captures the Lagrangian velocity statistics accurately. We repeated the analysis for truncated power-law and the absolute value of Cauchy distributions of conductivity, and found that the Markovianity assumption holds

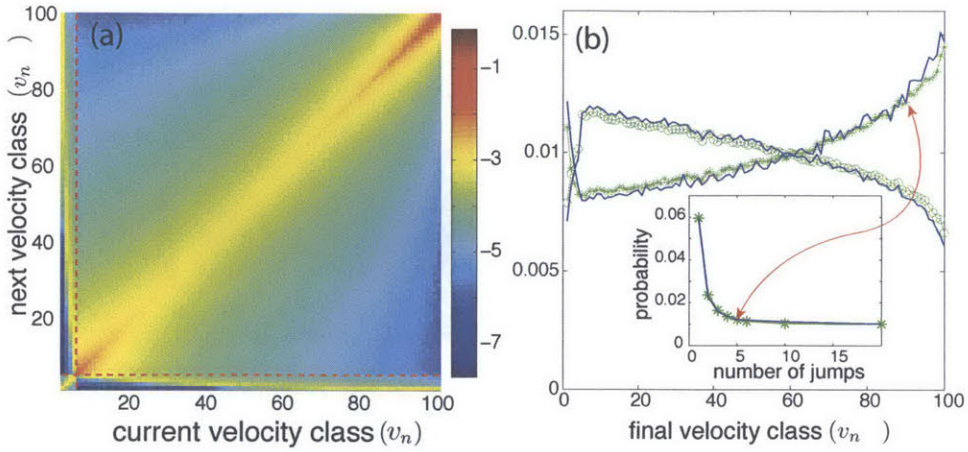

Figure 3-18: (a) Aggregate transition matrix for $N = 100$ velocity classes distributed with logarithmic scale. (b) Transition probabilities after $m = 5$ steps from direct Monte Carlo computation (blue solid line) and calculated from the Markov assumption (green symbols). Shown are probability densities for two initial velocity classes: a low velocity class ($j = 5$, $\circ$), and a high velocity class ($j = 90$, $*$). Inset: probability of returning to the same initial velocity class as a function of the number of steps for a high initial velocity (class $j = 90$).

for these conductivity distributions too. Therefore, a CTRW characterized by a one step correlation in velocity is a good approximation for describing average transport.

3.5 Continuous Time Random Walk Model.

Particle movements in the random lattice can, on average, be described by the following system of Langevin equations

$$\mathbf{x}_{n+1} = \mathbf{x}_n + l\frac{\mathbf{v}_n}{|\mathbf{v}_n|}, \qquad t_{n+1} = t_n + \frac{l}{|\mathbf{v}_n|}. \tag{3.7}$$

We have already shown that the series of Lagrangian velocities $\{\mathbf{v}_n\}_{n=0}^{\infty}$ is well approximated by a Markov process and thus fully characterized by the one-point density $p(\mathbf{v}) = \langle\delta(\mathbf{v} - \mathbf{v}_n)\rangle$ and the one-step transition probability density

$$r_1(\mathbf{v}|\mathbf{v}') = \langle\delta(\mathbf{v} - \mathbf{v}_{n+1})\rangle|_{\mathbf{v}_n=\mathbf{v}'}. \tag{3.8}$$

The particle density can be written as

$$P(\mathbf{x},t) = \int d\mathbf{v} \langle \delta(\mathbf{x} - \mathbf{x}_{n_t}) \delta(\mathbf{v} - \mathbf{v}_{n_t}) \rangle, \tag{3.9}$$

in which $n_t = \max(n | t_n \leq t)$, $\mathbf{x}$ is the position of the node at which the particle is at time t, and $\mathbf{v}$ is the velocity by which the particle emanates from this node. Equation (3.9) can be recast as

$$P(\mathbf{x},t) = \int d\mathbf{v} \int_{t-l/|\mathbf{v}|}^{t} dt' R(\mathbf{x},\mathbf{v},t'), \tag{3.10a}$$

in which we defined

$$R(\mathbf{x},\mathbf{v},t') = \sum_{n=0}^{\infty} \langle \delta(\mathbf{x} - \mathbf{x}_n) \delta(\mathbf{v} - \mathbf{v}_n) \delta(t' - t_n) \rangle. \tag{3.10b}$$

The latter satisfies the Kolmogorov type equation

$$\begin{aligned} R(\mathbf{x},\mathbf{v},t) &= \delta(\mathbf{x}) p(\mathbf{v}) \delta(t) + \int d\mathbf{v}' r_1(\mathbf{v}|\mathbf{v}') \\ &\times \int d\mathbf{x}' \delta(\mathbf{x} - \mathbf{x}' - l\mathbf{v}'/|\mathbf{v}'|) R(\mathbf{x}',\mathbf{v}',t - l/|\mathbf{v}'|). \end{aligned} \tag{3.10c}$$

For independent successive velocities, i.e., $r_1(\mathbf{v}|\mathbf{v}') = p(\mathbf{v})$, one recovers the CTRW model [e.g., 129]

$$P(\mathbf{x},t) = \int_0^t dt' R(\mathbf{x},t') \int_{t-t'}^{\infty} d\tau \int d\mathbf{x} \psi(\mathbf{x},\tau), \tag{3.11a}$$

where $R(\mathbf{x},t)$ satisfies

$$\begin{aligned} R(\mathbf{x},t) &= \delta(\mathbf{x}) \delta(t) \\ &+ \int d\mathbf{x}' \int_0^t dt' R(\mathbf{x}',t') \psi(\mathbf{x} - \mathbf{x}', t - t') \end{aligned} \tag{3.11b}$$

and the joint transition length and time density is given by

$$\psi(\mathbf{x}, t) = \int d\mathbf{v}' p(\mathbf{v}') \delta(\mathbf{x} - l\mathbf{v}'/|\mathbf{v}'|) \delta(t - l/|\mathbf{v}'|). \tag{3.11c}$$

In the following, we refer to system (3.10) as *correlated* CTRW because subsequent particle velocities are correlated, and to model (3.11) as *uncorrelated* CTRW because subsequent particle velocities are uncorrelated.

3.6 Model Prediction

Based on the identified Markovianity of particle transitions, the developed correlated CTRW model is applied to study the predictability of the model. The predictions of the developed correlated CTRW model shows excellent match with the Monte Carlo simulations for three different heterogeneity and the different mixing rules that we studied [Fig. 3-19, 3-20, 3-21].

To confirm long-time predictability of the developed model, we study the lattice size of 500×500 nodes and, in each realization, we release 10^3 particles at the origin in 10^3 realizations. The following results are for variance $\sigma^2_{\ln k} = 5$. We compare the results obtained from direct Monte Carlo simulations to correlated CTRW and uncorrelated CTRW. Correlated CTRW is parametrized by the one-step transition matrix $\mathbf{T}_1$ determined from numerical Monte Carlo simulations. Uncorrelated CTRW is parametrized by the Lagrangian velocity distribution $p(\mathbf{v})$, which is obtained from Monte Carlo simulations as well.

The particle distribution is non-Gaussian and characterized by a sharp leading edge and an elongated tail [Fig. 3-22]. The non-Gaussian features persist even after the center of mass has travelled a distance of about 100 links in the direction of the mean flow. Correlated CTRW captures the shape of the particle plume with remarkable accuracy, including its leading edge, peak, transverse spread, and low-probability tail near the origin. Ignoring the correlated structure of the Lagrangian velocity leads to predictions of longitudinal and transverse spreading that deviate from the direct Monte Carlo simulation [Fig. 3-22, insets].

Figure 3-23a shows the time evolution of the longitudinal and transverse spreading.

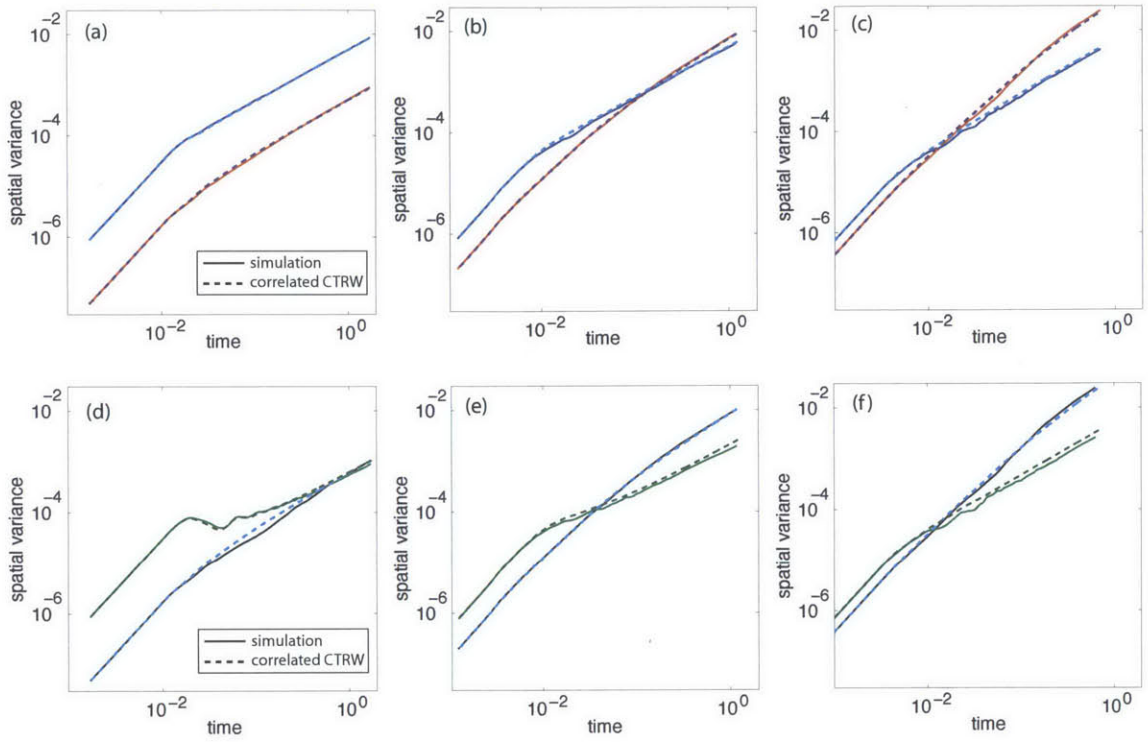

Figure 3-19: Comparison between time evolution of MSDs for Monte Carlo simulations and model predictions. The developed correlated CTRW model is able to accurately capture time evolution of MSDs for all of the conductivity heterogeneities and mixing rules. (a) $\sigma^2_{\ln k} = 0.1$ and complete mixing rule. (b) $\sigma^2_{\ln k} = 1$ and complete mixing rule. (c) $\sigma^2_{\ln k} = 5$ and complete mixing rule. (d) $\sigma^2_{\ln k} = 0.1$ and streamline routing rule. (e) $\sigma^2_{\ln k} = 1$ and streamline routing rule. (f) $\sigma^2_{\ln k} = 5$ and streamline routing rule.

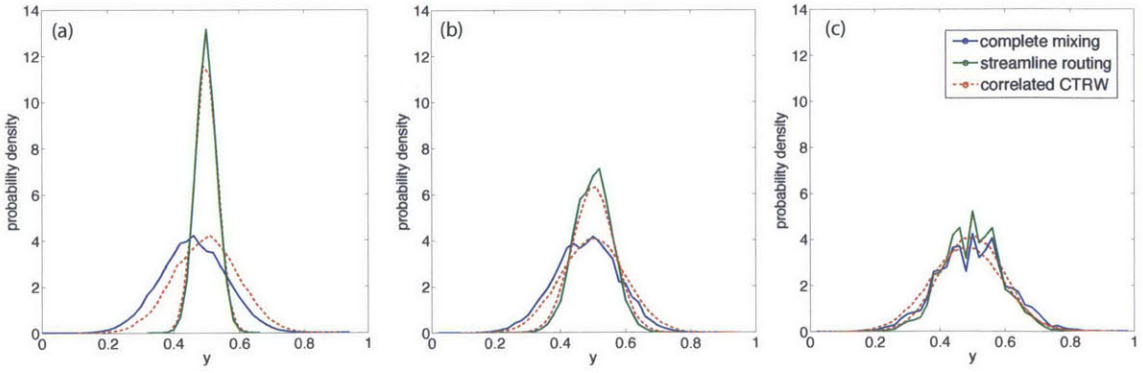

Figure 3-20: Probability distributions of transverse particle breakthrough position for Monte Carlo simulations and model predictions. (a) $\sigma^2_{\ln k} = 0.1$. (b) $\sigma^2_{\ln k} = 1$. (c) $\sigma^2_{\ln k} = 5$.

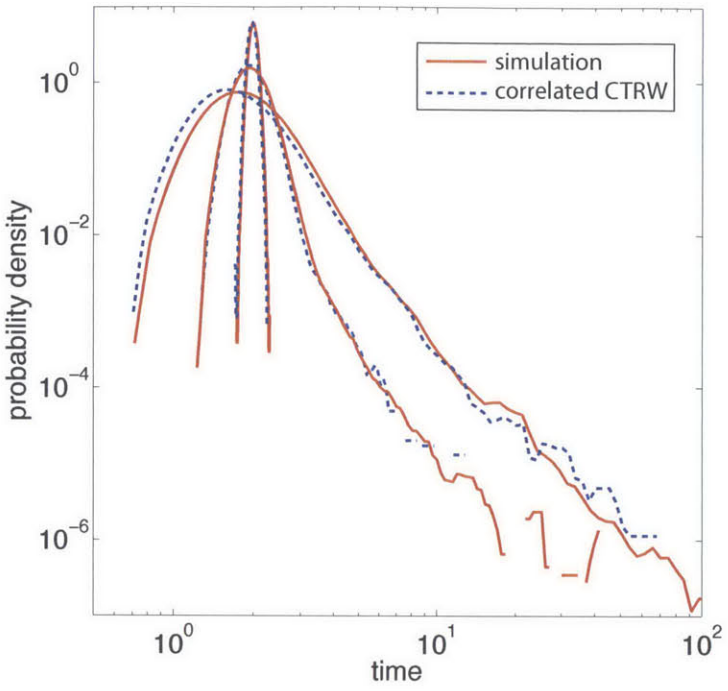

Figure 3-21: Comparison of FPT distributions of Monte Carlo simulations and model predictions.

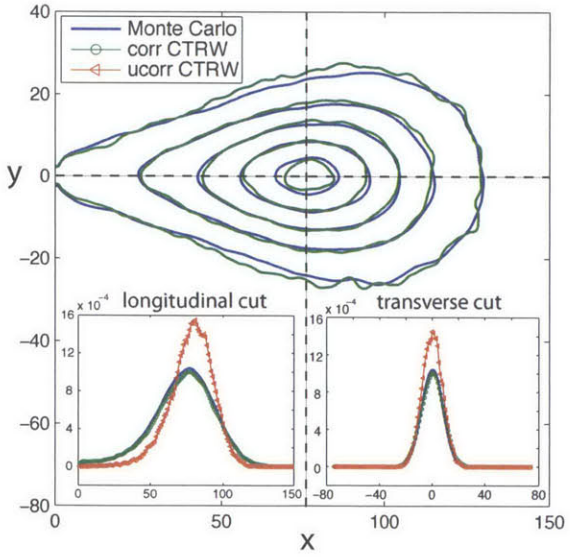

Figure 3-22: Contour plot of the mean particle density at $t = 5 \times 10^2$, computed from direct Monte Carlo simulation (blue solid line), correlated CTRW model (green solid line), and uncorrelated CTRW model (red solid line).

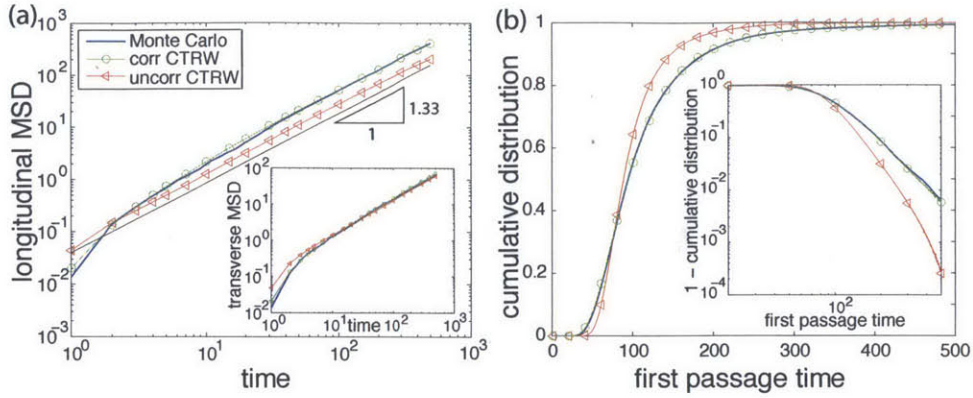

Figure 3-23: (a) Time evolution of the longitudinal MSD. Inset: Transverse MSD. (b) Cumulative FPT distribution.

The Monte Carlo simulation shows that the longitudinal mean square displacement (MSD) with respect to the center of mass evolves faster than linear with time (slope of 1.33). Both the scaling and the magnitude of the longitudinal spreading are captured accurately by correlated CTRW. The model also reproduces accurately the magnitude and time scaling of the transverse MSD. The uncorrelated model underpredicts the magnitude of longitudinal spreading.

Nonlocal theories of transport, including CTRW, are often invoked to explain the empirical observation that the first passage time (FPT) distribution is broad-ranged [10]. Early arrival and slow decay of the FPT is also observed in our model system, even when the conductivity distribution is lognormal and has zero spatial correlation [Fig. 3-23(b)]. The cumulative FPT distribution from the Monte Carlo simulation exhibits a significantly slower decay than uncorrelated CTRW. This behavior is accurately captured by correlated CTRW, suggesting that the velocity correlation along particle trajectories is responsible for the emergence of the observed asymptotic behavior.

3.7 CTRW model with effective parameterization

The proposed model utilizes Markov property of velocity transitions and takes one-point density $p(\mathbf{v})$ and the one-step transition probability density $r_1(\mathbf{v}|\mathbf{v}')$ as two inputs. Some might argue that the model has to many parameters since the transition matrix (T_1) has

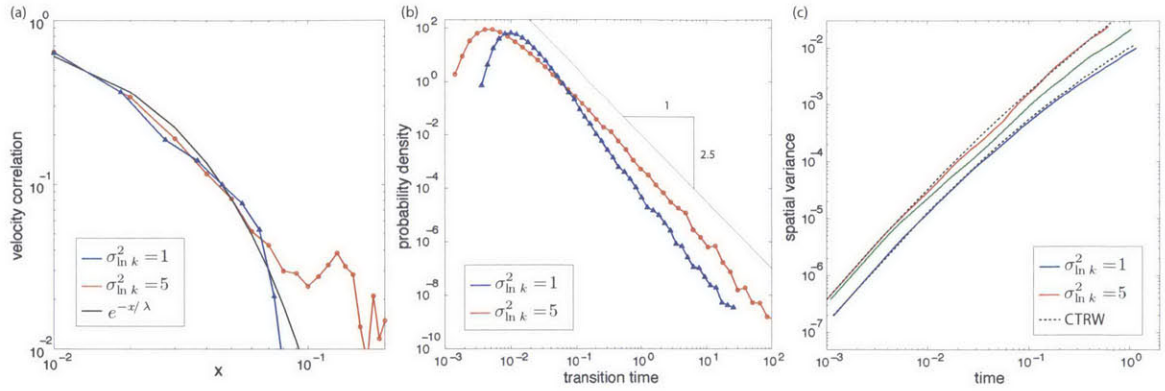

Figure 3-24: (a) Velocity autocorrelation function for $\sigma^2_{\ln k} = 1$ and $\sigma^2_{\ln k} = 5$. For both cases, we can accurately fit exponential correlation function with $\lambda = 3l$. (b) Probability distribution functions of transition time in longitudinal direction. (c) Comparison between the MSD from MC simulations and CTRW model. Our effectively parameterized CTRW can accurately predict the time evolution of MSDs. Without correlation, we underestimate MSD (green line).

N by N values where N is the number of velocity bins. However, the core information we need from $r_1(\mathbf{v}|\mathbf{v}')$ is the strength of the velocity correlation and it can be effectively parameterized with single value. The full description of the simplified model can be found in 4.4.3. To validate CTRW model with effective parameterization, we parametrized the model with measured correlation length and the velocity probability distribution function (Fig. 3-24(a)(b)). For both $\sigma^2_{\ln k} = 1$ and $\sigma^2_{\ln k} = 5$ conductivity fields, we can obtain correlation length λ in the order of $3l$ where l is the link length. The modeling result is shown in Fig. 3-24(c) that shows accurate predictability for both $\sigma^2_{\ln k} = 1$ and $\sigma^2_{\ln k} = 5$ conductivity fields. The detailed structure of velocity transition matrix might be important in different settings, however, the proposed effective parameterization shows excellent predictability for lattice networks.

3.8 Discussion

We have shown that the divergence-free condition arising from mass conservation is the source of strong and nontrivial correlation in the Lagrangian velocity, even when the underlying conductivity field is completely uncorrelated. Accounting for such correlation in the velocity is important to obtain quantitative agreement for the mean particle density

and the FPT distribution. Here, we have proposed and validated a spatial Markov model of transport on a lattice network that explicitly captures the multidimensional effects associated with changes in direction along the particle trajectory. Finally, we suspect that correlation in the Lagrangian velocity exerts an even more dominant control over mixing (understood as the decay of the variance of the particle density [91, 73, 140]) than it does on spreading. We now further extend our findings to field-scale anomalous transport.

Chapter 4

Field experiment on fractured granite

4.1 Background

Understanding flow and transport through fractured geologic media is essential for improving forecasts, management and risk assessment of many subsurface technologies, including geologic nuclear waste disposal [17], geologic CO_2 storage [137]; oil and gas production from fractured reservoirs [84], enhanced geothermal systems [118], shale-gas development [31, 30], and groundwater contamination and remediation [58, 69]. Moreover, if we conceptualize fractured geologic media as a network system, this knowledge can be extended to other physical processes, including disease spreading through river networks [124] and the air transportation system [112], urban traffic [85], and nutrient transport through preferential paths in biofilms [150].

There are two main sources of uncertainty for transport through fractured media: uncertainty in the fracture structural properties, including fracture aperture, roughness, location and connectivity describing fracture geometry; and uncertainty in the physical transport processes impacting the flow and transport such as advection, diffusion, dispersion and adsorption. The fracture structural properties and the physical transport processes are interdependent, and may lead to anomalous transport. Anomalous transport, understood as the nonlinear scaling with time of the mean square displacement of transported particles, is a characteristic feature of transport through porous and fractured geologic media [10, 12, 8].

The uncertainty in fracture structural properties affects transport in two major ways.

First, heterogeneity in fracture conductivities gives rise to slow and fast velocity zones, which result in a broad range of particle transport velocities. As fracture heterogeneity increases, the velocity distribution also becomes more heterogeneous, thereby impacting the macroscopic transport. Second, the network of interconnected rock fractures form complex hydrodynamic pathways that impact the flow correlation structure. Fracture length impacts velocity correlation since the velocity within each fracture is highly correlated. Therefore, the fracture structural properties impact both the transport velocity distribution and flow correlation. In practice, however, the fracture structural information is very limited and only a few dominant properties, such as relative fracture aperture and dominant major fractures, are identifiable [46].

Heterogeneous advection, matrix diffusion, hydrodynamic dispersion and adsorption are the four key physical transport mechanisms that impact transport of nonreactive tracers through fractured media. Heterogeneous advection, which results from the separation of mass into different flow channels, can be partially reversible when the flow field is reversed. Matrix diffusion is an irreversible process that describes mass exchange between fractures and the surrounding rock matrix. Hydrodynamic dispersion is a local mixing phenomenon within the fracture that always increases in the direction of flow. Adsorption is the adhesion of dissolved tracers to solid surfaces. For nonreactive tracers, all these physical phenomena can be understood as either an advective or a diffusive process. Heterogeneous advection is an advective process, and matrix diffusion, hydrodynamic dispersion, and adsorption can be understood as diffusive processes. The interplay between advective and diffusive processes determines the strength of flow correlation. An advective process tends to maintain the velocity, whereas a diffusive process tends to erode the velocity correlation. The competition between advective and diffusive processes is therefore manifested by the reversibility of flow. Advection is a reversible process: when flow is reversed, the spreading caused by heterogeneous advection collapses back. In contrast, diffusion is an irreversible process: particle spreading cannot be collapsed by reversing the flow. The physical transport mechanisms also impact the Lagrangian velocity distribution. For example, heterogeneous advection induces a broad velocity distribution via the combination of slow paths and fast paths, matrix diffusion via the trapping of tracers in the rock matrix, and adsorption via the

adhesion of particles onto the rock surface.

In summary, the complex interplay between fracture structural properties and physical transport processes determine the average particle transport behavior via flow correlation and flow heterogeneity. Recent studies have shown that tracer transport through fractured and porous media is strongly modulated by the particle velocity distribution and velocity correlation [90, 78, 35, 80]. Here, we develop a stochastic model of transport that recognizes the impact of both flow heterogeneity and flow correlation as an integral part of its ability to make predictions of transport at the field scale.

4.2 Field experiments

A signature of anomalous transport in the field is the late-time tailing of breakthrough curves (BTCs), that is, time series of tracer concentration at the pumping well. Breakthrough curves are affected by both the underlying fracture structural properties and the physical transport processes such as advection, diffusion, dispersion and adsorption. Thus, they are sensitive to both flow heterogeneity and flow correlation.

We build on the seminal observation by [144], who suggested that the combination of different tracer tests could be used to reduce the uncertainty in the characterization of fractured media. Here, we propose a framework to combine single-well (push-pull) and two-well (convergent) tests to extract transport parameters.

4.2.1 Field site and tracer-test setup

We conducted a series of field tracer tests under forced hydraulic gradient in a saturated fractured granite formation close to Ploemeur, France [46] (Figure 4-1). Geologically, the site is located at the contact between the underlying fractured granite and the overlying mica schist. The matrix permeability of granite is extremely low and, therefore, groundwater flows mainly through the network of fractures.

For this study, we used two boreholes, B1 (83 m deep) and B2 (100 m deep), which are 6 m apart. Previous work [46, 47] has identified four major conductive fractures intersecting B1, labelled B1-1 (24 m deep), B1-2 (50 m), B1-3 (63 m) and B1-4 (79 m), and

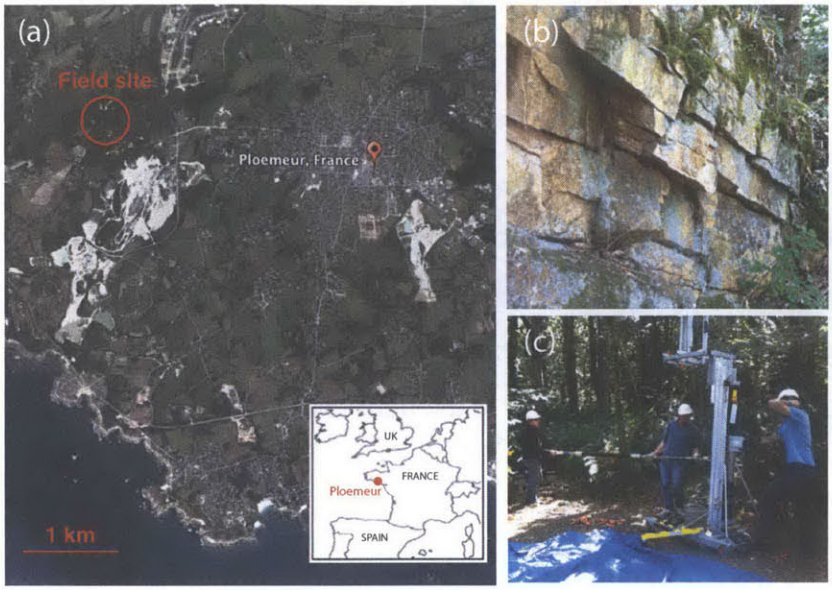

Figure 4-1: (a) Satellite image of the Ploemeur field site (modified from Google Earth). Inset: map showing the location of Ploemeur, France. (b) Outcrop of fractured granite at the Ploemeur field site. (c) Photo from the installation of double packer system in B1 borehole.

four major conductive fractures intersecting B2, labelled B2-2 (56 m), B2-3 (59 m), B2-4 (79 m) and B2-5 (97 m). We designed and conducted convergent and push-pull tests at two different fractures: B1-2 and B1-4. Regional flow is negligible compared to the flow from injection and withdrawal at the boreholes, as confirmed by tracer dilution tests conducted at B1-2 and B1-4 under regional flow conditions. As a tracer, we used fluorescein, which is widely used for groundwater tracing and known to be non-reactive, insensitive to pH and salinity, and moderately resistant to adsorption and photochemical bleaching [136].

Convergent tracer test

In the convergent test, we inject a known mass of tracer into an injection borehole (B1) and measure the tracer concentration at the pumping borehole (B2) (Fig. 4-2(a,b,c)). To place the tracer at the target fracture, we installed a double-packer at the injection borehole at two different depths, targeting the B1-2 and B1-4 fractures in separate experiments. To form a stationary, radial convergent flow configuration, a constant pumping rate was established at borehole B2 throughout the experiment. Once a stationary pressure field is achieved, we inject the tracer at borehole B1 for a short duration compared to the total duration of

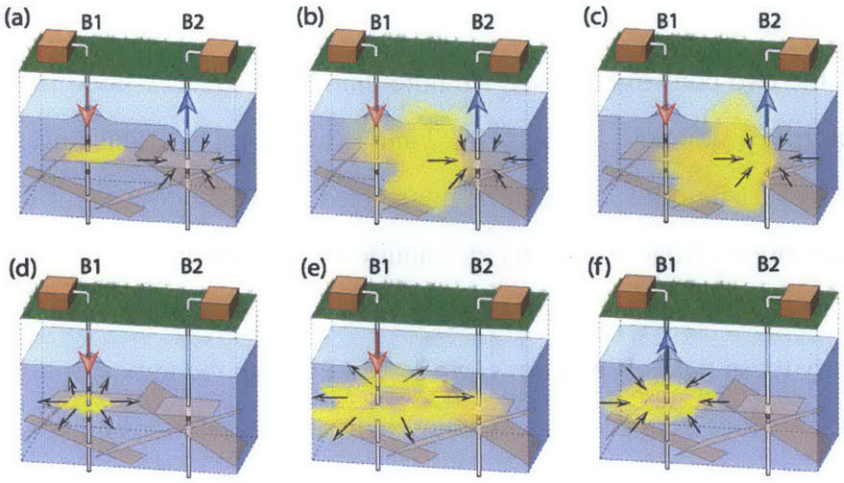

Figure 4-2: Schematic of the tracer tests conducted. (a,b,c) Convergent test with tracer placement at borehole B1 and pumping from borehole B2. Two different fracture planes at different depths (B1-2 and B1-4) are used for two separate tests. (d,e,f) Push-pull test from borehole B1. The same two fracture planes (B1-2 and B1-4) are used.

the experiment, and at a small injection rate (<1% of the pumping rate at B2). When the injection of tracer is completed, we recirculate the fluid inside the double-packer system to prevent the tracer from continuing to leak into the formation.

Push-pull tracer test

In the push-pull test, we first inject a known mass of tracer into borehole B1, and continue to inject fresh water for a fixed duration of time ("push" phase). We then reverse the flow and pump water from the same borehole with the same flow rate ("pull" phase), and measure the arrival tracer concentration (Fig. 4-2(d,e,f)). Again, a double-packer system was installed to isolate the injection into the desired fracture plane.

4.2.2 Field test results

Additional details on the conditions and parameters of the field experiments are given in Table 4.1, and the measured BTCs are shown in Figure 4-3. As expected, the BTCs are broader for the convergent tests than for the push-pull tests, given that in the latter the spreading during the "push" phase is partially recovered during the "pull" phase. Indeed, the degree to which the initial tracer spreading is reversed is an indication of the strength

of velocity correlation.

Analyzing the two convergent tests, we note that the power-law late-time scalings are different, exhibiting a slope of $\sim$1.75 for B1-2 and $\sim$1.85 for B1-4. This difference reflects different velocity distributions, and can be interpreted as different levels of heterogeneity, with the gentler slope (broader velocity distributions) corresponding to a higher level of heterogeneity.

Motivated by these field observations, we review existing theoretical transport models, and develop a new model that takes into account both flow correlation and flow heterogeneity.

Table 4.1: Details of the conditions and parameters of the four tracer experiments.

Experimental parameters	Experiments			
	B1-2 convergent	B1-2 push-pull	B1-4 convergent	B1-4 push-pull
Tracer injection fracture	B1-2	B1-2	B1-4	B1-4
Withdrawal borehole / fracture	B2	B1-2	B2	B1-4
Flow configuration	convergent	push-pull	convergent	push-pull
Tracer injection depth	50.5 m	50.5 m	78.7 m	78.7 m
Packer system at B1	double packer	double packer	double packer	double packer
Packer system at B2	single packer	single packer	single packer	single packer
Injection rate	1 L/min	6 L/min	1 L/min	5 L/min
Injection duration	15 min	30 min	15 min	80 min
Withdrawal rate	120 L/min	6 L/min	100 L/min	5 L/min
Injected mass	5 g	0.1 g	1.5 g	0.4 g
Peak arrival time	30 min	57 min	35 min	140 min
Peak concentration	590 ppb	353 ppb	312 ppb	690 ppb
Mass recovery	96 %	89 %	99 %	87 %
Late-time tailing slope	$\sim$ 1.7		$\sim$ 1.85	

4.3 Existing models of transport

Various approaches have been proposed to model flow and transport through fractured media, ranging from equivalent porous medium approaches that represent the fractured medium as a single continuum [110, 145], to discrete fracture networks that explicitly represent fractures as entities embedded in the surrounding matrix [86, 24, 107, 75, 105, 82, 99, 104, 100, 37, 132]. Dual porosity models are, in some sense, in between these two

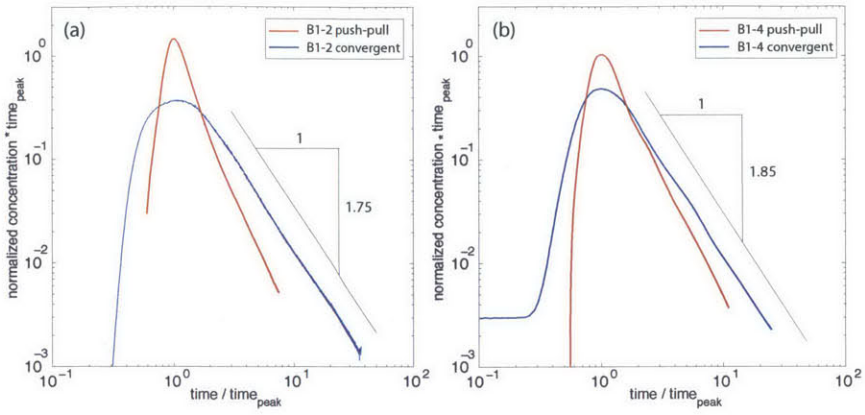

Figure 4-3: Measured breakthrough curves (BTC) for the tracer tests we conducted, in the form of a normalized time (peak arrival at dimensionless time of 1) and normalized concentration (such that the area under the BTC is identically equal to 1). (a) BTCs for fracture plane B1-2. (b) BTCs for fracture plane B1-4.

extremes, and conceptualize the fractured–porous medium as two overlapping continua, which interact via an exchange term [11, 52, 98, 58].

Stochastic models that account for the observed non-Fickian global transport behavior in fractured media include continuous-time random walks (CTRW) [8, 77, 78], fractional advection-dispersion equations (fADE) [7], multirate mass transfer (MRMT) [63, 25, 88], stochastic convective stream tube (SCST) models [4], and Boltzmann equation approaches [5]. All of these models are valid under their own assumptions, and have played an important role in advancing the understanding of transport through fractured media. Among these models, the MRMT and SCST approaches have been applied to model non-Fickian tracer transport in both push-pull and convergent tests [64, 101, 4].

Below, we briefly revisit the basic formulations of the classical advection-dispersion, stochastic-convective streamtube and multirate mass transfer models for radial flow geometries, and discuss their ability to capture BTCs for convergent and push-pull tests.

4.3.1 Advection-dispersion equation (ADE) model

The classical advection-dispersion equation (ADE) in radial coordinates is given by

$$\frac{\partial c(r,t)}{\partial t} + \frac{k_v}{r}\frac{\partial c(r,t)}{\partial r} - \frac{\alpha k_v}{r}\frac{\partial^2 c(r,t)}{\partial r^2} = 0, \tag{4.1}$$

where α is dispersivity and $k_v = Q/(2\pi b_{\text{eff}})$ with Q the flow rate and b_{eff} the effective transport aperture [89]. Since we will use a Lagrangian modeling approach in the following, we formulate the advection-dispersion model in terms of radial particle trajectories. This can be done by rewriting (4.1) in terms of a conserved variable in radial coordinates,

$$p(r,t) = 2\pi b_{\text{eff}} r c(r,t), \tag{4.2}$$

which is the particle density per unit radial length. Inserting the latter into (4.1) we obtain

$$\frac{\partial p(r,t)}{\partial t} + \frac{\partial}{\partial r}\frac{k_v}{r}p(r,t) - \frac{\partial^2}{\partial r^2}\frac{\alpha k_v}{r}p(r,t) = 0. \tag{4.3}$$

The equivalent Langevin equation is given by

$$\frac{dr(t)}{dt} = \frac{k_v}{r(t)} + \sqrt{\frac{2\alpha k_v}{r(t)}}\xi_r(t), \tag{4.4}$$

where $\xi_r(t)$ is a Gaussian white noise of zero mean and unit variance. Here and in the following, we employ the Ito interpretation of the Langevin equation (4.4) [125]. The particle density is given in terms of the radial trajectories as $p(r,t) = \langle \delta[r - r(t)] \rangle$, and by virtue of (4.2), we obtain for the concentration distribution

$$c(r,t) = \frac{1}{2\pi b_{\text{eff}} r}\langle \delta[r - r(t)] \rangle. \tag{4.5}$$

The angular brackets $\langle \cdot \rangle$ denote the average over all solute particles.

The solute breakthrough curve at a distance r_c from the injection point $r(0)$ is given in terms of the probability density function of the particles' first arrival times at the radius $r = r(0) + r_c$,

$$\tau_a = \inf \{t| \ |r(t) - r(0)| \geq r_c\}, \tag{4.6}$$

which is defined by

$$f(\tau) = \langle \delta(\tau - \tau_a) \rangle. \tag{4.7}$$

The mean solute arrival time at a radius r_c is given by

$$\langle \tau_a \rangle = \frac{[r(0) + r_c]^2 - r(0)^2}{2k_v}, \tag{4.8}$$

which is also the peak arrival time.

4.3.2 Stochastic convective stream tube (SCST) model

Stochastic convective streamtube models assume that transport occurs along independent streamtubes. Transport within streamtubes is one-dimensional, and there is no mass exchange between individual streamtubes [33, 28, 59, 4]. Thus, these models are sometimes called minimum mixing models. For uniform mean flow, transport in a single radial streamtube of type ω is given by [59, 4]

$$\frac{\partial c_\omega(x,t)}{\partial t} + \frac{k_\omega}{r}\frac{\partial c_\omega(r,t)}{\partial r} - \frac{\alpha k_\omega}{r}\frac{\partial^2 c_\omega(r,t)}{\partial r^2} = 0, \tag{4.9}$$

where k_ω is given by $k_\omega = Q_\omega/(2\pi b_\omega \phi_\omega)$ with Q_ω the flow rate, b_ω the typical aperture and ϕ_ω the porosity of the streamtube, and α is the dispersivity. The total solute concentration

$c(r,t)$ is given by the average of $c_\omega(r,t)$ over all streamtubes

$$c(r,t) = \int d\omega \mathcal{P}(\omega) c_\omega(r,t), \tag{4.10}$$

where $\mathcal{P}(\omega)$ denotes the distribution of streamtubes. Macroscopic solute dispersion here is caused predominantly by velocity contrasts between streamtubes. Transport is fully reversible for $\alpha = 0$. The only irreversible transport mechanism in this framework is dispersion along the streamtubes.

The Lagrangian formulation of transport in a single streamtube ω is identical to (4.4) because transport along a streamtube is given by the radial advection-dispersion equation (4.9). In many realistic flow and transport scenarios, radial dispersion can be disregarded because its effect on solute spreading is negligible compared with advective heterogeneity. For $\alpha = 0$, the Langevin equation (4.4) for a single streamtube ω reduces to

$$\frac{dr_\omega(t)}{dt} = \frac{k_\omega}{r_\omega(t)}. \tag{4.11}$$

Consequently, in the case of an instantaneous solute injection, and using (4.5), we obtain the following expression for the total solute concentration (4.10),

$$c(r,t) = \frac{1}{2\pi br} \int d\omega \mathcal{P}(\omega) \phi_\omega^{-1} \delta[r - r_\omega(t)]. \tag{4.12}$$

The solute arrival time τ_ω at a distance r_c in a single streamtube is given by

$$\tau_\omega = \frac{[r_c + r(0)]^2 - r(0)^2}{2k_\omega}. \tag{4.13}$$

The total solute breakthrough is given by averaging the deterministic arrival times τ_ω over

the ensemble of streamtubes, which is characterized by the distribution $\mathcal{P}_{k_\omega}(k)$ of k_ω,

$$f(\tau) = \int dk \mathcal{P}_{k_\omega}(k) \delta[\tau - \tau_\omega(k)]. \tag{4.14}$$

For a push-pull tracer test, we immediately see that the breakthrough curve is given by $f(\tau) = \delta(t - 2t_p)$, where t_p is the push time. The solute arrival time at the injection point is simply twice the push time because of the full reversibility of transport, as described by (4.11).

4.3.3 Multirate mass transfer (MRMT) model

The MRMT model considers solute transport under mass transfer between a single mobile zone and a series of immobile zones. Fast solute transport in the mobile zone and solute retardation in the immobile zones can lead to non-Fickian spatial distributions and breakthrough curves, and in general to an increase of solute dispersion. Solute mass conservation in the mobile domain is expressed in radial coordinates by

$$\phi_m \frac{\partial c_m(r,t)}{\partial t} + \frac{\phi_m k_v}{r} \frac{\partial c_m(r,t)}{\partial r} - \frac{\alpha \phi_m k_v}{r} \frac{\partial^2 c_m(r,t)}{\partial r^2} = -\phi_{im} \frac{\partial c_{im}(r,t)}{\partial t} \tag{4.15}$$

where ϕ_m and ϕ_{im} are the (average) porosities of the mobile and immobile continua, respectively, $k_v = Q/(2\pi b \phi_m)$ with Q the flow rate and b the width of the injection interval, and α is the dispersivity. Mass transfer between the mobile and immobile regions is linear and thus, assuming zero initial conditions in the immobile regions, the mobile $c_m(r,t)$ and immobile $c_{im}(r,t)$ solute concentrations are related by [38]

$$c_{im}(r,t) = \int_0^t dt' \varphi(t - t') c_m(r,t'), \tag{4.16}$$

where $\varphi(t)$ is the memory function that encodes the specific mass transfer mechanism [63, 65, 25, 38, 43]. For linear first-order mass exchange, $\varphi(t)$ determines the distribution

of transfer rates between mobile and immobile regions [63]. For diffusive mass transfer, it encodes the geometries and the characteristic diffusion scales of the immobile regions [43]. Combining (4.15) and (4.16), we write the temporally non-local single-equation MRMT model

$$\phi_m \frac{\partial c_m(r,t)}{\partial t} + \phi_{im} \frac{\partial}{\partial t} \int_0^t dt' \varphi(t-t') c_m(r,t') + \frac{\phi_m k_v}{r} \frac{\partial c_m(r,t)}{\partial r} - \frac{\alpha \phi_m k_v}{r} \frac{\partial^2 c_m(r,t)}{\partial r^2} = 0. \tag{4.17}$$

It has been shown that the MRMT model is equivalent to CTRW models characterized by uncoupled transition length and time distributions, and to time fractional advection-dispersion models [38, 134, 6]. The MRMT model was employed by [64] to intepret breakthrough curves for radial push-pull tracer tests in fractured dolomite. [88] used a CTRW implementation of MRMT to simulate breakthrough curves for radial push-pull tracer tests. The MRMT models and its equivalent CTRW and fADE formulations describe solute dispersion as an irreversible process. In these modeling frameworks, retardation events that essentially cause macroscopic solute dispersion are independent. Thus, transport is irreversible upon flow reversal.

As in the previous section, we formulate the radial MRMT model (4.17) in a Lagrangian framework. Following the approach employed in [88], we implement MRMT in terms of the continuous time random walk

$$r_{n+1} = r_n + \frac{k_v}{r_n} \Delta s + \sqrt{\frac{2\alpha k_v \Delta s}{r_n}} \xi_n, \tag{4.18a}$$

$$t_{n+1} = t_n + \Delta s + \tau_n \Delta s, \tag{4.18b}$$

where the ξ_n are identical independently distributed Gaussian random variables with zero mean and unit variance, and Δs is an operational time increment. The dimensionless random time increments τ_n are identical independently distributed random variables with the distribution density $\psi(\tau)$. For $\tau_n \equiv 0$, the system (4.18) is identical to the discretized

version of (4.4) in the Ito interpretation.

The continuous time random walk (4.18) is equivalent to (4.17) in the limit of small Δs with the identification [38]

$$\varphi(t) = \frac{\phi_m}{\phi_{im}} \mathcal{L}^{-1} \left\{ \frac{1 - \psi^*(\lambda \Delta s)(1 + \lambda \Delta s)}{\lambda \Delta s \psi^*(\lambda \Delta s)} \right\}, \tag{4.19}$$

where $\mathcal{L}^{-1}\{\cdot\}$ denotes the inverse Laplace transform, $\psi^*(\lambda)$ is the Laplace transform of $\psi(t)$, and λ the Laplace variable. Here and in the following, Laplace-transformed quantities are marked by an asterisk.

The distribution of solute arrival times for both convergent and push-pull tracer tests is obtained from the individual particle arrival times $\tau_a = \inf(t_n | \, |r_n - r_0| > r_c)$ as

$$f(\tau) = \overline{\delta(\tau - \tau_a)}, \tag{4.20}$$

where the overbar $\overline{(\cdot)}$ denotes the average over the ensemble of all particles characterized by the stochastic series of dimensionless retention times $\{\tau_n\}$. Notice that the arrival time distribution in the push-pull case does not reduce to a delta-density, as in the SCST model. Solute transport is irreversible in the MRMT approach.

4.3.4 Comparison of ADE, SCST and MRMT models

The traditional ADE formulation presented in section 4.3.1 does not have the ability to capture anomalous transport, manifested as a power-law tailing in BTCs. To overcome this limitation, SCST and MRMT models have been applied to explain BTCs for convergent and push-pull tests. To show the fundamental difference between the two models, we run both convergent and push-pull simulation with the two models. For the MRMT model, we employ the Pareto waiting time distribution

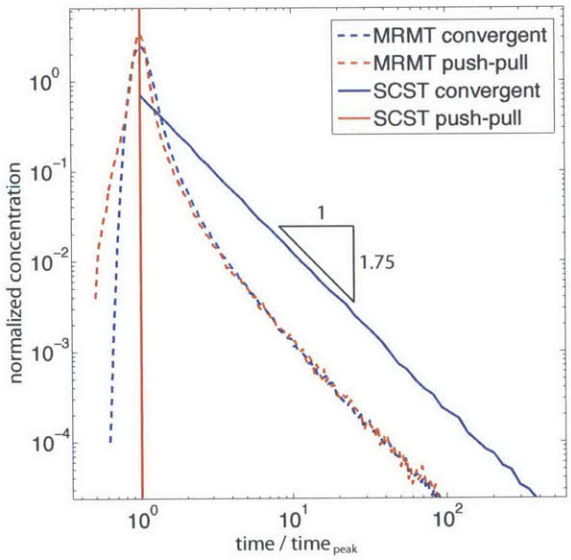

Figure 4-4: Comparison of the breakthrough curves (BTC) for the MRMT and SCST models characterized by the distributions (4.21) and (4.22) with $\beta = 1.75$, $\tau_0 = 0.005$ and $k_0 = 200$, respectively. The BTCs for the convergent and push-pull scenarios are almost identical in the MRMT approach because solute spreading is irreversible. In contrast, the BTC for the convergent and push-pull scenarios in the SCST model are drastically different: in the absence of local dispersion, the BTC in the push-pull scenario is a delta distribution due to the perfect velocity correlation within each streamtube, i.e., full reversibility.

$$\psi(\tau) = \frac{\beta}{\tau_0}\left(\frac{\tau}{\tau_0}\right)^{-1-\beta}, \qquad \tau > \tau_0, \tag{4.21}$$

with $0 < \beta < 2$. For the distribution of the k_ω in the SCST approach we employ the distribution

$$\mathcal{P}_{k_\omega}(k) = \frac{\beta}{k_0}\left(\frac{k}{k_0}\right)^{\beta-1}, \qquad k < k_0. \tag{4.22}$$

The distributions (4.21) and (4.22) for the MRMT and SCST models, respectively, give identical slopes for the long time behavior of the BTCs in the convergent tracer tests. In Figure 4-4, we show the modeling results for MRMT and SCST models. We can see the clear distinction between the two models. Since MRMT does not have a mechanism to capture the reversibility of advective spreading, the BTCs of convergent and push-pull tests are almost identical. In contrast, the stream tube model assumes perfect correlation in velocity, and we observe perfect reversibility in the BTC for the push-pull tracer test in the absence of local dispersion within streamtubes. In reality, there always exists both irreversible diffusive and reversible advective processes, and our objective is to develop a stochastic model that recognizes the competition between the two processes.

4.4 Continuous time random walks (CTRW) with correlated velocities

As discussed in Section 4.3.4, the SCST and MRMT frameworks represent transport models that exhibit full reversibility and complete irreversibility, respectively. The breakthrough curves obtained from convergent and push-pull tracer tests at the Ploemeur fractured aquifer, however, exhibit neither full reversibility nor complete irreversibility (Figure 4-3). Here we develop a stochastic model based on a correlated CTRW approach [90, 78, 35, 80], with the following two design criteria: Lagrangian velocity correlation

that captures flow reversibility, and particle velocity distribution that captures flow heterogeneity.

4.4.1 Model formulation

The starting point for the model is the Langevin equation (4.4) in differential form

$$dr(t) = \frac{k_v dt}{r(t)} + \sqrt{2\alpha \frac{k_v dt}{r(t)}}\xi_r(t). \tag{4.23}$$

By defining the differential space increment $ds = k_v dt/r(t)$ [42, 39], equation (4.23) transforms into

$$dr(s) = ds + \sqrt{2\alpha ds}\xi_r(s), \tag{4.24a}$$

$$dt(s) = \frac{r(s)\phi}{k_v} ds. \tag{4.24b}$$

Discretizing this system in s and setting $\Delta s = \ell$ gives the following system of equations for the particle trajectories in space and time coordinates, or in other words, a CTRW,

$$r_{n+1} = r_n + \ell + \sqrt{2\alpha\ell}\xi_n, \tag{4.25a}$$

$$t_{n+1} = t_n + \frac{\ell r_n}{k_v}. \tag{4.25b}$$

Notice that this CTRW is characterized by a radially dependent time increment. It is by definition equivalent to (4.3) in the limit of small $\ell \ll L$, with L a macroscopic observation scale.

We generalize this CTRW heuristically in order to account for variability in radial particle velocities that may be induced by spatial variability in hydraulic conductivity and retardation properties of the medium. Notice that the transport velocity depends on both hydraulic conductivity and porosity. [90] and [78] demonstrated that the impact of flow het-

erogeneity on large scale solute transport can be quantified in terms of CTRWs whose time increments form a Markov chain based on the observation that the series of Lagrangian particle velocities form a Markov process.

We define here a radial correlated CTRW that allows to vary the flow correlation (persistence of particle velocities) and flow heterogeneity (distribution of particle velocities), to represent and quantify both correlation and heterogeneity-induced anomalous transport features, and to discriminate between them [39]. Thus, we generalize the stochastic process (4.25b) of particle times according to

$$t_{n+1} = t_n + \frac{\ell r_n}{k_v}\tau_n, \tag{4.25c}$$

where the dimensionless time increments $\{\tau_n\}$ form a Markov chain characterized by the marginal distribution density $\psi_0(\tau)$ of initial increments τ_0 and the one-step transition probability density $\psi_1(\tau|\tau')$. The Chapman-Kolmogorov equation for the n-step transition time density $\psi_n(\tau|\tau')$ reads

$$\psi_n(\tau|\tau') = \int_0^\infty d\tau'' \psi_{n-m}(\tau|\tau'')\psi_m(\tau''|\tau'). \tag{4.26}$$

The density $\psi_n(\tau)$ of random increments τ_n after n steps is given by

$$\psi_n(\tau) = \int_0^\infty d\tau' \psi_n(\tau|\tau')\psi_0(\tau'). \tag{4.27}$$

We set here $\psi_0(\tau) = \psi(\tau)$ equal to the steady state density, which is an eigenfunction of the transition density $\psi_1(\tau|\tau')$ and therefore $\psi_n(\tau) = \psi(\tau)$. This is equivalent to assuming that particles sample velocities from the steady state Lagrangian velocity distribution from the beginning. Equations (4.25a) and (4.25c) constitute the equations of motion of solute particles in the proposed radial correlated CTRW approach, where $\psi(\tau)$ determines the flow heterogeneity and $\psi_1(\tau|\tau')$ determines the flow correlation.

4.4.2 Limiting cases

In the following, we briefly determine the limits of the system (4.25a) and (4.25c) for fully correlated and fully uncorrelated dimensionless time increments $\{\tau_n\}$.

Fully correlated case

In the limit of fully correlated $\{\tau_n\}$, i.e., $\psi_1(\tau|\tau') = \delta(\tau - \tau')$, where δ denotes the Kronecker delta, equations (4.25a) and (4.25c) reduce to

$$r_{n+1} = r_n + \ell + \sqrt{2\alpha\ell}\xi_n, \tag{4.28a}$$

$$t_{n+1} = t_n + \frac{\ell r_n}{k_\omega}, \tag{4.28b}$$

where we defined the constant $k_\omega = k_v/\tau_\omega$ with τ_ω the perfectly persistent increment, which is distributed according to $\psi(\tau)$. Each τ_ω, or k_ω, represents a streamtube in the sense of the SCST model. In fact, just as (4.25a) and (4.25b) are equivalent to (4.3), so is system (4.28), which constitutes the equivalence of (4.28) and (4.9). Therefore, the fully correlated case of the proposed model is equivalent to the SCST model.

Fully uncorrelated case

In the limit of fully uncorrelated $\{\tau_n\}$, i.e., $\psi_1(\tau|\tau') = \psi(\tau)$, the system (4.25a) and (4.25b) is equivalent to the following non-local radial advection dispersion equation [45]

$$\frac{\partial c(r,t)}{\partial t} + \int_0^t dt' \left[\frac{\phi k_v}{r}\frac{\partial}{\partial r} M(r, t-t')c(r,t') - \frac{\alpha\phi k_v}{r}\frac{\partial^2}{\partial r^2} M(r,t-t')c(r,t') \right] = 0, \tag{4.29}$$

with the radially dependent memory function

$$M(r,t) = \mathcal{L}^{-1}\left\{\frac{\lambda\tau_k(r)\psi^*[\lambda\tau_k(r)]}{1-\psi^*[\lambda\tau_k(r)]}\right\}. \tag{4.30}$$

We defined $\tau_k(r) = \ell r/k_v$ for compactness. The memory function depends explicitly on the radial position through the radially dependent time scale $\tau_k(r)$. This model is similar to the MRMT model (4.17), except for the radial dependence of the memory function (4.30). The conditions of their equivalence are discussed in [45].

4.4.3 Model implementation

The proposed CTRW with correlated transition times (4.25a) and (4.25c) is solved using random walk particle tracking. The model has three key transport characteristics: the probability distribution of the dimensionless time increments, $\psi(\tau)$, the one step transition probability that quantifies the velocity correlation, $\psi_1(\tau|\tau')$, and the local dispersivity, α. Here we present how to characterize $\psi(\tau)$ and $\psi_1(\tau|\tau')$, and explain in detail the random walk particle tracking algorithm used to solve for the BTCs in the convergent and push-pull scenarios.

Transition probability and correlation

To independently control velocity heterogeneity and velocity correlation, we describe the Markov process $\{\tau_n\}$ with the steady state distribution, $\psi(\tau)$. The continuous non-dimensional transition times τ are discretized into N classes, $\tau \in \bigcup_{j=1}^{N}(\tau_j, \tau_{j+1}]$, such that the transition probabilities between the classes are represented by the $N \times N$ transition matrix $\mathbf{T}$, with components

$$T_{ij} = \int_{\tau_i}^{\tau_{i+1}} d\tau \int_{\tau_j}^{\tau_{j+1}} d\tau' \psi_1(\tau|\tau')\psi(\tau') \Big/ \int_{\tau_j}^{\tau_{j+1}} d\tau' \psi(\tau'). \tag{4.31}$$

Here, we choose equiprobable binning such that

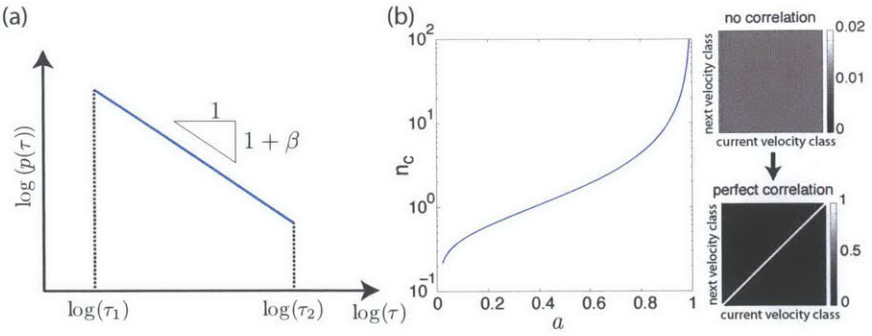

Figure 4-5: Key transport characteristics of our proposed CTRW model. (a) $\psi(\tau)$ follows the truncated Pareto distribution (4.40). The slope of the power law, β, characterizes the flow heterogeneity of the fractured medium. As β decreases, the flow heterogeneity increases. (b) Number n_c of correlation steps given by (4.35) as a function of parameter a for $N = 100$ velocity classes. By changing the value of the diagonal, a, we can systematically vary the strength of the velocity correlation from the uniform transition matrix that is equivalent to the uncorrelated velocity field to the identity matrix that represents a fully correlated velocity field.

$$\int_{\tau_i}^{\tau_{i+1}} d\tau \psi(\tau) = \frac{1}{N}. \tag{4.32}$$

With this condition, $\mathbf{T}$ is a doubly stochastic matrix, which therefore satisfies

$$\sum_{i=1}^{N} T_{ij} = \sum_{j=1}^{N} T_{ij} = 1. \tag{4.33}$$

For a large number of transitions, the transition matrix converges towards the uniform matrix,

$$\left[\lim_{n\to\infty} \mathbf{T}^n\right]_{ij} = \frac{1}{N}, \tag{4.34}$$

whose eigenvalues are 1 and 0. Thus, correlation can be measured by the convergence of $\mathbf{T}$ towards the uniform matrix. The correlation length is determined by the decay rate of the second largest eigenvalue χ_2 (the largest eigenvalue of a stochastic matrix is always 1).

The correlation function is defined by $C(n) = \chi_2^n$, which can be written as

$$C(n) = \exp\left(-\frac{n}{n_c}\right), \qquad n_c = -\frac{1}{\ln(|\chi_2|)}, \tag{4.35}$$

where n_c is the correlation step number. Thus, we define the dimensionless correlation length λ as

$$\lambda = \frac{n_c \ell}{r_c} \tag{4.36}$$

with ℓ the spatial discretization of the correlated CTRW model.

Here we consider a simple transition matrix model, in which all diagonal entries are fixed to a constant a, and the remaining entries are equal to $(1-a)/(N-1)$,

$$T_{ij} = a\delta_{ij} + \frac{1-a}{N-1}(1-\delta_{ij}). \tag{4.37}$$

The diagonal value of $a \leq 1$ determines the correlation strength. A value of $a = 1$ implies perfect correlation, which renders the N–dimensional unity matrix, $T_{ij} = \delta_{ij}$. For $a = 1/N$, all transitions are equally probable, and the transition matrix is equal to the uniform matrix with $T_{ij} = 1/N$; see Figure 4-5b. The transition matrix (4.37) has the eigenvalues $\chi_1 = 1$ and

$$\chi_2 = \frac{Na-1}{N-1}, \tag{4.38}$$

such that we obtain for the dimensionless correlation length (4.36)

$$\lambda = \frac{\ell}{r_c}\frac{1}{\ln\left(\frac{N-1}{Na-1}\right)} \overset{N\gg 1}{\approx} \frac{\ell}{r_c}\frac{1}{\ln\left(a^{-1}\right)}. \tag{4.39}$$

Thus, the correlation length λ is uniquely determined by the value of a.

For the steady state transition time distribution, $\psi(\tau)$, we use the truncated Pareto distribution,

$$\psi(\tau) = \frac{\beta \tau^{-1-\beta}}{\tau_1^{-\beta} - \tau_2^{-\beta}}, \qquad \tau_1 < \tau \leq \tau_2. \tag{4.40}$$

We fix the mean of the transition time distribution to 1, which ensures that the mean arrival time in the correlated CTRW model (4.25c) is equal to the one in the homogeneous model (4.25b). Furthermore we enforce a given ratio of $r_\tau = \tau_2/\tau_1$ such that the power-law range covers the power-law regime observed in the breakthrough curves (see Figure 4-3). This determines τ_1 as

$$\tau_1 = \frac{1-\beta}{\beta} \frac{1 - r_\tau^{-\beta}}{r_\tau^{1-\beta} - 1}. \tag{4.41}$$

This bounds the value of τ_1 between $\ln(r_\tau)/(r_\tau - 1)$, which is the limit of (4.41) for $\beta \to 0$, and $(r_\tau + 1)/(2r_\tau)$, which is the value of (4.41) for $\beta = 2$. For large contrasts $r_\tau \gg 1$, τ_1 is approximately in $(\ln(r)/r, 1/2]$.

The transition time distribution (4.40) is illustrated in Figure 4-5. The slope β of the truncated Pareto distribution describes the velocity heterogeneity. As β decreases, the transport becomes more anomalous because the probability of experiencing large transition times increases. Therefore, smaller β can be understood to represent higher flow heterogeneity, as is well known in the CTRW modeling framework [10].

In summary, the proposed transport model controls the velocity heterogeneity and the velocity correlation with two independent parameters: the slope of the Pareto distribution, β, and the normalized correlation length λ.

Simulation of convergent tracer tests

For the simulation of the convergent scenario, all the particles are injected at the injection well at $r_0 = r_\mathrm{i}$, with r_i the radial distance between injection and pumping well. The convergent BTCs are obtained by recording the particle travel times at the well radius r_w of the pumping well at a radial distance of $r_c = r_\mathrm{i} - r_\mathrm{w}$. The detailed procedure is:

1. Assign the desired values to k_v, α, λ β, and ℓ.
2. Simulate the sequence of particle positions and times according to (4.25a) and (4.25c).
3. Sample particle arrival times at r_w and obtain the BTC.

Simulation of push-pull tracer tests

The implementation for the push-pull scenario is similar to the one for the convergent scenario. Here, particles are injected at $r_0 = r_\mathrm{w}$, with r_w the radius of the injection well. Particles travel radially outwards until the push duration t_push. Then, the radial direction is reversed and particles travel back to the injection well until they reach the well radius r_w. The algorithmic steps are identical to those of the convergent test, except that step 2 is split into its "push" phase and the flow reversal "pull" phase.

4.5 Model behavior and field application

In this section, we study the model behavior of the proposed correlated CTRW model (4.25) depending on the three parameters α, β and λ. We then apply the model to the experimental data presented in Section 4.2 to explore the predictive capabilities of the model through the simultaneous prediction of BTCs in both convergent and push-pull tracer tests.

4.5.1 Model behavior

We first consider the dependence of the peak arrival time on dispersivity α, the heterogeneity distribution as parameterized by β, and the heterogeneity correlation as parameterized

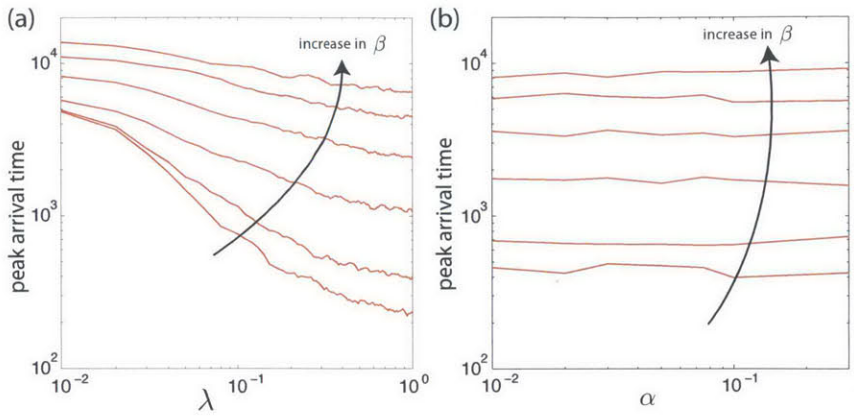

Figure 4-6: Sensitivity analysis for the peak arrival time on the three parameters of our CTRW model. (a) Change in peak arrival times for $\alpha = 0.3$ with varying λ. Different curves represent different degrees of velocity heterogeneity ($\beta = 0.5, 0.6, 0.8, 1, 1.2, 1.4$). (b) Change in peak arrival times for $\lambda = 0.2$ with varying α. Different curves represent different $\beta = 0.5, 0.6, 0.8, 1, 1.2, 1.4$.

by λ. Notice that the mean arrival time is the same in all cases because the model implementation detailed in the previous section forces the mean arrival of the correlated CTRW model (4.25c) to be equal to the one for the homogeneous CTRW model (4.25b). The minimum arrival time is obtained in the perfectly correlated CTRW, i.e., $a = 1$ in (4.37), which gives $\lambda = \infty$, and it is approximately

$$t_{\min} \approx \tau_1 \frac{r_c^2}{2k_v}, \tag{4.42}$$

which can be obtained directly from (4.25c) by setting $\tau_n \equiv \tau_1$, the minimum non-dimensional transition time. For the perfectly correlated model, the minimum arrival time is at the same time the peak arrival. As λ decreases, the peak arrival time increases due to loss of flow coherence, as illustrated in Figure 4-6a.

The simple estimate (4.42) for the fully correlated case also indicates how the peak arrival depends on β. Recall that τ_1 depends on β as given in (4.41): it increases with increasing β up to a maximum of $1/2$ for $\beta = 2$. From this, we conclude that the peak arrival time increases with increasing β, as illustrated in Figure 4-6. This may seem counter-intuitive at first. Notice however, that we force the mean of $\psi(\tau)$ to be equal to 1 for a

given range r_τ. Thus, as β becomes smaller, this means that as the probability of large transition times increases, τ_1 must decrease.

Finally, the dispersivity α has essentially no impact on the peak arrival time, as illustrated in Figure 4-6b. This is intuitively clear when considering the mean arrival time (4.8) for the homogeneous model, which at the same time is the peak arrival time. It is completely independent of α, given that α only impacts the spreading about the mean arrival time.

In Figure 4-7, we plot tracer BTCs for a set of random walk particle tracking simulations for the convergent and push-pull scenarios for various combinations of α, β, and λ. Different features of the BTCs are sensitive to variation in α (dispersivity), β (heterogeneity) and λ (correlation).

The dispersivity α mainly impacts the early time behavior of the convergent BTCs. As expected, a decrease in α leads to a slight increase of the early arrivals due to the reduced particle dispersion (Figure 4-7a). Neither the late time tailing nor the peak position are affected by changes in α. For the push-pull scenario, a decrease in α decreases the relative dispersion of particle arrival times about the peak arrival times (Figure 4-7b). As for the push-pull test, the late-time scaling is not affected by the value of α.

For fixed λ, an increase in β leads to a decrease in BTC tailing in both the convergent and push-pull scenarios, as expected in the CTRW modeling framework [10] (Figures 4-7c,d).

The correlation length λ impacts the early time BTC in the convergent scenario. We have already seen in Figure 4-6a that the peak arrival time increases with decreasing λ. Figure 4-7e shows that also the relative distance between the minimum arrival time and the peak arrival decreases with increasing λ. This behavior is caused by the fact that the particles sample a narrower window of the spectrum of transition times because of increased coherence. This leads to a decrease in the relative dispersion of early arrival times. For the push-pull scenario illustrated in Figure 4-7f, the implact of λ is more dramatic. The relative spread of arrival times about the peak arrival time decreases for increasing λ, which reflects the partial reversibility of the transport process in the presence of flow correlation. In the limit of a perfectly correlated scenario for $\lambda = \infty$, i.e., $a = 1$ in (4.37), the BTC is identical

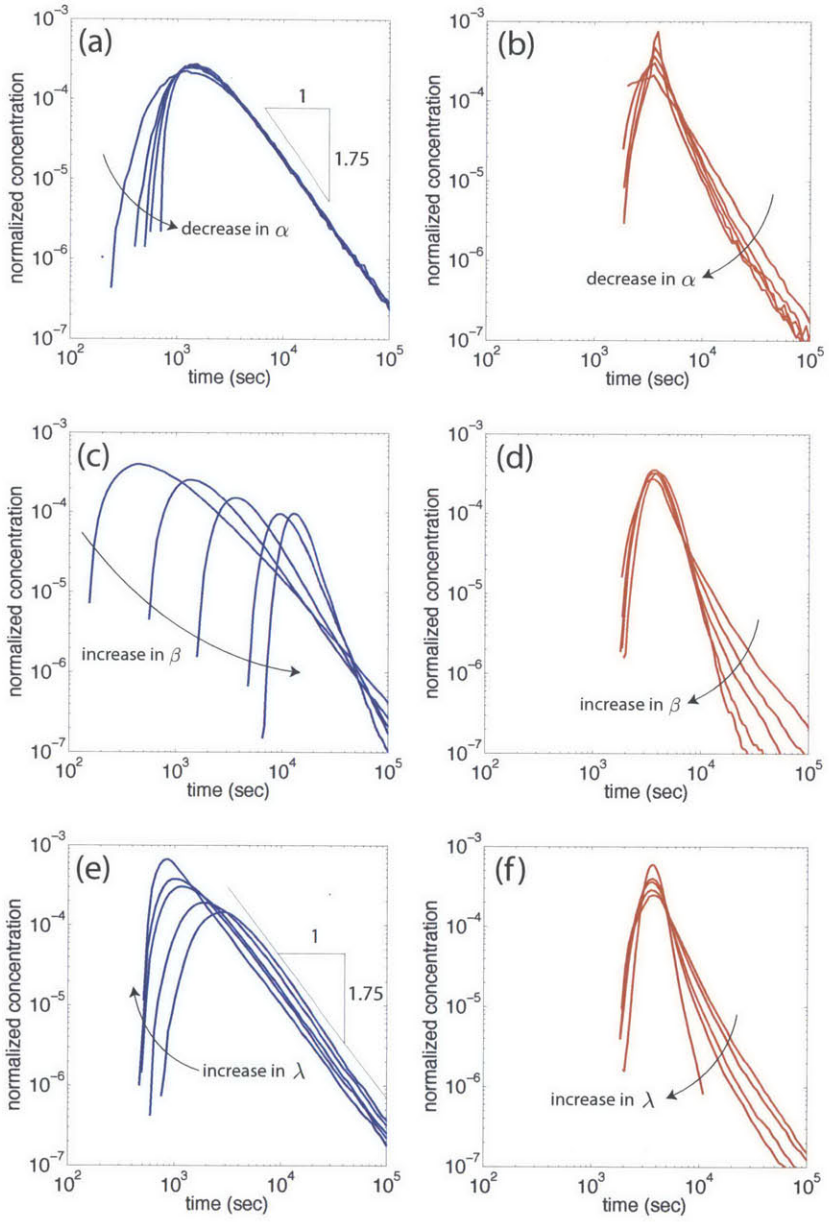

Figure 4-7: Impact of parameters α, β and λ of our CTRW model on transport behavior. Left (a,c,e): convergent tests. Right (b,d,f): push-pull tests. Top (a,b): impact of dispersivity ($\alpha = 0, 0.02, 0.05, 0.1, 0.3$) for fixed $\beta = 0.75$ and $\lambda = 0.2$. Middle (c,d): impact of velocity heterogeneity ($\beta = 0.5, 0.75, 1, 1.5, 2$) for fixed value of $\alpha = 0.03$ and $\lambda = 0.2$. Bottom (e,f): impact of velocity correlation ($\lambda = 0.05, 0.1, 0.3, 0.5, \infty$) for fixed value of $\alpha = 0.03$ and $\beta = 0.75$.

to the one for a homogeneous medium, which is fully characterized by the dispersivity α (Figure 4-7f).

It is important to emphasize the difference between varying dispersivity α and correlation length λ. While increasing λ and decreasing α have qualitatively similar impacts on the relative early arrival times, their impacts on the BTC are very different. First, the peak arrival is essentially independent of dispersivity α, but depends strongly on correlation λ. Secondly, the limit $\lambda = \infty$ renders the BTC in the push-pull scenario identical to the one for a homogeneous medium because of full reversibility: no tailing is observed. For $\alpha = 0$, the strong BTC tailing in the push-pull scenario at long times remains unchanged.

4.5.2 Field application

We now test whether our CTRW model with correlated velocities is able to capture the transport behavior observed in the field, as evidenced by the BTC in the tracer tests. In particular, we address the central question of whether tracer tests under different flow configurations (convergent and push-pull tests) can be explained with *the same* set of model parameters.

We perform a comprehensive comparison between the measured BTCs and the simulated BTCs over the entire three-dimensional space of possible parameter values for dispersivity α, velocity disorder β, and velocity correlation λ. We compute the mean square error (MSE), combined for the convergent and push-pull tests over the entire range of measured data for each test. The MSE surfaces for each of the fracture planes (B1-2 and B1-4) are shown in Figure 4-8 over the β–λ space, for a value of α close to the optimum. These surfaces show the existence of a single minimum in the MSE surface, corresponding to the optimum choice of model parameters that best matches *both* the convergent test and the push-pull test. These values are: $\alpha = 0.03$, $\beta = 0.75$ and $\lambda = 0.22$ for fracture B1-2, $\alpha = 0.02$, $\beta = 0.80$ and $\lambda = 0.06$ for fracture B1-4.

This suggests that B1-2 has similar dispersivity (α), slightly higher heterogeneity (smaller β), and significantly larger flow correlation (larger λ) than B1-4. One way to qualitatively (but independently) confirm this result is by comparing the characteristic fracture length

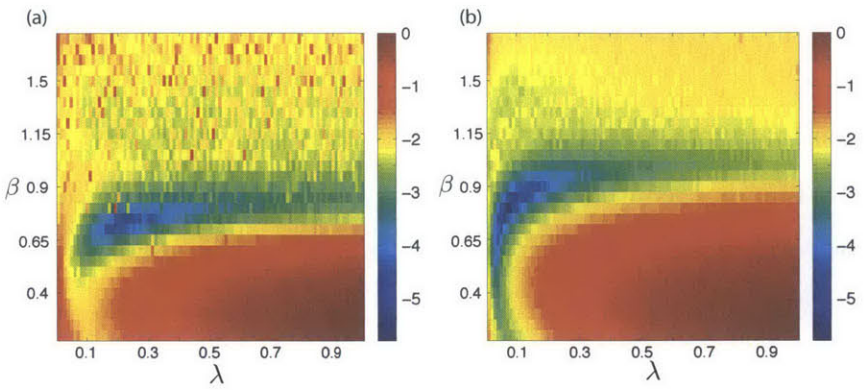

Figure 4-8: Plot of the mean square error (MSE) between modeled and measured BTCs for different model parameters. The error is for the combined differences of the convergent and push-pull tests. (a) MSE for the B1-2 fracture with a value $\alpha = 0.03$. The global minimum is for $\alpha = 0.03$, $\beta = 0.75$ and $\lambda = 0.22$. (b) MSE for the B1-4 fracture with a value $\alpha = 0.02$. The global minimum is for $\alpha = 0.02$, $\beta = 0.80$ and $\lambda = 0.06$.

in the field with the flow correlation length inferred from our model. Recently, ground-penetrating radar (GPR) data was combined with hydrological data to infer the fracture geometry at the same site [46]. Interestingly, this study reports fracture lengths that are larger but of the same order of magnitude (meter scale), and an average fracture length that is larger for B1-2 than for B1-4; a finding that is consistent with our results.

The actual comparison between our model and the field data is shown in Figure 4-9. Our model accurately reproduces the BTCs of both push-pull and convergent tests. Therefore, our CTRW with one-step correlation in velocity is a parsimonious, yet accurate, approximation for describing macroscopic transport in fractured media.

4.6 Summary and Conclusions

In this Chapter, we have proposed a unified framework to characterize transport in fractured media and account for both velocity heterogeneity and flow correlation. We first presented results from convergent and push-pull tracer tests in a fractured-granite subsurface observatory near Ploemeur, France. The field data suggest that flow correlation and flow heterogeneity are the key controlling transport properties. In particular, the BTCs recorded in the field demonstrate the more reversible character of tracer spreading for the

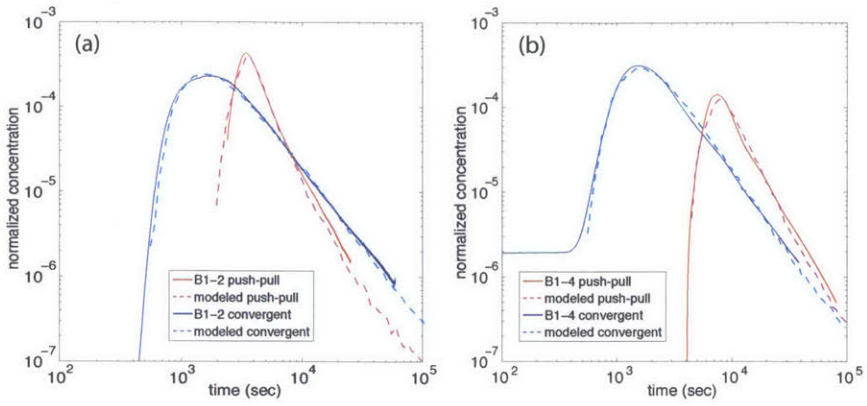

Figure 4-9: Comparison of measured and modeled BTCs for both convergent and push-pull tests, modeled with the same set of parameters. (a) B1-2 fracture; model parameters $\alpha = 0.03$, $\beta = 0.75$, and $\lambda = 0.22$. (b) B1-4 fracture; model parameters $\alpha = 0.02$, $\beta = 0.80$, and $\lambda = 0.06$.

push-pull test compared with the convergent test; an indication of the importance of flow correlation.

Based on the field evidence, we have proposed a stochastic transport model that incorporates local dispersivity, flow heterogeneity (Lagrangian velocity distribution), and flow correlation (Lagrangian velocity correlation) as the three key transport processes, each characterized by a single parameter (α, β and λ, respectively). We have shown analytically that our model embodies other existing models of transport as particular cases: it is equivalent to the MRMT model under the assumption of negligible velocity correlation, and to the SCST model under the assumption of infinite correlation.

In contrast, our model is designed to capture the interplay between velocity heterogeneity and flow correlation, which we have illustrated with a sensitivity analysis of different metrics of the BTCs (early arrival time, peak arrival time, and late-time concentration decay) on the model parameters. The simplicity and versatility of our model has allowed us to perform a robust interpretation of the field tests, since the BTCs of both convergent and push-pull tests are retrieved accurately with the same set of parameters.

Our results raise important questions about modeling choices to simulate mixing and spreading in geologic media. For example, our model captures observations for both push-pull and convergent BTCs with scale-independent local dispersivity, in contrast with the traditional ansatz of a dispersivity that increases with the observational scale [57]. Be-

cause our model accounts for macroscopic features with λ and β, it permits removing the (spurious) scale dependence of local dispersivity α.

Finally, because our model distinguishes between the spreading caused by advective processes (λ) and diffusive processes (α), we speculate that it may provide an avenue to model not only tracer spreading but also fluid mixing [91, 92, 44, 73, 36, 27, 74]. The prediction of mixing and spreading rates in field-scale experiments remains, however, an exciting open question.

Chapter 5

Joint flow–seismic inversion for characterizing fractured reservoirs

5.1 Background

Characterizing fractured geologic formations is essential in hydrogeology, exploration geophysics and petroleum engineering. For example, flow behavior in fractured media is essential to the design and performance assessment of nuclear waste disposal [32, 119]. Similarly, much of the oil and gas reserves worldwide are from reservoirs that are naturally fractured [83]. The relevance of fracture characterization has only increased in recent years with the growth of unconventional resources like oil and gas shale [48]. Determining the effectiveness and sustainability of hydrocarbon production in those environments depends critically on our ability to characterize natural and induced fractures [149, 49].

Traditionally, seismic interpretation and flow modeling have been performed independently. Both in hydrogeologic applications and the upstream oil and gas industry, reservoir modeling typically follows a unidirectional workflow. From an interpretation of seismic surveys and other geophysical and geological data, a structural reservoir model—with reservoir geometry and faults—is built. Facies data and inference are then used to populate reservoir properties (like porosity and permeability) on a fine grid known as a static model (or geomodel). The number of cells in the geomodel is typically too large to perform reservoir flow studies, so a dynamic model is built from either upscaling procedures

or multiscale techniques, which solves the reservoir flow equations on a coarser grid. The rock physics properties (like porosity and permeability) and reservoir dynamics properties (like relative permeability and capillary pressure) are then modified to history-match production data. By then, all feedback to the originating seismic data, and often much of the geologic realism, is lost.

During the last two decades, joint flow-geophysics inversion has received much attention, especially in the context of hydrogeophysics [68]. Most of joint inversion algorithms can be classified into two approaches: using close relation between geophysical and hydrological parameters [127, 96, 72, 67], and using zonation estimates where hydrological and geophysical estimates are assumed to follow similar zonation structure [70, 97]. Rubin et al.[127] proposed the first method to estimate a synthetic hydraulic conductivity field by combining sparsely sampled hydrologic data with densely sampled seismic data assuming the accurate relationship between seismic velocity and hydraulic conductivity is known. However, this relationship is site specific and hard to know a priori. Hyndman et al.[70] used split inversion method to extract the geometry of lithologic zones and successfully estimated seismic velocity field and conductivity field by combining seismic and tracer transport data. This approach do not require strong correlation between geophysical and hydrological parameters. Key assumption behind the work was that the zonation of seismic velocity field and hydraulic conductivity field is identical. Also, the problem is limited to relatively simple geometry. Since this work do not rely on the direct link between seismic and flow properties, this method has limited application for complex geologic structures such as fractured media.

Seismic interpretation in challenging geologic environments like naturally-fractured reservoirs is plagued with uncertainty [23]. Due to the great uncertainty, there is very limited study of joint interpretation of hydrologic and geophysical data on fractured geologic media [26, 46]. Therefore, there is a pressing need for a work that combines multiple measurements for characterizing fracture geologic media. In this study we combined inverted geophysical data from novel double-beam method with hydrologic data which are linked via petrophysical relation.

The goal of our work is twofold: on one hand, reduce that uncertainty by incorporating

dynamic flow measurements into the seismic interpretation; on the other, improve the predictability of reservoir models by making joint use of seismic and flow data. The basic tenet of our proposed framework is that there is a strong dependence between fracture permeability (which drives the flow response) and fracture compliance (which drives the seismic response). This connection has long been recognized [146, 120], and recent works have pointed to the potential of exploiting that connection [19, 116, 148, 156]. Here, we propose a formal approach to improved characterization of fractured reservoirs, and improved reservoir flow predictions, by making joint use of the seismic and flow responses.

5.2 Overall framework

Our approach seeks to combine seismic scattered wavefield data that provides spatial estimates of fracture orientation, spacing, and compliance [51, 157] with flow data (pressure and concentration, or saturation, values) at a number of well locations. The fracture compliance values obtained from seismic data analysis are related to permeability through a rock-physics model [146, 120, 19, 116]. Both the seismic data and the rock-physics model contain potentially significant uncertainty. By combining the flow and seismic data in a single inversion we hope to obtain an improved estimation of the subsurface permeability field that can be used to predict reservoir flow.

The general workflow is shown in Figure 5-1. Our proposed framework is rather general and can be applied to field data, but here we restrict our exposition and validation to synthetic computer models. The starting point for the synthetic models is a 'true' compliance field, which entails generating: (1) a fracture network, which can disordered but have certain geometric statistics (fracture density, length and orientation); (2) elastic compliance of the individual fractures, which also exhibits a predefined geospatial distribution (mean, variance, and correlation length). This model of interconnected discrete fractures, embedded in a reservoir matrix located at depth, is the common physical model from which seismic and flow response is determined.

The true compliance field (C_T) and true permeability field (K_T) are related via a predefined *rock-physics model*, $K_T = f(C_T, \alpha)$, where α denotes a set of parameters governing

the functional relation between C_T and K_T (Figure 5-1). The strong correlation between fracture compliance and permeability can be ascertained from simulations of fluid flow and elastic deformation on rough-walled fractures (Figure 5-2a, see next section). The objective is then to infer the true compliance field and compliance–permeability relationship by a procedure that unifies seismic and flow modeling.

Seismic modeling. We first run a forward seismic model on the true compliance field (C_T) to generate the detailed wavefield [133, 29, 51]. We then treat this wavefield blindly, without knowledge of the underlying structure, to estimate the seismic compliance (C_M) by means of the double-beam method [157]. The error in the estimated compliance field, $e_c = C_T - C_M$, has different scale and often exhibits a strong spatial correlation with the actual compliance field C_T; something that points to the need to model (re-scale and detrend) this error to reduce this dependence. Methodologically, this implies a transformation $C_M \rightarrow C'_M \rightarrow C''_M$ such that the error in the transformed variable, $e''_c = C_T - C''_M$, is only weakly dependent on the underlying (and unknown) true compliance field. This error-modeling of the compliance introduces a set of parameters, β, that needs to be estimated.

Flow modeling. The flow response relies on the compliance-to-permeability relation, from which we generate the fracture-permeability field K_T. We simulate fluid flow and solute transport on this permeability field, from which we extract a dynamic record of pressure (P_T) and production curves (S_T) at a discrete set of locations that represent well measurements. These records are subject to measurement errors, and therefore we denote the accessible, measured quantities as P_M and S_M, respectively. The set of parameters α generating this response via the compliance to permeability relation: $K_T = f(C_T, \alpha)$ are of course unknown. We run the flow model (G_P) and transport model (G_S) on estimates $\hat{K}_T(\hat{\alpha}, \hat{\beta})$ to obtain simulated responses $\hat{P}_T$ and $\hat{S}_T$. The sets of parameters $\hat{\alpha}$ and $\hat{\beta}$ are then estimated by minimizing the error between the measured (P_M, S_M) and modeled ($\hat{P}_T, \hat{S}_T$) flow response. While sophisticated estimation and inversion procedures exist, our work employs a straightforward least-squares minimization procedure:

$$\min_{\hat{\alpha},\hat{\beta}} \left[\sum \frac{\left(P_M - G_P(\hat{K}_T(\hat{\alpha},\hat{\beta}))\right)^2}{\sigma^2_{v_P}} + \sum \frac{\left(S_M - G_S(\hat{K}_T(\hat{\alpha},\hat{\beta}))\right)^2}{\sigma^2_{v_S}} \right]. \tag{5.1}$$

5.3 Fluid flow and elastic deformation on rough-walled fractures

To convert seismic scattering measurements into data useful for hydrologic modeling, a physical relation between fracture compliance and fracture permeability is needed. To show the close relation between the fracture compliance and fracture permeability, we perform simulations of fluid flow and elastic deformation on rough-walled fractures. Following [19], we further extend the methodology of [20] to better represent the correlated structure of fracture roughness and aperture and implement the method of [1] and [22] to run efficient simulation of elastic contact problems.

We first numerically construct synthetic rough-walled fractures using the spectral synthesis method (Figure 5-2(a)) [21, 117, 61]. Spectral analysis decomposes each surface into two components: a power spectral density function and a phase spectrum. The power spectral density of a real fracture surface exhibits power law decay as a function of wave number k (inverse of wavelength, λ) where the exponent is determined by the fractal dimension (D_f) of the fracture surface [21, 62, 117, 20]. The phase spectrum on the other hand is often observed to be nearly a random process independent of frequency (white noise). Further, compared to a single fracture surface, the fracture aperture, the difference between top and bottom fracture surface, has a lower power spectral density for long wavelengths and a value for short wavelengths. This reflects the fact that the top and bottom surfaces are highly correlated for long wave lengths [20, 61]. To incorporate this observation into the numerical synthetic rough surface generator, [20] introduced a critical wavelength (λ_c) where two surfaces are perfectly matched above the critical wavelength and completed independent below the critical wavelength. [61] extended Brown's method to allow the surfaces to be matched at long wavelengths and gradually mismatched as wavelength decrease. However, [61] still assumed zero correlation between two surfaces below the critical wavelength and the way they generate partially correlated phases leads to different variance between the phases of top and bottom surfaces.

Therefore, we propose a method that allows gradual change in correlation strength as a function of wavelength, λ, and conserves variance between phases of top and bottom

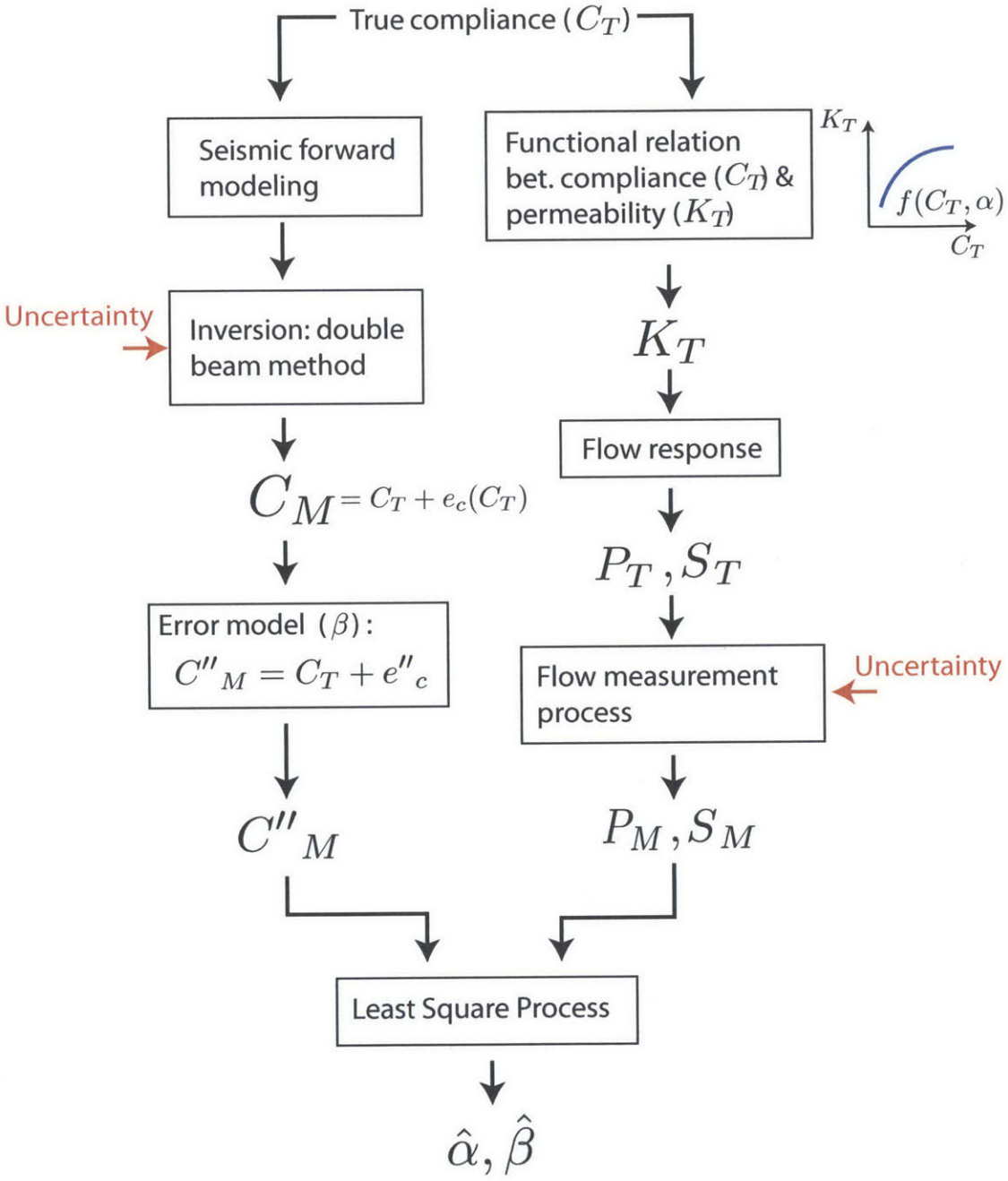

Figure 5-1: Overall framework for joint flow-seismic inversion. The above framework shows how seismic and flow models are integrated to better characterize fractured reservoirs.

surfaces. First, we define a critical wavelength, $\lambda_c = 1/k_c$, where the correlation between the top and bottom surface is 0.5. Second, we define the correlation (γ) of the phases between top and bottom fractures as a function of frequency, $k = 1/\lambda$, as follows: $\gamma = \frac{erf\left(-\frac{k-k_c}{\theta}\right)+1}{2}$. As can be seen in the inset of Figure 5-2(b), correlation gradually decreases from perfect correlation (1) to zero correlation (0) as frequency increases. As defined, γ is 0.5 at $k = k_c$ and θ determines the rate of the change in correlation. As an example, the inset of Figure 5-2(b) shows γ for three different values of θ.

To construct top and bottom fracture surfaces that follow the correlation structure γ, we assign random phases R_1 for the top surface and generate phases R_2 for the bottom surface such that R_2 have correlation γ with R_1. To assign R_2, we mix the two random variables (R_1, R_3) to come up with a new random variable (R_2) such that R_2 and R_1 have the correlation γ as following: $R_2 = \gamma R_1 + \sqrt{1-\gamma^2} R_3$ [55]. Once the phases have been set appropriately, we then obtain the two surfaces by performing inverse Fourier transform of the combined power and phase spectra. After the two surfaces are generated, we define the standard deviation of surface heights (σ_f) and the mean distance (D) between top and bottom surfaces. Figure 5-2(a) shows the top single surface and a fracture aperture for three different θ values with fixed D which gives the minimum distance between top and bottom surfaces to be 0 (no penetration). In summary, we generate the fracture aperture field with four main parameters: the fractal dimension (D_f) that defines the slope of the power spectral density, the critical wave length (λ_c), the rate of change in correlation (θ), and the standard deviation of the fracture profile (σ_f).

From the generated fracture aperture, we obtain the compliance via an elastic deformation simulation on the synthetic rough surface subject to confining stress. This method is explained in detail in [1] and [22], so we only describe the procedure briefly here. We consider only normal stress and the medium to be linearly elastic. As the mean distance between the top and bottom surfaces (D) decrease, the region with interpenetration between top and bottom surface emerges. The medium is assumed to be linearly elastic and we constrain deformation such that there is no penetration between the two surfaces. The stress field ($S(x, y)$) that satisfies no penetration can be obtained using an iterative method. Analytical solution for vertical/normal displacement due to a point force on an elastic half space

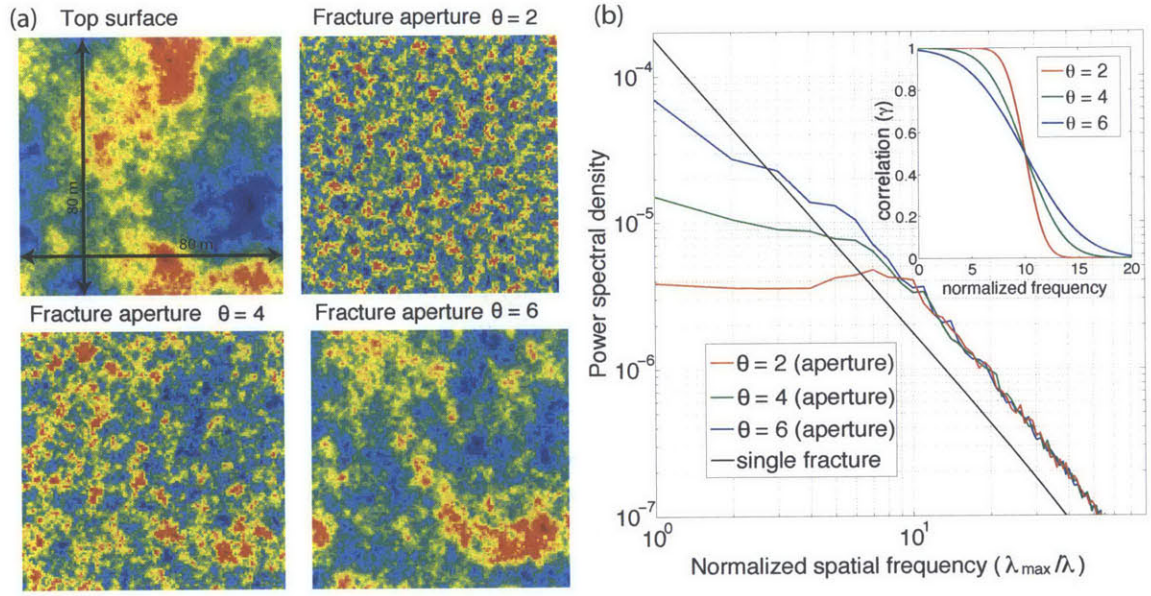

Figure 5-2: (a) Top fracture surface where the horizontal and vertical length is $L = 80$ m and fracture aperture maps (void space between the top and bottom surface) for three different θ values. For this work, we choose $D_f = 2.5$ for fractal dimension, $k_c = 10$ for the normalized critical frequency and $\sigma_f = 0.02$ for standard deviation of surface heights. (b) Power spectral density for three different θ values. Change in power spectral density is smoother as we increase θ. Inset: correlation function (γ) for different θ values.

is known as the Boussinesq solution ($B(r) = \frac{(1-\nu)}{2\pi G}\frac{1}{r}$ where G is the shear modulus and ν is the Poisson's ratio). The normal displacement ($w(x,y)$) due to the stress field $S(x,y)$ is obtained by convolution of the Boussinesq solution: $w(x,y) = \int\int S(x',y')B(r)dx'dy'$. The solution is obtained via a two-dimensional fast Fourier transform. We iteratively update $S(x,y)$ until the stress field satisfies the zero penetration boundary condition [146]. To run the simulation with realistic values, we used 0.25 for Poisson ratio's and $10GPa$ for shear modulus. These are realistic values for Berea Sandstone under confining stress around $30MPa$ [121]. By solving the elastic deformation problem for different values of D, we obtain average normal stress ($\bar{S}$) over the fracture surface for fixed D as following: $\bar{S} = \int\int S(x,y)dxdy/L^2$. From the definition of the fracture compliance, we obtain the compliance as $C = \frac{d\bar{S}}{dD}$.

We perform a fluid flow simulation for incompressible fluid with constant viscosity and density on the final solution of elastic deformation simulation for given D. We consider each aperture value represents the width of the parallel plate. Therefore, we apply lubrication approximation, and we can obtain Darcy type equation for mean velocity, $\underline{u} = -\frac{b^2}{12\mu}\nabla P$, where b is the aperture, μ is the viscosity and P is pressure. From continuity equation, we obtain following equation: $\nabla \cdot \underline{q} = 0$ where $\underline{q} = \underline{u}b$. We obtain pressure by solving the continuity equation with the following boundary condition: constant pressure boundary condition at the left and right boundaries and no flow boundary condition for the top and bottom boundaries. Finally, we obtain the hydraulic aperture using following relation between total outgoing flux and the hydraulic aperture: $Q_{out} = -\frac{b_{hydraulic}^3 W}{12\mu}\frac{P_R - P_L}{L}$, where P_R is the fixed pressure at the right boundary, P_L is the fixed pressure at the left boundary, W is the width the fracture surface and L is the length of the fracture surface.

By plotting the obtained compliance value with the hydraulic aperture, we can obtain the functional relation between the compliance and permeability (Figure 5-3(b)). We typically obtain concave shape for the functional relation. However, it is true that also different shapes can exist depending on the rock type [120]. The dependence of the functional relation on the fracture characteristics has to be further investigated. In this study, we take the compliance-permeability relation shown in Figure 5-3(b). We tested our framework for three different types of the functional relation: linear, convex, concave and confirmed the

framework is equally powerful. The only potential limitation is when the permeability has not enough sensitive with respect to the compliance.

5.4 Seismic inversion on orthogonal discrete fracture networks

We test our approach on discrete fracture networks consisting of two sets of parallel, equidistant, connected fractures oriented at an angle of 0 and 90 degrees with respect to the x-axis (Figure 5-3(a)). The fracture spacing is uniform and equal to 80m. On average, the value of x-directional compliance is two times larger than the y-directional compliance. Our compliance values vary between 10^{-10} and 10^{-9} m/Pa which is the realistic range at the field scale [153]. We construct a spatially-correlated compliance field that follows a lognormal distribution with an exponential autocorrelation function in space (Figure 5-3(a)). We simulate seismic shot gathers using a 3D staggered grid finite-difference method [29, 152, 51]. For seismic inversion, we apply the double-beam method [157] to estimate the modeled seismic compliance field C_M.

5.5 Error model for the compliance field

By analyzing C_M obtained from the double-beam method, we find that the compliance measurement has to be re-scaled and de-trended. As can be seen in Figure 4a, C_M has different scale with C_T and should be re-scaled. In other words, the mean value of measured compliance field ,$\langle C_M \rangle$, is significantly larger than the mean value of true compliance field, $\langle C_T \rangle$, and has to be corrected. Therefore, we introduce re-scaling factor, β_0, where $C'_M = \beta_0 C_M$ such that $\langle C'_M \rangle = \langle C_M \rangle$. The re-scaled error, $e'_c = C_T - C'_M$, is highly correlated with C_T itself (Figure 5-4). From the point of view of estimation, this is of course undesirable because it would require *a priori* knowledge of the true compliance field. Thus, one must introduce an error model that effectively de-trends the modeled response and weakens its dependence on the true compliance field. Our error correction model is motivated by the scatter plot between $C_T - C'_M$ and C_T, which shows a linear trend

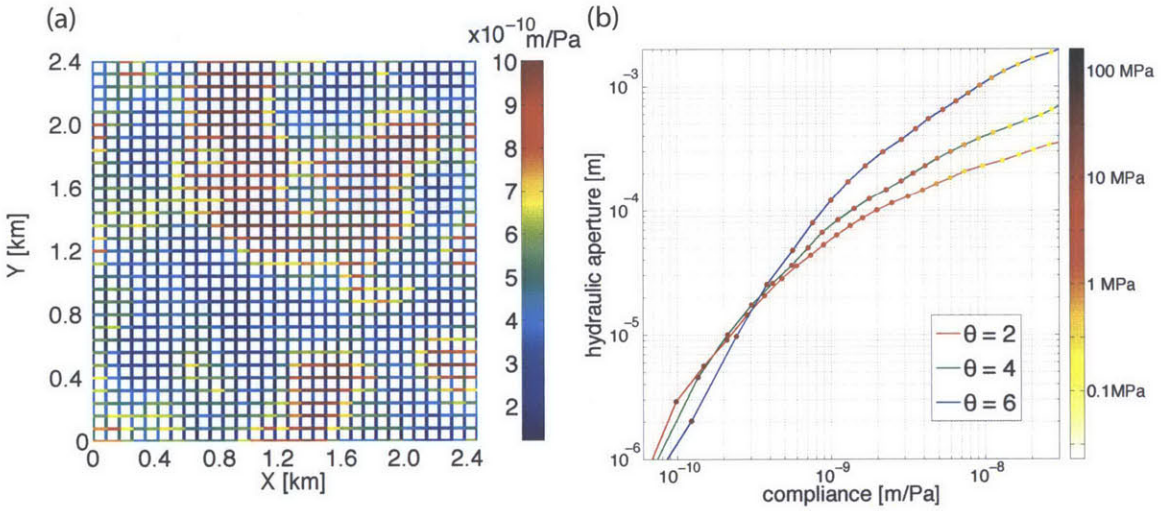

Figure 5-3: (a) True compliance field of the orthogonal discrete fracture networks that we study. Each link has length equal to 80m and has a compliance value between 10^{-10} and 10^{-9} m/Pa. (b) Functional relation between fracture compliance and permeability obtained from simulation of fluid flow and elastic deformation on rough-walled fractures for three different θ values. We parametrize the functional relation with a set of parameters α using the polynomial curve fitting to the data in loglog space: $log(b_{hydraulic}) = \alpha_1 log(C_T)^2 + \alpha_2 log(C_T) + \alpha_3$. Color of solid circles indicate the pressure values at each point. We can observe that the pressure values between the compliance of 10^{-10} and 10^{-9} m/Pa are around 30 MPa.

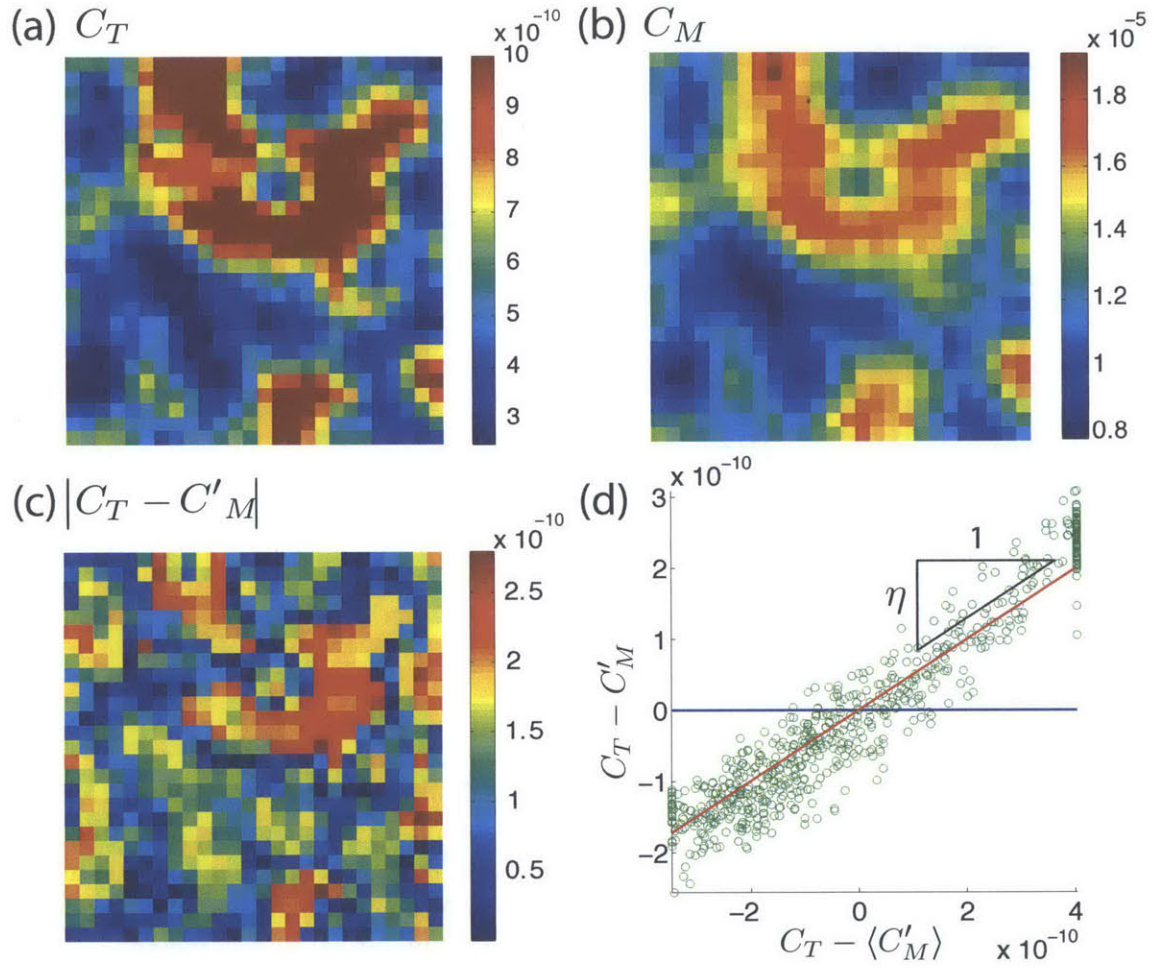

Figure 5-4: (a) True compliance field for the orthogonal discrete fracture network, interpolated to show the smoothed compliance field (C_T). (b) Modeled compliance field from double beam seismic model (C_M). Note that the modeled compliance field has to be re-scaled to have same mean value with the true compliance filed. (c) Difference between true compliance field (C_T) and re-scaled seismic interpreted compliance field (C'_M). We find a strong spatial correlation between the error (e'_c) and the true compliance field (C_T). (d) Error ($C_T - C'_M$) with respect to centered C_T ($C_T - \langle C'_M \rangle$). We observe that C'_M is compressed compared to C_T, and there is a linear relation between the error and the centered C_T.

(Figure 5-4d). From Figure 5-4d, we observe that ${e'}_c \equiv C_T - {C'}_M = \eta(C_T - \langle {C'}_M \rangle) + \epsilon$ where ϵ is a random spatial variable that exhibits a much lower correlation with C_T. From these observations, and reorganizing, $(1-\eta)C_T = (1-\eta)\beta_0 C_M + \beta_0\eta(C_M - \langle C_M \rangle) + \epsilon$. Therefore, we define ${C''}_M = \beta_0[C_M + \beta_1(C_M - \langle C_M \rangle)]$ with $\beta_1 = \eta/(1-\eta) > 0$ but unknown, and ${e''}_c = C_T - {C''}_M = \epsilon$ can be modeled as an independent random function.

5.6 Flow and transport model

We study a simple flow setting: a no-flow condition at the boundaries of the fracture network, and fixed pressure values at the injection well ($P = 1$ at the lower-right corner for scenario 1, at the lower-left corner for scenario 2 and the left center for scenario 3) and production well ($P = 0$ at the upper-left corner for scenario 1, at the upper-right corner for scenario 2 and the right center for scenario 3) (Figure 5-5). We simulate flow through the fracture networks by assuming Poiseuille's law for the fluid flux u_{ij} between nodes i and j, $u_{ij} = -k_{ij}(P_j - P_i)/l$, where P_i and P_j are the fluid pressure values and k_{ij} is compliance-dependent fracture permeability. Imposing mass conservation at each node i and assuming incompressible flow, $\sum_j u_{ij} = 0$, leads to a linear system of equations, which is solved for the pressure values simultaneously at all the nodes. Once the fluxes at the links are known, we simulate transport of a passive tracer by particle tracking. We neglect diffusion along links, and thus particles are advected with the flow velocity between nodes. We assume complete mixing at the nodes. Thus, the link through which the particle exits a node is chosen randomly with flux-weighted probability [78]. This particle-tracking simulation allows us to compute the breakthrough curves (first-passage time distribution) of the tracer at the production well.

5.7 Unifying flow and seismic measurements: least squares

To characterize fracture compliance field, we unify flow and seismic measurements. Pressure and production curves can be obtained by solving the pressure and transport equations with the permeability field obtained from the C_T field. The objective is to find the set of

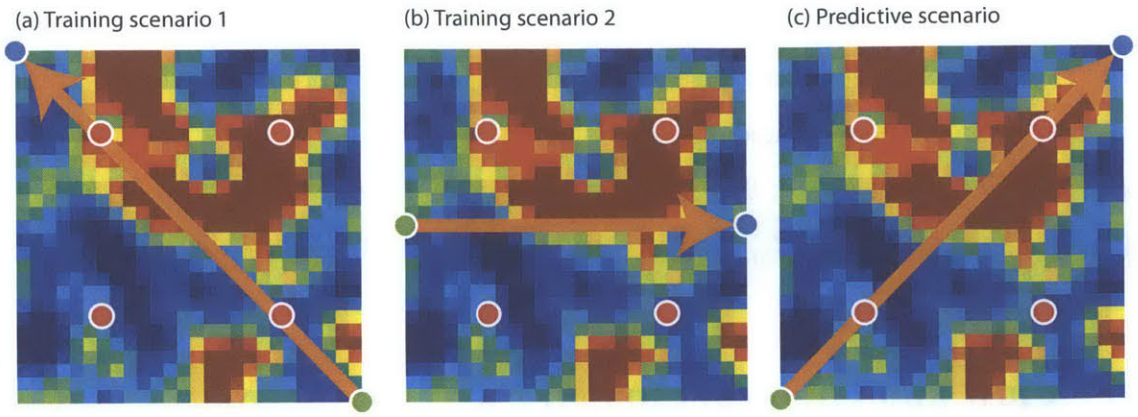

Figure 5-5: (a) First flow scenario used in estimation. Quarter five-spot flow geometry with a single injection well (green circle) and a single production well (blue circle). There are four observation wells (red circle) that measures borehole pressure. (b) Second flow scenario used in estimation. A single injection well (green circle) at the left center and a single production well (blue circle) at the right center. (c) Flow scenario used to test the predictability of estimated permeability field. Quarter five-spot flow geometry in different diagonal direction compared with first flow scenario. Predictive scenario is not used in the estimation step.

parameters, α (which characterizes the functional relation between K_T and C_T, Figure 5-3b), and β (which characterizes the error model of the compliance field, Figure 5-4d) by minimizing the objective function in Equation (5.1), that is, the sum of the squares of the difference between measured and simulated pressure (P_M and $\hat{P}_T$) and the difference between measured and simulated tracer production curves (S_M and $\hat{S}_T$) from the seismically-interpreted compliance field. As input for our least squares minimization procedure we used two flow scenarios (scenario1 and scenario 2), each with four pressure observation wells and measured well pressure data and one breakthrough curve (Figure 5-5). Global optimization algorithm is applied to find a set of parameters (α, β) that minimize our objective function. As can be seen in Figure 5-4, modeled compliance field (C_M) provides excellent information on relative compliance values and structural organization of compliance field. However, the modeled compliance field have very different scale and trend with the true compliance field. Since flow data is sensitive to absolute and relative value of compliance field, we unify flow and seismic measurement to estimate the true compliance field. To test the predictability of our estimated compliance field, flow scenario that is not used in the estimation step is used for verification (Figure 5-5(c)).

5.8 Joint inversion results

From joint inversion of seismic and flow data, we show that the fracture field can be accurately characterized. Figure 5-6 shows a summary of the results obtained from our framework. We highlight three main results:

1. The find that the error modeling of the compliance field was very effective: the error of the modified compliance ($e''_c = C_T - C''_M$, Figure 5-6a) is much lower than the error of the original modeled compliance ($e_c = C_T - C_M$, Figure 5-4), and exhibits virtually no spatial correlation with the true compliance.

2. The functional relation between compliance and permeability was estimated accurately (Figure 5-6b), despite the paucity of dynamic flow data used.

3. The improvements in the estimates of the compliance field and the compliance-to-permeability relation lead to dramatic improvements in the predictability of the model, as evidenced by the ability of the model to *predict* the production curve for a different flow scenario (scenario 3 that is an injector in the left-center and a producer in the right-center, Figure 5-5(c)) in which the injection and production wells are located on a diametrically-different pattern (Figure 5-6c).

5.9 Conclusions

We have presented a new framework for joint inversion of seismic and flow data for improved characterization of fractured reservoirs. The key ingredient of our approach is to recognize that the seismic response and the flow response are linked through a fracture compliance-to-permeability rock-physics relationship. We show that seismic and flow data is complementary where seismic modeling provides structural organization and relative values of compliance field and flow data provides information to re-scale and de-trend the modeled compliance field. Our methodology is rather general, and was designed to be applicable to real field data, where the true compliance field is unknown, the compliance-to-permeability relationship is uncertain, and the flow data are noisy. Here, we have illustrated

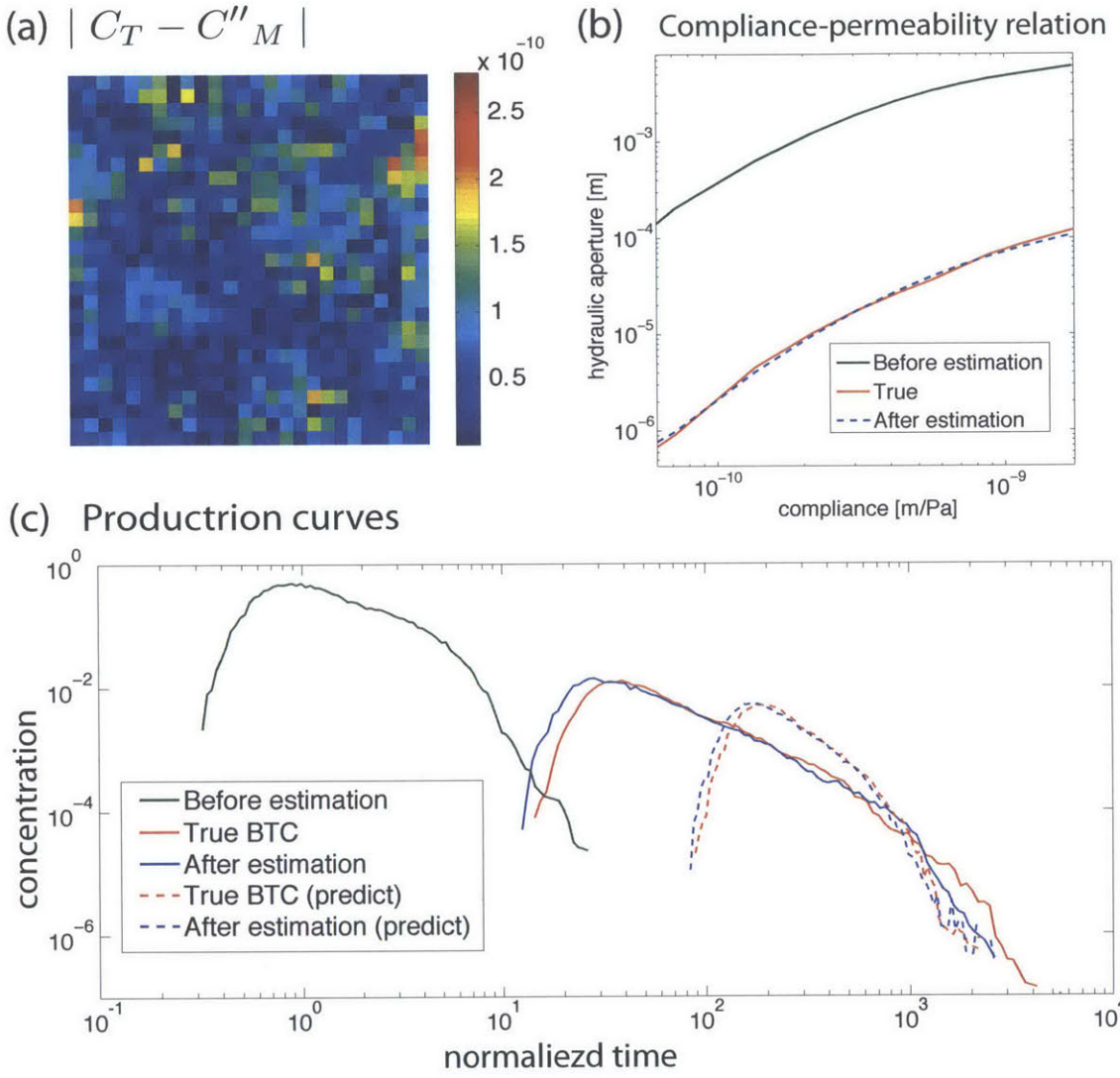

Figure 5-6: (a) Difference between the true compliance field (C_T) and the corrected seismically-interpreted compliance field (C''_M), which shows that the corrected compliance error ($e''_c = C_T - C''_M$) is small and virtually independent of the true compliance field C_T. (b) Estimated compliance-permeability relationship from joint flow-seismic inversion (blue line) accurately captures the true compliance-permeability relationship (red line); the green line is the initial input for our least square procedure. (c) Tracer production curves before (green solid line) and after inversion (blue solid line) compared with the measurements (red solid line). The dashed lines show the performance of the model in *predictive mode*, in which the model is used after inversion to predict the flow response for a different well configuration (a quarter-five spot with injector in the upper-left and producer in the lower-right corner).

the potential of the framework through synthetic computer models of fractured reservoirs. We have shown that integrating seismic interpretation (through the double-beam method [51]) with flow modeling leads not only to robust parameter estimation, but also to reservoir flow models that are more predictive. Our methodology will be extended to more challenging setting where fracture network has random spacing. Also, more sophisticated inversion and data assimilation techniques will be applied. If our workflow is shown to be effective for general fracture network system, the methodology will be applied to real field data.

Chapter 6

Conclusions and future work

6.1 Intellectual contributions

In this thesis, we first identified the origin of anomalous transport at pore scale and developed a predictive transport model that incorporates the identified physical origin of anomalous transport. The generality of our findings and the applicability of the developed model is shown for Darcy-scale transport through lattice fracture networks and finally applied to field-scale tracer transport experiments. Our parsimonious transport model, in the form of correlated CTRW, accurately predicts the anomalous transport behavior from pore scale to field scale. Thus, the proposed correlated CTRW modeling approach furnishes a simple yet powerful framework for characterizing flow and transport through porous and fractured media. Finally, we proposed joint flow-seismic inversion framework to better characterize fractured geologic media.

Following are the summary of the research highlights.

1. We identified pore-scale origin of anomalous transport in real rock: the interplay between flow correlation and velocity heterogeneity (Chapter 2).

2. Based on the understanding of the origin of anomalous transport, we proposed the predictive transport model in the form of correlated CTRW (Chapter 2).

3. Our findings on pore-scale transport through real rock is extended to Darcy-scale transport through lattice fracture networks (Chapter 3).

4. Our transport model captured the full multidimensional particle transport dynamics for a broad range of network heterogeneities and for both advection- and diffusion-dominated flow regimes (Chapter 3).

5. Proposed a field tracer test methodology that quantifies flow correlation and velocity heterogeneity (Chapter 4).

6. Our transport model captures the anomalous behavior in the field breakthrough curves for both push-pull and convergent flow geometries, with the same set of parameters (Chapter 4).

7. Based on the identified relation between fracture permeability and fracture compliance, we proposed a joint flow-seismic inversion framework (Chapter 5).

8. The joint flow-seismic inversion reduced the error in the seismic interpretation and improved predictions of the reservoir flow dynamics. (Chapter 5).

6.2 Future work: laboratory experiments using microfluidics

We have investigated the origin of anomalous transport through 3D real rock (Chapter 2) and lattice fractures (Chapter 3). Both works relied on numerical simulation and the complementary follow up research will be conducting particle tracking experiment and particle image velocimetry using microfluidics. Microfluidics experiments will allow direct visualization of Eulerian velocity field and Lagrangian trajectories. This will lead to more rigorous validation of our findings. Moreover, the impact of anomalous transport on reactive transport and bacteria transport can be studied using microfluidics which often is very challenging with numerical simulations.

6.3 Future work: Joint flow-seismic inversion

There are many exciting open questions regarding joint flow-seismic interpretation. Relationships among geophysical properties and rock fracturing have been extensively studied, but relatively few studies relate the underlying geometrical and mechanical properties of the fractured rock to permeability. Using forward models, the quantitative relation between fracture geometry and stress-dependent properties including permeability, electrical conductivity, and seismic velocity could be identified. This will lead to a new inverse method that integrates various geophysical and flow measurements for better characterization of underlying fractured media. Also, there are not many laboratory experiments relating flow and geophysical measurements. Well controlled laboratory experiments on joint flow and geophysical measurement can lead to the better understanding of the link between flow and geophysical responses.

Bibliography

[1] D. J. Andrews. On modeling closure of rough surfaces in contact. *Eos, Transactions AGU*, 69:1426, 1988.

[2] D. Balcan, V. Colizza, B. Gonçalves, H. Hu, J. J. Ramasco, and A. Vespignani. Multiscale mobility networks and the spatial spreading of infectious diseases. *Proc. Natl. Acad. Sci. USA*, 106:21484–21489, 2009.

[3] J. Bear. *Dynamics of Fluids in Porous Media*. Elsevier, New York, 1972.

[4] M. W. Becker and A. M. Shapiro. Interpreting tracer breakthrough tailing from different forced-gradient tracer experiment configurations in fractured bedrock. *Water Resour. Res.*, 39:1024, 2003.

[5] R. Benke and S. Painter. Modeling conservative tracer transport in fracture networks with a hybrid approach based on the Boltzmann transport equation. *Water Resour. Res.*, 39:1324, 2003.

[6] D. A. Benson and M. M. Meerschaert. A simple and efficient random walk solution of multi-rate mobile/immobile mass transport equations. *Adv. Water Resour.*, 32: 532–539, 2009.

[7] D. A. Benson, S. W. Wheatcraft, and M. M. Meerschaert. Application of a fractional advection-dispersion equation. *Water Resour. Res.*, 36:1403–1412, 2000.

[8] B. Berkowitz and H. Scher. Anomalous transport in random fracture networks. *Phys. Rev. Lett.*, 79(20):4038–4041, 1997.

[9] B. Berkowitz and H. Scher. Anomalous transport in correlated velocity fields. *Phys. Rev. E*, 81:011128, 2010.

[10] B. Berkowitz, A. Cortis, M. Dentz, and H. Scher. Modeling non-Fickian transport in geological formations as a continuous time random walk. *Rev. Geophys.*, 44(2): RG2003, 2006.

[11] R. Bibby. Mass transport of solutes in dual-porosity media. *Water Resour. Res.*, 17 (4):1075–1081, 1981.

[12] B. Bijeljic and M. J. Blunt. Pore-scale modeling and continuous time random walk analysis of dispersion in porous media. *Water Resour. Res.*, 42:W01202, 2006.

[13] B. Bijeljic and M. J. Blunt. Pore-scale modeling of transverse dispersion in porous media. *Water Resour. Res.*, 43:W12S11, 2007.

[14] B. Bijeljic, P. Mostaghimi, and M. J. Blunt. Signature of non-Fickian solute transport in complex heterogeneous porous media. *Phys. Rev. Lett.*, 107:204502, 2011.

[15] B. Bijeljic, P. Mostaghimi, and M. J. Blunt. Insights into non-fickian solute transport in carbonates. *Water Resour. Res.*, 49(5):2714–2728, 2013.

[16] B. Bijeljic, A. Raeini, P. Mostaghimi, and M. J. Blunt. Predictions of non-fickian solute transport in different classes of porous media using direct simulation on pore-scale images. *Physical Review E*, 87(1):013011, 2013.

[17] G. S. Bodvarsson, W. B., R. Patterson, and D. Williams. Overview of scientific investigations at Yucca Mountain: the potential repository for high-level nuclear waste. *J. Contaminant Hydrol.*, 38:3–24, 1999.

[18] J. P. Bouchaud and A. Georges. Anomalous diffusion in disordered media — statistical mechanisms, models and physical applications. *Phys. Rep.*, 195:127–293, 1990.

[19] S. Brown and X. Fang. Fluid flow property estimation from seismic scattering data. *SEG Technical Program Expanded Abstracts*, pages 1–6, 2012. doi: 10.1190/segam2012-1315.1. URL `http://library.seg.org/doi/pdfplus/10.1190/segam2012-1315.1`.

[20] S. R. Brown. Simple mathematical model of a rough fracture. *J. Geophys. Res.*, 100: 5941–5952, 1995.

[21] S. R. Brown and C. H. Scholz. Broad bandwidth study of the topography of natural rock surfaces. *J. Geophys. Res.*, 90:12575–12582, 1985.

[22] S. R. Brown, D. J. Andrews, and P. K. Kang. Elastic deformtation of rough-walled fractures. *in preparation*, 2014.

[23] D. R. Burns, M. E. Willis, M. N. Toksöz, and L. Vetri. Fracture properties from seismic scattering. *The Leading Edge*, 26:1186, 2007.

[24] M. C. Cacas, E. Ledoux, and G. de Marsily. Modeling fracture flow with a stochastic discrete fracture network: calibration and validation. 2. The transport model. *Water Resour. Res.*, 26(3):491–500, 1990.

[25] J. Carrera, X. Sánchez-Vila, I. Benet, A. Medina, G. A. Galarza, and J. Guimerá. On matrix diffusion: formulations, solution methods and qualitative effects. 6:178–190, 1998.

[26] J. Chen, S. Hubbard, J. Peterson, K. Williams, M. Fiene, P. Jardine, and D. Watson. Development of a joint hydrogeophysical inversion approach and application to a contaminated fractured aquifer. *Water Resour. Res.*, 42:W06425, 2006.

[27] G. Chiogna, D. L. Hochstetler, A. Bellin, P. K. Kitanidis, and M. Rolle. Mixing, entropy and reactive solute transport. *Geophys. Res. Lett.*, 39:L20405, 2012.

[28] O. A. Cirpka and P. K. Kitanidis. An advective-dispersive streamtube approach for the transfer of conservative tracer data to reactive transport. *Water Resour. Res.*, 36: 1209–1220, 2000.

[29] R. T. Coates and M. Schoenberg. Finite-difference modeling of faults and fractures. *Geophysics*, 60:1514–1526, 1995.

[30] L. Cueto-Felgueroso and R. Juanes. Forecasting long-term gas production from shale. *Proc. Natl. Acad. Sci. USA*, 110(49):19660–19661, doi:10.1073/pnas.1319578110, 2013.

[31] J. B. Curtis. Fractured shale-gas systems. *AAPG Bull.*, 86:1921–1938, 2002.

[32] V. Cvetkovic, S. Painter, N. Outters, and J. O. Selroos. Stochastic simulation of radionuclide migration in discretely fractured rock near the sp hard rock laboratory. *Water Resour. Res.*, 40:W02404, 2004.

[33] G. Dagan and E. Bressler. Solute dispersion in unsaturated soil at field scale, I, Theory. 43:461–466, 1979.

[34] S. S. Datta, H. Chiang, T. S. Ramakrishnan, and D. A. Weitz. Spatial fluctuations of fluid velocities in flow through a three-dimensional porous medium. *Phys. Rev. Lett.*, 111:064501, 2013.

[35] P. de Anna, T. Le Borgne, M. Dentz, A. M. Tartakovsky, D. Bolster, and P. Davy. Flow intermittency, dispersion, and correlated continuous time random walks in porous media. *Phys. Rev. Lett.*, 110:184502, 2013.

[36] J.-R. de Dreuzy, J. Carrera, M. Dentz, and T. Le Borgne. Time evolution of mixing in heterogeneous porous media. *Water Resour. Res.*, 48:W06511, 2012.

[37] J.-R. de Dreuzy, Y. Méheust, and G. Pichot. Influence of fracture scale heterogeneity on the flow properties of three-dimensional discrete fracture networks (DFN). 117: B11207, 2012.

[38] M. Dentz and B. Berkowitz. Transport behavior of a passive solute in continuous time random walks and multirate mass transfer. *Water Resour. Res.*, 39:1111, 2003.

[39] M. Dentz and D. Bolster. Distribution- versus correlation-induced anomalous transport in quenched random velocity fields. *Phys. Rev. Lett.*, 105:244301, 2010.

[40] M. Dentz and A. Castro. Effective transport dynamics in porous media with heterogeneous retardation properties. *Geophys. Res. Lett.*, 36:L03403, 2009.

[41] M. Dentz, A. Cortis, H. Scher, and B. Berkowitz. Time behavior of solute transport in heterogeneous media: transition from anomalous to normal transport. *Adv. Water Resour.*, 27(2):155–173, 2004.

[42] M. Dentz, D. Bolster, and T. Le Borgne. Concentration statistics for transport in random media. *Phys. Rev. E*, 80:010101(R), 2009.

[43] M. Dentz, P. Gouze, and J. Carrera. Effective non-local reaction kinetics for transport in physically and chemically heterogeneous media. *J. Contaminant Hydrol.*, 120–121:222–236, 2011.

[44] M. Dentz, T. Le Borgne, A. Englert, and B. Bijeljic. Mixing, spreading and reaction in heterogeneous media: A brief review. *J. Contaminant Hydrol.*, 120–121:1–17, 2011.

[45] M. Dentz, P. K. Kang, and T. Le Borgne. A multirate mass transfer solute transport model in radial coordinates. in preparation, 2014.

[46] C. Dorn, N. Linde, T. Le Borgne, O. Bour, and M. Klepikova. Inferring transport characteristics in a fractured rock aquifer by combining single-hole ground-penetrating radar reflection monitoring and tracer test data. *Water Resour. Res.*, 48: W11521, 2012.

[47] C. Dorn, N. Linde, T. Le Borgne, O. Bour, and J.-R. de Dreuzy. Conditioning of stochastic 3-D fracture networks to hydrological and geophysical data. *Adv. Water Resour.*, 62:79–89, 2013.

[48] J. R. Dyni. Geology and resources of some world oil-shale deposits. *U. S. Geological Survey*, pages 2005–5294, 2006.

[49] T. Engelder. Capillary tension and imbibition sequester frack fluid in marcellus gas shale. *Proc. Natl. Acad. Sci. USA*, 109:E3625, 2012.

[50] L. M. Ensign, R. Cone, and J. Hanes. Oral drug delivery with polymeric nanoparticles: The gastrointestinal mucus barriers. *Adv. Drug. Deliv. Rev.*, 64(6):557–570, 2012.

[51] X. Fang, M. Fehler, T. Chen, D. Burns, and Z. Zhu. Sensitivity analysis of fracture scattering. *Geophysics*, 78:T1–T10, 2013.

[52] S. Feenstra, J. A. Cherry, and E. A. Sudicky. Matrix diffusion effects on contaminant migration from an injection well in fractured sandstone. *Ground Water*, 22(3):307–316, 1985.

[53] G. Ferguson and T. Gleeson. Vulnerability of coastal aquifers to groundwater use and climate change. *Nat. Clim. Chang.*, 2(5):342–345, 2012.

[54] A. Fick. Ueber diffusion. *Ann. der. Physik*, 170:59–86, 1855.

[55] K. J. Gabriel and H. S. Colburn. Interaural correlation discrimination: I. bandwidth and level dependence. *J. Acoust. Soc. Am.*, 69:1394–1401, 1981.

[56] S. P. Garabedian, D. R. LeBlanc, L. W. Gelhar, and M. A. Celia. Large-scale natural gradient tracer test in sand and gravel, Cape Cod, Massachusetts 2. Analysis of spatial moments for a nonreactive tracer. *Water Resour. Res.*, 27(5):911–924, 1991.

[57] L. W. Gelhar, C. Welty, and K. R. Rehfeldt. A critical review of data on field-scale dispersion in aquifers. *Water Resour. Res.*, 28:1955–1974, 1992.

[58] H. H. Gerke and M. T. van Genuchten. A dual-porosity model for simulating the preferential flow of water and solutes in structured porous media. *Water Resour. Res.*, 29(2):305–319, 1993.

[59] T. R. Ginn. Stochastic-convective transport with nonlinear reactions and mixing: finite streamtube ensemble formulation for multicomponent reaction systems with intra-streamtube dispersion. *J. Contaminant Hydrol.*, 47:1–28, 2001.

[60] T. Gleeson, Y. Wada, M. F. P. Bierkens, and L. P. H. van Beek. Water balance of global aquifers revealed by groundwater footprint. *Nature*, 488(7410):197–200, 2012.

[61] P. W. J. Glover, K. Matsuki, R. Hikima, and K. Hayashi. Synthetic rough fractures in rocks. *J. Geophys. Res.*, 103:9609–9620, 1998.

[62] John A. Goff. Comment on fractal mapping of digitized images: Application to the topography of arizona and comparison with synthetic images by j. huang and d. l. turcotte. *Journal of Geophysical Research: Solid Earth*, 95(B4): 5159–5159, 1990. ISSN 2156-2202. doi: 10.1029/JB095iB04p05159. URL `http://dx.doi.org/10.1029/JB095iB04p05159`.

[63] R. Haggerty and S. M. Gorelick. Multiple-rate mass transfer for modeling diffusion and surface reactions in media with pore-scale heterogeneity. *Water Resour. Res.*, 31 (10):2383–2400, 1995.

[64] R. Haggerty, S. W. Fleming, L. C. Meigs, and S. A. McKenna. Tracer tests in a fractured dolomite 2. Analysis of mass transfer in single-well injection-withdrawal tests. *Water Resour. Res.*, 37:1129–1142, 2001.

[65] C. F. Harvey and S. M. Gorelick. Temporal moment-generating equations: Modeling transport and mass transfer in heterogeneous aquifers. *Water Resour. Res.*, 31:1895–1911, 1995.

[66] C. F. Harvey, C. H. Swartz, A. B. M. Badruzzaman, N. Keon-Blute, W. Yu, M. A. Ali, J. Jay, R. Beckie, V. Niedan, D. Brabander, K. N. Ashfaque P. M. Oates, S. Islam, H. F. Hemond, and M. F. Ahmed. Arsenic mobility and groundwater extraction in bangladesh. *Science*, 298(5598):1602–1606, 2002.

[67] A. C. Hinnell, T. P. A. Ferré, J. A. Vrugt, J. A. Huisman, S. Moysey, J. Rings, and M. B. Kowalsky. Improved extraction of hydrologic information from geophysical data through coupled hydrogeophysical inversion. *Water Resour. Res.*, 46:W00D40, 2010.

[68] S. S. Hubbard and Y. Rubin. Hydrogeological parameter estimation using geophysical data: a review of selected techniques. *J. Contaminant Hydrol.*, 45:3–34, 2000.

[69] P. S. Huyakorn, S. Panday, and Y. S. Wu. A three-dimensional multiphase flow model for assessing NAPL contamination in porous and fractured media, 1. Formulation. *J. Contaminant Hydrol.*, 16:109, 1994.

[70] D. W. Hyndman, J. M. Harris, and S. M. Gorelick. Coupled seismic and tracer test inversion for aquifer property characterization. *Water Resour. Res.*, 30:1965–1977, 1994.

[71] IPCC. *Special Report on Carbon Dioxide Capture and Storage,* B. Metz et al. (eds.). Cambridge University Press, 2005.

[72] J. Irving and S. Kamini. Stochastic inversion of tracer test and electrical geophysical data to estimate hydraulic conductivities. *Water Resour. Res.*, 46:W11514, 2010.

[73] B. Jha, L. Cueto-Felgueroso, and R. Juanes. Fluid mixing from viscous fingering. *Phys. Rev. Lett.*, 106:194502, 2011.

[74] B. Jha, L. Cueto-Felgueroso, and R. Juanes. Synergetic fluid mixing from viscous fingering and alternating injection. *Phys. Rev. Lett.*, 111:144501, doi:10.1103/PhysRevLett.111.144501, 2013.

[75] R. Juanes, J. Samper, and J. Molinero. A general and efficient formulation of fractures and boundary conditions in the finite element method. 54(12):1751–1774, 2002.

[76] D. Kandhai, D. Hlushkou, A. G. Hoekstra, P. M. A. Sloot, H. Van As, and U. Tallarek. Influence of stagnant zones on transient and asymptotic dispersion in macroscopically homogeneous porous media. *Phys. Rev. Lett.*, 88:234501, 2002.

[77] P. K. Kang, M. Dentz, and R. Juanes. Predictability of anomalous transport on lattice networks with quenched disorder. *Phys. Rev. E*, 83:030101(R), doi:10.1103/PhysRevE.83.030101, 2011.

[78] P. K. Kang, M. Dentz, T. Le Borgne, and R. Juanes. Spatial markov model of anomalous transport through random lattice networks. *Phys. Rev. Lett.*, 107:180602, 2011.

[79] P. K. Kang, Y. Zheng, X. Fang, M. C. Fehler, D. Burns, and R. Juanes. Joint flow-seismic inversion for characterizing fractured reservoirs. *Society of Exploration Geophysicist*, 2013.

[80] P. K. Kang, P. de Anna, J. P. Nunes, B. Bijeljic, M. J. Blunt, and R. Juanes. Pore-scale origin of anomalous transport in 3D porous media. *Submitted*, 2014.

[81] P. K. Kang, T. Le Borgne, M. Dentz, O. Bour, and R. Juanes. Impact of flow correlation and heterogeneity on transport in fractured media: field evidence and theoretical model. *Submitted*, 2014.

[82] M. Karimi-Fard, L. J. Durlofsky, and K. Aziz. An efficient discrete fracture model applicable for general purpose reservoir simulators. 9(2):227–236, June 2004.

[83] H. Kazemi and J. R. Gilman. *Multiphase flows in fractured petroleum reservoirs.* Academic Press, New York, 1993.

[84] H. Kazemi, L. S. Merrill, K. L. Porterfield, and P. R. Zeman. Numerical simulation of water–oil flow in naturally fractured reservoirs. 16(6):317–326, 1976.

[85] B. S. Kerner. Experimental features of self-organization in traffic flow. *Phys. Rev. Lett.*, 81(17):3797–3800, 1998.

[86] L. Kiraly. Remarques sur la simulation des failles et du réseau karstique par éléments finis dans les modèles d'écoulement. *Bull. Centre Hydrogéol.*, 3:155–167, 1979. Univ. of Neuchâtel, Switzerland.

[87] J. Klafter and R. Silbey. Derivation of the continuous-time random-walk equation. *Phys. Rev. Lett.*, 44:55–58, 1980.

[88] T. Le Borgne and P. Gouze. Non-fickian dispersion in porous media: 2. Model validation from measurements at different scales. *Water Resour. Res.*, 44:W06427, 2007.

[89] T. Le Borgne, O. Bour, F. L. Paillet, and J.-P. Caudal. Assessment of preferential flow path connectivity and hydraulic properties at single-borehole and cross-borehole scales in a fractured aquifer. 328:347–359, 2006.

[90] T. Le Borgne, M. Dentz, and J. Carrera. Lagrangian statistical model for transport in highly heterogeneous velocity fields. *Phys. Rev. Lett.*, 101:090601, 2008.

[91] T. Le Borgne, M. Dentz, D. Bolster, J. Carrera, J.-R. de Dreuzy, and P. Davy. Non-Fickian mixing: Temporal evolution of the scalar dissipation rate in heterogeneous porous media. *Adv. Water Resour.*, 33(12):1468–1475, 2010.

[92] T. Le Borgne, M. Dentz, P. Davy, D. Bolster, J. Carrera, J.-R. de Dreuzy, and O. Bour. Persistence of incomplete mixing: A key to anomalous transport. *Phys. Rev. E*, 84:015301(R), 2011.

[93] K. C. Leptos, J. S. Guasto, J. P. Gollub, A. I. Pesci, and R. E. Goldstein. Dynamics of enhanced tracer diffusion in suspensions of swimming eukaryotic microorganisms. *Phys. Rev. Lett.*, 103:198103, 2009.

[94] D. R. Lester, G. Metcalfe, and M. G. Trefry. Is chaotic advection inherent to porous media flow? *Phys. Rev. Lett.*, 111:174101, 2013.

[95] M. Levy and B. Berkowitz. Measurement and analysis of non-Fickian dispersion in heterogeneous porous media. *J. Contaminant Hydrol.*, 64:203, 2003.

[96] N. Linde, S. Finsterle, and S. Hubbard. Inversion of tracer test data using tomographic constraints. *Water Resour. Res.*, 42:W04410, 2006.

[97] T. Löchbuhler, J. Doetsch, R. Brauchler, and N. Linde. Structure-coupled joint inversion of geophysical and hydrological data. *Geophysics*, 78, 2013.

[98] P. Maloszewski and A. Zuber. On the theory of tracer experiments in fissured rocks with a porous matrix. 79(3–4):333–358, 1985.

[99] L. Martinez-Landa and J. Carrera. An analysis of hydraulic conductivity scale effects in granite (Full-scale Engineered Barrier Experiment (FEBEX), Grimsel, Switzerland). *Water Resour. Res.*, 41(3):W03006, 2005.

[100] L. Martinez-Landa, J. Carrera, M. Dentz, D. Fernandez-Garcia, A. Nardi, and M. W. Saaltink. Mixing induced reactive transport in fractured crystalline rocks. *Appl. Geochem.*, 27(2):479–489, 2012.

[101] S. A. McKenna, L. C. Meigs, and R. Haggerty. Tracer tests in a fractured dolomite 3. Double-porosity, multiple-rate mass transfer processes in convergent flow tracer tests. *Water Resour. Res.*, 37:1143–1154, 2001.

[102] R. Metzler and J. Klafter. The random walks guide to anomalous diffusion: a fractional dynamics approach. *Phys. Rep.*, 339:1–77, 2000.

[103] D. W. Meyer and H. A. Tchelepi. Particle-based transport model with Markovian velocity processes for tracer dispersion in highly heterogeneous porous media. *Water Resour. Res.*, 46:W11552, 2010.

[104] J. Molinero and J. Samper. Large-scale modeling of reactive solute transport in fracture zones of granitic bedrocks. *J. Contaminant Hydrol.*, 82:293–318, 2006.

[105] J. Molinero, J. Samper, and R. Juanes. Numerical modeling of the transient hydrogeological response produced by tunnel construction in fractured bedrocks. 64(4): 369–386, 2002.

[106] N. Mordant, J. Delour, E. Léveque, A. Arnéodo, and J.-F. Pinton. Long time correlations in Lagrangian dynamics: a key to intermittency in turbulence. *Phys. Rev. Lett.*, 89(25):254502, 2002.

[107] L. Moreno and I. Neretnieks. Fluid flow and solute transport in a network of channels. *J. Contaminant Hydrol.*, 14:163–194, 1993.

[108] M. Moroni, N. Kleinfelter, and J. H. Cushman. Analysis of dispersion in porous media via matched-index particle tracking velocimetry experiments. *Adv. Water Resour.*, 30(1):1–15, 2007.

[109] P. Mostaghimi, B. Bijeljic, and M. J. Blunt. Simulation of flow and dispersion on pore-space images. *SPE J.*, 17:1131, 2012.

[110] S. P. Neuman, C. L. Winter, and C. M. Newman. Stochastic theory of field-scale Fickian dispersion in anisotropic porous media. *Water Resour. Res.*, 23(3):453–466, 1987.

[111] C. Nicolaides, L. Cueto-Felgueroso, and R. Juanes. Anomalous physical transport in complex networks. *Phys. Rev. E*, 82:055101(R), 2010.

[112] C. Nicolaides, L. Cueto-Felgueroso, M. C. Gonzalez, and R. Juanes. A metric of influential spreading during contagion dynamics through the air transportation network. *PLoS ONE*, 7(7):e40961, doi:10.1371/journal.pone.0040961, 2012.

[113] OPENFOAM. The open source cfd toolbox. *http://www.openfoam.com*, 2011.

[114] F. M. Orr Jr. and J. J. Taber. Use of carbon dioxide in enhanced oil recovery. *Science*, 224:563–569, 1984.

[115] S. Painter and V. Cvetkovic. Upscaling discrete fracture network simulations: An alternative to continuum transport models. *Water Resour. Res.*, 41:W02002, 2005.

[116] C. L. Petrovitch, L. J. Pyrak-Nolte, and D. D. Nolte. Scaling of fluid flow versus fracture stiffness. *Geophys. Res. Lett.*, 2013.

[117] W. L. Power and T. E. Tullis. Euclidean and fractal models for the description of rock surface roughness. *J. Geophys. Res.*, 96:415–424, 1991.

[118] K. Pruess. Enhanced geothermal systems (EGS) using CO_2 as working fluid: novel approach for generating renewable energy with simultaneous sequestration of carbon. *Geothermics*, 35:351–367, 2006.

[119] K. Pruess, J. S. Y. Wang, and Y. W. Tsang. On thermohydrologic conditions near high-level nuclear wastes emplaced in partially saturated fractured tuff: 1. simulation studies with explicit consideration of fracture effects. *Water Resour. Res.*, 26:1235–1248, 1990.

[120] L. J. Pyrak-Nolte and J. P. Morris. Single fractures under normal stress: The relation between fracture specific stiffness and fluid flow. *Int. J. Rock. Mech. Min.*, 37:245–262, 2000.

[121] New England Research. Elastic constants and strength of berea sandstone. *retrieved online August 23*, 2013. URL `www.ner.com/pdf/NER`$_t n_b$*erea.pdf*.

[122] L. F. Richardson. Atmospheric diffusion shown on a distance-neighbour graph. *Proc. R. Soc. A*, 110:709, 1926.

[123] L. F. Richardson and H. Stommel. Note on eddy diffusion in the sea. *J. Meteor.*, 5: 238, 1948.

[124] A. Rinaldo et al. Reassessment of the 2010-2011 Haiti cholera outbreak and rainfall-driven multiseason projections. *Proc. Natl. Acad. Sci. USA*, 109(17):6602–6607, 2012.

[125] H. Risken. *The Fokker–Planck Equation*. Springer, Berlin, second edition, 1989.

[126] M. Rolle, D. Hochstetler, G. Chiogna, P. K. Kitanidis, and P. Grathwohl. Experimental investigation and pore-scale modeling interpretation of compound-specific transverse dispersion in porous media. 93(3):347–362, 2012.

[127] Y. Rubin, G. Mavko, and J. Harris. Mapping permeability in heterogeneous aquifers using hydrologic and seismic data. *Water Resour. Res.*, 28:1809–1816, 1992.

[128] X. Sanchez-Vila, A. Guadagnini, and J. Carrera. Representative hydraulic conductivities in saturated groundwater flow. *Rev. Geophys.*, 44:RG3002, 2006.

[129] H. Scher and E. W. Montroll. Anomalous transit-time dispersion in amorphous solids. *Phys. Rev. B*, 12(6):2455–2477, 1975.

[130] U. M. Scheven, D. Verganelakis, R. Harris, M. L. Johns, and L. F. Gladden. Quantitative nuclear magnetic resonance measurements of preasymptotic dispersion in flow through porous media. *Phys. Fluids*, 17:117107, 2005.

[131] J. F. Schijven and S. M. Hassanizadeh. Removal of viruses by soil passage: Overview of modeling, processes, and parameters. *Crit. Rev. Env. Sci. Tech.*, 30 (1):49–127, 2000.

[132] K. S. Schmid, S. Geiger, and K. S. Sorbie. Higher order FE–FV method on unstructured grids for transport and two-phase flow with variable viscosity in heterogeneous porous media. 241:416–444, 2013.

[133] M. Schoenberg. Elastic wave behavior across linear slip interfaces. *J. Acoust. Soc. Am.*, 68:1516–1521, 1980.

[134] R. Schumer, D. A. Benson, M. M. Meerschaert, and B. Baeumer. Fractal mobile/immobile solute transport. *Water Resour. Res.*, 39:1022, 2003.

[135] M. F. Shlesinger. Asymptotic solutions of continuous-time random walks. *J. Stat. Phys.*, 10(5):421–434, 1974.

[136] P. L. Smart and I. M. S. Laidlaw. An evaluation of some fluorescent dyes for water tracing. *Water Resour. Res.*, 13(1):15–33, 1977.

[137] M. L. Szulczewski, C. W. MacMinn, H. J. Herzog, and R. Juanes. Lifetime of carbon capture and storage as a climate-change mitigation technology. *Proc. Natl. Acad. Sci. USA*, 109(14):5185–5189, 2012.

[138] A. M. Tartakovsky. Langevin model for reactive transport in porous media. *Phys. Rev. E*, 82:026302, 2010.

[139] A. M. Tartakovsky, G. Redden, P. C. Lichtner, T. D. Scheibe, and P. Meakin. Mixing-induced precipitation: Experimental study and multiscale numerical analysis. *Water Resour. Res.*, 44(6):W06S04, 2008.

[140] A. M. Tartakovsky, D. M. Tartakovsky, and P. Meakin. Stochastic langevin model for flow and transport in porous media. *Phys. Rev. Lett.*, 101:044502, 2008.

[141] G. I. Taylor. Diffusion by continuous movements. *Proc. London Math. Soc.*, 20: 196–211, 1921.

[142] V. Tejedor and R. Metzler. Anomalous diffusion in correlated continuous time random walks. *J. Phys. A: Math. Theor.*, 43(8):082002, 2010.

[143] M. G. Trefry, F. P. Ruan, and D. McLaughlin. Numerical simulations of preasymptotic transport in heterogeneous porous media: Departures from the Gaussian limit. *Water Resour. Res.*, 39(3):1063, 2003.

[144] Y. W. Tsang. Study of alternative tracer tests in characterizing transport in fractured rocks. *Geophys. Res. Lett.*, 22:1421–1424, 1995.

[145] Y. W. Tsang, C. F. Tsang, F. V. Hale, and B. Dverstorp. Tracer transport in a stochastic continuum model of fractured media. *Water Resour. Res.*, 32(10):3077–3092, 1996.

[146] A. J. A. Unger and C. W. Mase. Numerical study of the hydromechanical behavior of two rough fracture surfaces in contact. *Water Resour. Res.*, 29:2101–2114, 1993.

[147] G. M. Viswanathan, V. Afanasyev, S. V. Buldyrev, E. J. Murphy, P. A. Prince, and H. E. Stanley. Lévy flight search patterns of wandering albatrosses. *Nature*, 381: 413–415, 1996.

[148] S. Vlastos, E. Liu, I. G. Main, M. Schoenberg, C. Narteau, X. Y. Li, and B. Maillot. Dual simulations of fluid flow and seismic wave propagation in a fractured network: effects of pore pressure on seismic signature. *Geophys. J. Int.*, 166:825–838, 2006.

[149] N. R. Warner, B. R. Jackson, T. H. Darrah, S. G. Osborn, Down A., K. Zhao, A. White, and A. Vengosh. Geochemical evidence for possible natural migration of marcellus formation brine to shallow aquifers in pennsylvania. *Proc. Natl. Acad. Sci. USA*, 2012.

[150] J. N. Wilking, V. Zaburdaev, M. De Volder, R. Losick, M. P. Brenner, and D. A. Weitz. Liquid transport facilitated by channels in Bacillus subtilis biofilms. *Proc. Natl. Acad. Sci. USA*, 110(3):848–852, 2013.

[151] T. W. Willingham, C. J. Werth, and A. J. Valocchi. Evaluation of the effects of porous media structure on mixing-controlled reactions using pore-scale modeling and micromodel experiments. 42:3185, 2008.

[152] M. Willis, D. Burns, R. Rao, B. Minsley, M. Toksoz, and Vetri L. Spatial orientation and distribution of reservoir fractures from scattered seismic energy. *Geophysics*, 71:O43–O51, 2006.

[153] M. H. Worthington and R. Lubbe. The scaling of fracture compliance. *Geological Society, London*, 270:73–82, 2007.

[154] N. Yoshida and Y. Takahashi. Land-surface contamination by radionuclides from the fukushima daiichi nuclear power plant accident. *Elements*, 8(3):201–206, 2012.

[155] S. R. Yu, M. Burkhardt, M. Nowak ad J. Ries, Z. Petrá˘sek, S. Scholpp, P. Schwille, and M. Brand. Fgf8 morphogen gradient forms by a source-sink mechanism with freely diffusing molecules. *Nature*, 461:533–536, 2009.

[156] Y. Zhang, C. M. Sayers, and J. I. Adachi. The use of effective medium theories for seismic wave propagation and fluid flow in fractured reservoirs under applied stress. *Geophys. J. Int.*, 177:205–221, 2009.

[157] Y. Zheng, X. Fang, M. C. Fehler, and D. R. Burns. Seismic characterization of fractured reservoirs by focusing gaussian beams. *Geophysics*, 78:A23–A28, 2013.